

Optimization of Solar-Coal Hybridization
for Low Solar Augmentation

Aaron T. Bame

A thesis submitted to the faculty of
Brigham Young University
in partial fulfillment of the requirements for the degree of
Master of Science

Brian D. Iverson, Chair
Matthew R. Jones
John Hedengren

Department of Mechanical Engineering
Brigham Young University

Copyright © 2021 Aaron T. Bame
All Rights Reserved

ABSTRACT

Optimization of Solar-Coal Hybridization for Low Solar Augmentation

Aaron T. Bame

Department of Mechanical Engineering, BYU
Master of Science

One approach to enabling a larger penetration of renewable sources of energy is the implementation of hybrid power plants. This work presents a process to determine the preliminary optimal configuration of a concentrating solar power-coal hybrid power plant with low solar augmentation, and is demonstrated on a coal power plant in Castle Dale, UT.

A representative model is developed and validated against published data for a coal power plant of a different configuration than Hunter Unit 3. The simplifications within the representative model include combining multiple feedwater heaters, combining turbines that operate across the same boundary states, and the mass-average calculation for extraction properties to the combined feedwater heaters. It is shown that the representative model can accurately and consistently simulate a coal power plant. Comparing net power generation and boiler heating estimates from the representative model to the benchmark power plant, the representative model is accurate to within $\pm 1\%$ the accepted value from the benchmark power plant. The methods for quantifying solar resource with data from the National Renewable Energy Laboratory are presented with the derivation of an algorithm to simulate a concentrating solar power field arrangement. The solar contribution to electrical power output is estimated using an exergy balance. A simplified financial model is also developed to estimate the solar marginal levelized cost of electricity and payback time using a cash-flow analysis. Estimates for solar resource, solar contribution, and financial performance are consistent with data published by the National Renewable Energy Laboratory or in archival literature. A multi-objective optimization routine is developed consisting of the representative model, the augmentation of solar energy into the solar integration model by means of feedwater heater bypass, solar contribution, levelized cost of electricity, and payback time.

Because this study considered complete FWH bypass, higher solar augmentation ($>3\%$ of boiler heating) is required for a hybrid design to be considered feasible. However, for higher solar augmentation, the costs are also considerably higher and the financial benefit is insufficient to make any hybrid designs feasible unless a carbon tax is in place. A carbon tax will amplify the financial benefit of hybridization, so optimization results are provided assuming a carbon tax value equivalent to the value used in California's Emissions Trading System (16 USD sh.tn.⁻¹). The impact of a green energy premium price paid by consumers is also explored in the context of payback time. The resulting optimal design for the Hunter Unit 3 with a carbon tax and no premium is using parabolic trough collector technology at an augment fraction of $k = 9\%$ to bypass feedwater heater 6. The resulting marginal solar levelized cost of electricity is 9.5×10^{-4} USD kWh⁻¹ with an estimated payback time of 25.2 years. This process can be applied to any coal power plant for which operating data and meteorological data are available to evaluate preliminary hybridization feasibility.

Keywords: hybridization, Concentrating Solar Power, coal, augmentation, renewable energy

ACKNOWLEDGMENTS

First, I offer my most humble appreciation to my committee. Learning from each of you over the course of my research has been a blessing I will value for the duration of my professional career. Your perspectives have made this thesis what it is thanks to your input. Though not a part of my committee, Dr. Kody Powell and Kasra Mohammadi of the University of Utah have provided contributions to this study that have been invaluable.

I owe a special thank you to Dr. Matthew Jones for his assistance throughout my undergraduate education as a professor and research advisor. It was while working with Dr. Jones that I found the joy in research. While I have decided not to pursue a Ph.D. at this time, despite your unwavering encouragement, I am humbled by you believing in me.

I am deeply grateful to PacifiCorp for funding this project and the PacifiCorp employees that have collaborated with me throughout this study. Specifically, I am grateful to Daniel Kinder, Trapper Burdick, and Roy Jewkes at the Hunter Unit 3 and to Ian Hoag for his frequent collaboration and his assistance on this project.

Pivotal to my success was the help of Joseph Furner and the support of my advisor Dr. Brian Iverson. Joseph provided critical work on the financial and solar contribution models used in this study. I will forever be grateful to Dr. Iverson for his guidance and advice during this project. I also appreciate Dr. Iverson's support outside of research-specific details and his understanding when other factors needed higher priority than research.

My friends, classmates, and family also deserve thanks for their encouragement and for putting up with my thesis dominating much of my conversations over these last few years. It means the most when people who know me the best believe in me and my abilities.

I do not have the words to express the thanks I have for the support of my wife, Maren. You have sacrificed so much for us to make it to this point. I do not say it enough, but please know how grateful I am for your constant love and friendship. One of the most important lessons I have learned is that together, we can do anything. Thank you, Maren.

TABLE OF CONTENTS

LIST OF TABLES	ix
LIST OF FIGURES	xi
NOMENCLATURE	xiii
Chapter 1 Introduction	1
1.1 Fossil Fuel vs. Renewable Energy	1
1.2 Evaluating CSP Hybridization Potential	2
1.3 Hybridization capabilities	3
1.4 CSP Technology	5
1.5 CSP Integration Options	6
1.6 Benefits of CSP-Hybridization	7
1.7 Existing CSP Hybrid Power Plants	9
1.8 Research Objectives	9
Chapter 2 Methods	13
2.1 Power Plant Model	13
2.1.1 Representative Plant Model	13
2.1.2 Adibhatla and Kaushik Configuration	20
2.1.3 Representative Model Validation	20
2.2 Solar Resource	23
2.2.1 NSRDB Data	23
2.2.2 Solar Data Processing	23
2.2.3 Technology References	24
2.2.4 Solar Field Simulation	29
2.3 Solar Integration Model	31
2.4 Solar Contribution	33
2.5 Financial Model	35
2.6 Optimization	37
Chapter 3 Results	45
3.1 Solar Contribution	45
3.2 Financial	46
3.3 Optimization	50
3.4 Geography	52
Chapter 4 Conclusion	55
Chapter 5 Future Work	59
5.1 Partial FWH Bypass	59
5.2 Minimum Spacing	59

5.3	Retrofit vs. Initial Construction	60
5.4	Natural Gas Hybrids	60
5.5	Photovoltaic Hybrids	61
5.6	Thermal Energy Storage	62
REFERENCES		63
Appendix A Solar Contribution		A-1
A.1	Introduction	A-1
A.2	Method	A-1
A.2.1	Equation for Calculation of Solar Contribution	A-2
A.2.2	Solar Heat Exchange Exergy Flow	A-2
A.2.3	Division of Subsystems	A-2
A.2.4	Calculation of Solar Proportion of Work Output	A-4
A.2.5	Calculation of Exergy Destruction	A-6
A.3	Results	A-7
A.4	Conclusion	A-9
Appendix B State Properties		B-1
Appendix C HP FWH Extraction		C-1
C.1	Overview	C-1
C.2	Methods	C-1
C.3	Results	C-3
C.4	Discussion	C-3
C.5	Conclusion	C-4
Appendix D Financial Parameters		D-1
D.1	Introduction	D-1
D.2	Method	D-1
D.2.1	Methods of LCOE Calculation	D-1
D.2.2	Model and Input Adjustments for Hybridization	D-7
D.3	Results	D-10
D.4	Conclusion	D-12
Appendix E NSRDB Data		E-1
Appendix F Correlations		F-1
Appendix G Solar Integration Configurations and Subsystems		G-1
Appendix H MATLAB Functions		H-1
H.1	Optimization	H-1
H.2	Solar Integration	H-4
H.3	Solar Contribution	H-21

H.4 Solar Data H-26
H.5 Solar Field Simulation H-34
H.6 Financial Model H-37

LIST OF TABLES

1.1	List of the world hybrid power plants. On average, CSP contributes 5% of the power generated in these hybrid plants [24, 33]	10
2.1	Results of applying the representative plant model to the Hunter 3 Unit and the data provided in Adibhatla and Kaushik [28].	21
2.2	Solar field comparison of existing CSP plants [33].	25
2.3	Typical dimensions for one CSP module used in power plants currently in operation [33]	26
2.4	Properties for common HTF used in CSP systems.	28
2.5	Effect of technology and maximum loop length ($L_{l,max}$) on receiver area (A_r) and solar field size (A_{sf})	32
2.6	Selected input values used for the cash flow cost analysis	36
3.1	Results for solar contribution based on FWH number and the solar augment fraction (k). Compare with results for $k = 0\%$ in Table 2.1.	46
3.2	Optimums at for each FWH bypass option for $\omega_1 = 0.2$, $\omega_2 = 0.8$, and 16 USD sh.tn. ⁻¹ carbon tax. f is a minimizing function, so the smallest value (or most negative) is considered the best.	52
3.3	Effect of geography on hybrid performance. Castle Dale, UT is the benchmark with Cleveland, OH and El Paso, TX as examples of lower and upper DNI, respectively. Local tax and financing parameters are not included.	53
C.1	Comparison of HP FWH extraction steam design options 2 and 3 to calculated performance parameters for the Hunter plant.	C-3
D.1	Default values for FCR LCOE excluded in Table 2.6	D-7
D.2	Methods used to calculate the capital cost.	D-8
D.3	Calculated values for Capital Cost (CC), LCOE, and payback time (PBT).	D-11
E.1	6/25/2018 Meteorological data for Castle Dale, UT. Downloaded from NSRDB [46]	E-1
F.1	Correlation property equations for use in the representative model. Properties generally follow a power law relationship ($\mathcal{P} = aP_{s1}^b + c$) where P_{s1} is in MPa. Constant properties are shown where $a = b = 0$	F-12

LIST OF FIGURES

1.1	Line focusing technology: a) Parabolic Trough Collector and b) Linear Fresnel Reflector [14].	5
1.2	Point focusing technology: Solar Tower [14]	6
2.1	Schematic of the representative plant model analyzed in this study.	14
2.2	Simplified heat engine schematic. The system of interest is enclosed by the dashed circle.	18
2.3	Schematic for the power plant analyzed in Adibhatla and Kaushik [28]	21
2.4	T-s diagrams comparing the performance of the representative model with (a) Hunter 3 Unit and (b) data in Adibhatla and Kaushik [28].	22
2.5	Sample PTC solar field array nomenclature.	25
2.6	Sample solar integration model. Solar thermal energy is transferred from the solar field to the power block working fluid through a solar heat exchanger (SX) at one of the integration options A-D (Option A shown here in series before the low pressure feedwater heater (LP FWH).	33
2.7	(a) Subsystem division for LP FWH1 or FWH 2 bypass and (b) T-s plot of \dot{W}_s for FWH 7 bypass at $k=1\%$	34
2.8	Overview of the interchange of parameters within the hybrid model. Bold rectangles indicate computational models with arrows connecting the necessary inputs and the reported outputs. Input and output variables are contained within rounded rectangles.	38
2.9	Visualization of the exhaustive search implemented in determining the optimal k (k_{opt}) for each technology/FWH combination.	40
2.10	Behavior of \dot{Q}_{fo} . FWH 1 and FWH 2 bypass does not show a decrease in fuel consumption. Other bypass options only reduce fuel consumption once $k > k_{FWH}$	42
3.1	Variation in LCOE with augment fraction, k . The LCOE for each FWH generally increases in the order $1 \approx 2 < 3 < 5 \approx 6 < 7$ as shown in the insert.	47
3.2	Calculated PBT1 for solar integration at HP FWHs with 0 USD sh.tn. ⁻¹ carbon tax. The horizontal line at PBT1=30 years signifies the typical life of coal power plant.	48
3.3	Effect of carbon tax on (a) LCOE and (b) PBT1. FWH 6 is used as an example of HP integration. LCOE and PBT1 trends for other bypass options are similar to those shown in Figures 3.1 and 3.2.	49
3.4	Effect of green premium price and k on PBT1.	50
3.5	Pareto fronts for HP FWH bypass displaying the competing optimization objectives for the current study and 16 USD sh.tn. ⁻¹ carbon tax. A minimum in OBJ1 corresponds to a maximum in OBJ2 and vice-versa for each FWH option.	51
A.1	CSP-coal hybrid power plant diagram with subsystem divisions for bypass of FWHs 1 & 2	A-3
A.2	Temperature vs entropy plot of main loop of CSP-coal hybrid power plant subsystems.	A-4
A.3	Temperature vs entropy plot of main loop of CSP-coal hybrid power plant subsystems demonstrating the calculation of reversible work for subsystem i	A-5

A.4	Temperature vs entropy plot for FWH 3 bypass with an augment fraction of $k = 3\%$ (a) and FWH 7 bypass with an augment fraction of $k = 3\%$ (b).	A-8
A.5	Temperature vs entropy plot for FWH 7 bypass with an augment fraction of $k = 1\%$ (a) and FWH 7 bypass with an augment fraction of $k = 6\%$ (b).	A-8
B.1	Generalized schematic to illustrate the process of calculating the mass-averaged pressure used in the simplified model.	B-5
C.1	Schematics for the three options considered for HP FWH extraction modeling: (a) HPT exhaust pressure, (b) throttled steam extracted from HPT exhaust, and (c) extraction from IPT.	C-2
C.2	CSP-coal hybrid power plant as published in Li et al. [107]. Two steam lines are extracted from the HPT for feedwater heating.	C-4
D.1	Comparison of capital cost data and calculated capital costs from financial model. . .	D-11
F.1	Boiler inlet pressure data and correlation to HPT 1 st stage pressure.	F-1
F.2	Main steam pressure data and correlation to HPT 1 st stage pressure.	F-2
F.3	FWH 6 data and constant average value	F-3
F.4	FWH 5 pressure ratio data and correlation to HPT 1 st stage pressure.	F-4
F.5	IPT pressure ratio data and correlation to HPT 1 st stage pressure.	F-5
F.6	DA pressure ratio data and correlation to HPT 1 st stage pressure.	F-6
F.7	FWH 3 pressure ratio data and correlation to HPT 1 st stage pressure.	F-7
F.8	FWH 3 pressure ratio data and correlation to HPT 1 st stage pressure.	F-8
F.9	LPT pressure ratio data and correlation to HPT 1 st stage pressure.	F-9
F.10	Boiler inlet mass flow rate data and correlation with respect to HPT 1 st stage pressure. .	F-10
F.11	DA inlet mass flow rate data and correlation with respect to HPT 1 st stage pressure. . .	F-11
G.1	FWH 1 or FWH 2 bypass solar integration configuration.	G-1
G.2	FWH 3 bypass solar integration configuration.	G-2
G.3	FWH 5 or FWH 6 bypass solar integration configuration.	G-3
G.4	FWH 7 bypass solar integration configuration.	G-4
G.5	Subsystem division for SX Model integration at FWH 1 or FWH 2 bypass.	G-5
G.6	Subsystem division for SX Model integration at FWH 3 bypass.	G-6
G.7	Subsystem division for SX Model integration at FWH 5 or FWH 6 bypass.. . . .	G-7
G.8	Subsystem division for SX Model integration at FWH 7 bypass.	G-8

NOMENCLATURE

Acronyms

BFP	Boiler Feed Pump
BFPT	Boiler Feed Pump Turbine
CC	Capital Cost
CO ₂	Carbon Dioxide
CP	Condensate Pump
CSDNI	Clear Sky Direct Normal Insolation [W m^{-2}]
CSP	Concentrating Solar Power
DA	Deaerator
DC	Drain Cooler
DNI	Direct Normal Insolation [W m^{-2}]
EPRI	Electric Power Research Institute
FE	Fuel Earnings [USD]
FS	Fuel Saving
FWH	Feedwater Heater
GHG	Greenhouse Gas
HP	High Pressure
HPT	High Pressure Turbine
HTF	Heat Transfer Fluid
IPT	Intermediate Pressure Turbine
ISCC	Integrated Solar Combined Cycle
LCOE	Levelized Cost of Electricity [USD kWh^{-1}]
LFR	Linear Fresnel Reflector
LP	Low Pressure
LPT	Low Pressure Turbine
NG	Natural Gas
NREL	National Renewable Energy Laboratory
NSRDB	National Solar Resource Database
O&M	Operation & Maintenance
OBJ	Objective
PB	Power Boost
PBT	Payback Time [years]
PTC	Parabolic Trough Collector
PV	Photovoltaic
PVT	Photovoltaic-Thermal
SAM	System Advisor Model
SCA	Solar Collection Assembly
SI	Solar Integration
SX	Solar Exchange
TES	Thermal Energy Storage

Variables

\dot{Q}_B	Boiler Heating Power [MW]
-------------	---------------------------

\dot{Q}_{fo}	Thermal Equivalent of Fuel Offset [MW]
\dot{W}	Mechanical Power [MW]
η	Efficiency [%]
η_c	CSP Collection Efficiency [%]
η_{su}	Solar Use Efficiency [%]
η_{th}	Thermal Efficiency [%]
η_{II}	2 nd Law Efficiency [%]
ω	Optimization Objective Weight [-]
A	Area [m ²]
C	Cost [USD]
$c_{p,s}$	Specific Heat of Solar Heat Transfer Fluid [kJ kg ⁻¹ K ⁻¹]
d_r	Receiver Diameter [m]
E	Total Energy [kWh]
F	Conversion Factor
f	Optimization Objective [kW ⁻¹]
h	Specific Enthalpy [kJ kg ⁻¹]
h_{sun}	Useful Solar Time [hours day ⁻¹]
k	Augment Fraction [%]
L	Length [m]
\dot{m}	Mass Flow Rate [kg s ⁻¹]
m_{ef}	Mass Extraction Fraction []
N_l	Number of Solar Field Loops
N_a	Number of Solar Collection Assemblies per Loop
P_{s1}	HPT 1 st Stage Pressure [MPa]
r	Rate or Ratio
s	Specific Entropy [kJ kg ⁻¹ K ⁻¹]
T	Temperature [K]
T_0	Dead State Temperature [K]
W_p	Aperture Width [m]
\dot{X}	Exergy Rate [kW]

Subscripts

[] _c	Concentration Property
[] _d	Discount Property
[] _n	Annual Value
[] _p	Aperture Property
[] _r	Solar Receiver Property
[] _s	Solar Field/Solar Contribution
[] _{net}	Net Property
[] _{opt}	Optimum Property

Financial Variables (Appendix D)

A	Cumulative Cash Flow
FCR	Fixed Charge Rate

DC	Direct Costs
C_{exp}	Operation and Maintenance Expenses
C_{FOM}	Fixed Operation and Maintenance Costs
C_{ins}	Insurance Costs
$C_{P\&I}$	Principle and Interest Payment
$C_{t,prp}$	Property Tax Costs
C_{VOM}	Variable Operation and Maintenance Costs
CFF	Construction Factor
CRF	Capital Recover Factor
EPC	Engineering-Procurement-Construction
F_L	Debt Fraction
FS	Fuel Savings
IC	Indirect Costs
IRR	Internal Rate of Return
ITC	Investment Tax Credit
$L_{net,0}$	Initial Loan Balance
N_L	Loan Period
PFF	Project Factor
PTC	Project Tax Credit
r_d	Discount Rate
r_i	Inflation Rate
r_{int}	Loan Interest Rate
S	Savings
SC_{dep}	Depreciation Schedule
WACC	Weighted Average of Component Costs
[] _{an}	Annual
[] _{con}	Construction
[] _{cont}	Contingency
[] _{Fed}	Federal
[] _{nom}	Nominal
[] _r	Real
[] _{sal}	Sales
[] _{SI}	Site Improvements
[] _{st}	State
[] _t	Tax

CHAPTER 1. INTRODUCTION

1.1 Fossil Fuel vs. Renewable Energy

Fossil fuels have proven to be reliable sources of power for a developing world, accounting for 10-12% of the energy provided in the US every year since 2010 [1]. Energy consumption in developing countries has been projected to increase at a rate of 3% per year [2]. As the number of people in need of electricity continues to climb, the availability of resources capable of power generation becomes a paramount concern. Additionally, the effect of CO₂ and other greenhouse gas (GHG) emissions from power plants on the environment and global health needs to be addressed. These concerns lead to regulations that loom over fossil fuel power plants forcing innovation in cleaning emissions and improving efficiency.

Concerns with fossil fuels have sparked an ongoing debate, the result of which has been the dramatic increase in power generation using renewable resources such as wind and solar, with increases from 2018-2019 of 140 and 100 trillion BTU, respectively [1]. At first glance, renewable plants seem to solve all the problems associated with fossil fuels in that the resources are naturally occurring, renewable, and the process for the conversion of the energy to useful power does not provide harmful emissions.

However, renewable plants are not without drawbacks. The ability to harness a resource is completely dependent on location. Additionally, renewable power plants tend to have very high capital costs including transmission, land allocation, and thermal energy storage (TES) that is often used to meet grid demands when the resource is unavailable or production is inefficient. High capital costs and low efficiency power generation increase the levelized cost of electricity, or LCOE (measured in USD/kWh). Capital costs for natural gas combined cycles are approximately 1,000 USD kW⁻¹ compared to 2,000 USD kW⁻¹ for on shore wind and 2,600 USD kW⁻¹ for photovoltaic systems [3]. Conversion efficiencies for combined cycles can approach 60% while wind turbines range from 30-40% efficient and photovoltaic panels are typically 10-25% efficient; [4]. Effective

locations for resources such as wind and solar are in places that are not densely populated, thus requiring power transmission. Solar plants do not have a high yield because the conversion process is simply not efficient enough. Therefore, large plots of land must be allocated for one plant to support a community. In the US, coal power plants occupy 12.21 ac MW^{-1} compared to solar (43.5 ac MW^{-1}) and wind (70.64 ac MW^{-1}) [5]. In conjunction with the large scales that typically accompany renewable power plants, the cost of development is driven even higher by the wide use of relatively experimental technology. Perhaps the biggest drawback to renewable plants is intermittency. Power generation from wind peaks in the evening when there are large thermal gradients through canyons, but power consumption is typically lowest in the evenings. Solar power is only effective when the sun is visible which presents problems during cloud cover or in the evening. These high costs and intermittency can preclude the penetration of renewable energy systems into many markets [6, 7].

One solution proposed in 1975 [8] and further explored in 1993 [9] is to break out of the fossil-renewable dichotomy and implement hybrid power plants. The source energy for hybrid power plants may be either predominantly fossil-fuel with renewable augmentation or predominantly renewable with fossil-fuel augmentation. A baseload plant is one that continuously supplies at least the minimum amount of power required throughout the year. The integration of renewable and fossil fuel sources is able to maintain the necessary energy supply when the renewable resource availability drops and reduce the amount of carbon-based fuel used with its associated emissions. Concentrating solar power (CSP) and wind power are the best options for hybridization because both resources are more universally prevalent than other sources such as geothermal or tidal power. While wind power plants are limited by the average speed of the local wind, solar radiation can be used anywhere in the world with varying degrees of efficiency making CSP the most popular candidate for hybridization. Since 1993, hybridization has gained substantial international attention and is often discussed in current literature.

1.2 Evaluating CSP Hybridization Potential

Turchi et al. at National Renewable Energy Laboratory (NREL) have developed a method to evaluate hybridization potential for fossil fueled power plants [10]. The method compiles weighted parameters including plant age, capacity factor, annual average direct normal irradiation (DNI),

available land and slope of the land, and the expected solar use efficiency. The plants are then rated as Excellent, Good, Fair, or Not Considered based on comparative scores.

The most important category by weight in the NREL study was DNI (35%). Of the 22 states evaluated in the study, Texas, Arizona, and Florida have the most total hybridization potential, but only Arizona, Nevada, California, and New Mexico have plants that qualify as Excellent. According to the National Solar Radiation Database at NREL.gov, the latter 4 states also record the highest average annual DNI, improving the hybridization score.

After DNI, normal operating plant capacity factor is the next important category (20%). The solar integration discussed in this and an NREL study is most effective for baseload plants (capacity factor > 50%) because capital costs can only be repaid as more power is generated. Baseload plants are operating more and will thus repay the capital comparatively faster than intermediate or peaking plants (capacity factor < 50%).

The land to be used for the collectors (15%) is of interest because the area available can severely limit the collector area or technology selection depending on the desired solar thermal input. Additionally, land with too steep of a grade can inhibit the collector from effectively tracking the sun.

Finally, solar use efficiency (10%), and age of the plant (5%) are weighted as the least important parameters. Solar use efficiency is the ratio of power generated by solar contribution to the amount of energy absorbed by the collectors ($\eta_{su} = MW_e / MW_{th}$). A low weight for solar use efficiency seems counter-intuitive, but is in place to avoid penalizing plants with large solar collection area that typically result in lower solar use efficiency. The main purpose in hybridization is to reduce fossil fuel consumption and overall GHG emissions, so while increasing solar collector area can have a negative impact on solar use efficiency, it has an overall positive impact on the pursuit of increasing renewable power generation.

1.3 Hybridization capabilities

The NREL study only focused on power plants that used fossil fuels, but CSP can be used to augment any power generation method. Pramanik and Ravikrishna reviewed the CSP technologies available for hybridization with fossil fuel plants as well as with biomass, geothermal, and wind power plants and assigned each combination to a hybrid ranking from low to high. High solar

hybrids used CSP to supplement fuel from biomass, geothermal, and other plants that are already considered renewable. Medium solar hybrids combine CSP and natural gas as only a supplemental fuel limited to 15-25% to meet spikes in consumption. Low solar hybrids, the focus of this current study, use up to 20% CSP to supplement typically coal or natural gas fired Brayton cycles [11].

There are several medium solar hybrid systems in operation today. The Solar Electric Generating Systems in California are a collection of nine parabolic trough CSP plants, eight of which use natural gas as a backup resource. This backup fuel is used to offset volume required for the TES otherwise necessary in medium hybrid systems. Medium systems leave the designer with a choice between low LCOE and low GHG emissions. Increasing the amount of solar collector area will decrease GHG emissions and the amount of fossil fuel required to meet market demands but increase LCOE. Limiting collecting area will require more fossil fuel supplementation which decreases LCOE but increases GHG emissions. Fossil fuels consist of 15-25% of the source energy consumed in medium systems though individual analysis and optimization must be performed for each plant and geographic location.

Low solar hybrid systems consist of solar-Brayton cycles, integrated solar combined cycles (ISCC), and solar-aided coal cycles. Solar-Brayton cycles use the solar thermal technology to preheat or superheat the working fluid of the power cycle. Fossil fuels are still burned, but the preheating or superheating increases power output and thermal efficiency. ISCC use heat exchangers to transfer the solar thermal energy to the working fluid. Solar-aided coal cycles without regeneration often use solar thermal energy to heat the working fluid in place of the steam that is bled off in standard plants. The results for integration in combined cycles and coal plants are similar to solar-Brayton, but further analysis is required to evaluate top cycle versus bottom cycle integration for ISCC. Care must also be given when designing the solar collection area for solar-aided coal plants if the solar thermal energy is used for feedwater heating because there exists an optimal collection area such that more collection area does not contribute any more to the coal cycle. Using CSP to augment coal power plants is of interest because of the higher amount of GHG emissions per unit energy, compared with natural gas [12].

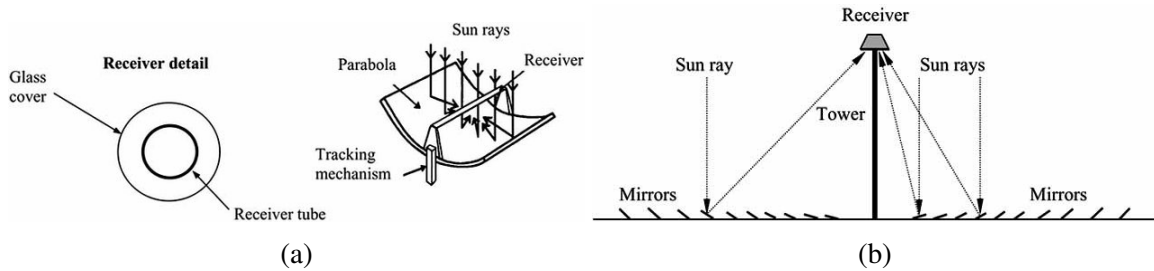


Figure 1.1: Line focusing technology: a) Parabolic Trough Collector and b) Linear Fresnel Reflector [14].

1.4 CSP Technology

There are three technologies commonly used for solar thermal applications: Parabolic Trough Collector (PTC), Solar Tower, and Linear Fresnel Reflector (LFR). PTC have been in production for at least 100 years since Frank Shuman used them to heat steam to power an irrigation pump in Egypt in 1916 [13]. Since then, PTC have benefited from extensive research that has improved performance and reduced cost to the point that PTC now owns 94% of the CSP market share. PTC operate based on geometric properties of parabolas. Any normal radiation will reflect off the parabolic mirrors and concentrate on the collector tube running along the geometric focus. The power concentrated on the collector will heat the solar heat transfer fluid (HTF) that will be sent to integrate with the fossil-fueled power plant.

Solar Tower and LFR have not undergone as much development as PTC but are still viable options for CSP as stand-alone plants as well as in hybrid plants. Solar towers use a circular array of mirrors that track the sun such that the radiation is concentrated on a collector area on top of a central tower. There are a growing number of CSP plants using Solar Tower technology in operation or in production. Because Solar Tower technology is still relatively new, it comes with considerable financial risk, but with more plants in operation, better and cheaper iterations will be developed eventually reducing the LCOE over time.

Like solar towers, few plants are in operation that use LFR, partly due to a lack of TES development for LFR. However, LFR operate based on very simple principles. Unlike PTC, LFR use a linear array of flat mirrors to focus the solar radiation on a collector tube. It is likely that LFR technology will see substantial improvements due to the simple operation principles and the

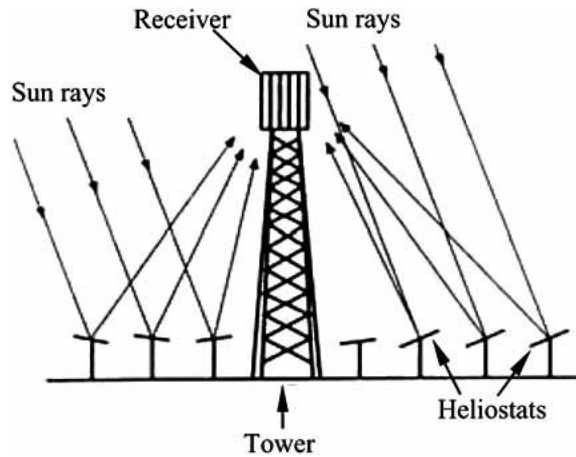


Figure 1.2: Point focusing technology: Solar Tower [14]

lowest cleaning water requirements of the other 2 technologies. For now, however, LFR is the least common of these three technologies.

Peterseim et al. did an extensive study evaluating the contribution of each technology to a specified hybridization model [15]. Each technology was evaluated for feasibility, risk, environmental impact, and LCOE with weighted scores assigned to each category. The weights were determined by the average response from 40 experts in the energy field. Of all the categories, LCOE was considered most important followed by risk reduction and feasibility with impact reduction considered least important. After data was collected on operating parameters for each technology, it was shown that Solar Tower technology is the clear choice for high pressure integration at temperatures above 500 °C. However, Tower technology only scores well for the extreme requirements because it is expensive, which raises its LCOE. The other technologies require much more area to generate the same integration conditions which is why Tower technology only becomes viable as more collector area is required. LFR and PTC both scored well in the low to mid temperature ranges (about 380 °C - 450 °C). PTC scores well due to maturity and LFR scores well due to efficient land use and comparatively low cleaning water consumption.

1.5 CSP Integration Options

The Electric Power Research Institute (EPRI) conducted a study on different integration locations for coal and natural gas hybrid plants and ranked the suggested integration points by

solar use efficiency [16]. The integration points for NGCC and coal are listed in the EPRI report. Because this study is focused on coal hybrid plants, only the integration points suggested for coal plants will be considered. For their model, it was determined that high-pressure (HP) superheated steam (about 540 °C) would be the best state to integrate into a coal plant at the main steam header ($\eta_{su} = 43-46\%$), followed by HP slightly superheated steam (about 370 °C) and HP saturated steam (about 350 °C) both integrated at the HP primary superheater inlet ($\eta_{su} = 30-42\%$ and $28-40\%$, respectively), and finally intermediate-pressure (IP) superheated steam (about 370 °C) for cold reheating ($\eta_{su} = 25-28\%$). Because a different technology would probably be ideal for each of the integration points above, a method of optimizing the integration point and technology is required, and should also include an analysis of a hybrid plant expected life cycle.

CSP augmentation of coal power plants offers multiple benefits including a reduction of CO₂ with some of the energy resource coming from a renewable source, a reduction in the overall cost as compared to a stand-alone CSP plant of the same combined capacity, and an increase in availability and capacity relative to a stand-alone CSP plant [17]. CSP integration also results in higher solar-to-electric efficiency, reduced costs for retrofitted projects, higher capacity factors without thermal energy storage, and improved ramping time [18, 19]. Among the various possible applications of CSP hybridization [20], coal is a popular candidate because CSP and coal share many of the same power generation components and because of the large presence of coal throughout the world. However, the possibility of hybridization is affected by more than just thermodynamic performance [21].

1.6 Benefits of CSP-Hybridization

Zhai et al. studied the life cycle of nine power plant combinations for baseload coal, CSP hybrid, and CSP hybrid with TES at 300, 600, and 1000 MW outputs [22]. Zhai et al. separated the life cycle of a CSP hybrid power plant into four phases: Fuel, Operation, Transport, and Materials. The Fuel phase is defined as the process of converting resources into useful fuel. The Operation stage is the actual burning of the fuel. The Transportation phase considers hardware transportation and solar thermal HTF transmission. The Materials stage entails the exploitation and transportation of raw materials.

Each configuration was evaluated from plant construction to the end of the expected life on a weighted sum of objective scores: (1) global warming potential, (2) acidification potential, (3) respiratory effects potential, (4) primary energy consumption, and (5) capital costs. Zhai et al. showed that for each objective value, every hybrid plant performs better than a coal-fired plant with one exception, capital costs. Pure coal plants became economically comparable to hybrid configurations as the weight of capital costs increased and surpassed hybrids with a further increase in the capital weight factor. This means that, when considering hybridization potential, as capital costs become more important and other economic factors such as carbon tax are neglected, hybrid viability decreases. Zhai et al. also shows that GHG emissions, including CO₂ and SO₂, are highest during the Fuel and Operation stages of a plant life. The integration of CSP reduces the fuel required to produce the same amount of power and provides significant environmental benefit to CSP hybrid power plants operating in FS mode such as in Zhai et al.

Manente studied the benefits of hybridization and demonstrated which plant modifications and operating mode would provide an increase of 50 MW_e turbine output power [23]. The plant analyzed was an integrated solar combined cycle which augments the heating for a natural gas combined cycle. Manente classified the operating modes as power boost (PB) and fuel saving (FS). In PB mode, solar augmentation is used to increase the power generation holding fuel consumption constant. The categories of power boost included: no change in plant equipment (PB1); upgrading steam turbines (PB2) to account for significant increases in turbine output; and upgrading both turbines and heat exchangers (PB3) to support the increased heat transfer from the solar collectors and loads on the turbine. In FS mode, solar augmentation is used to hold power generation constant and decrease fuel consumption. FS mode configurations were evaluated for configurations that required no equipment changes (FS1) and for the case of an upgraded turbine (FS2). The highest power output increase from solar augmentation was from PB3, but overall plant efficiency was highest for PB1. PB1 also required less solar collection area (SCA) and was comparable to PB2 and PB3 in both radiation and thermal-to-electric efficiencies. FS1 required slightly more augmentation than PB1, but provided a greater power boost and higher solar radiation-to-thermal efficiency. The hybrid power plants evaluated in this study will be assumed to operate in FS mode, or net power output will remain constant and the amount of fuel consumption will vary.

Both Behar et al. [24] and Libby [16] suggest that, among other options, solar can be integrated at a feedwater heater (FWH) where steam, extracted from a turbine, is typically used to preheat some other working fluid. Downstream effects can be mitigated by selecting the augment fraction such that the heat transfer limits of the FWH are not surpassed. This method is known as FWH bypass and has been shown to be a feasible candidate for CSP-coal hybridization [17,25–28]. Like the integrated solar combined cycles discussed in Manente [23], coal plants can integrate solar thermal energy by means of FWH bypass and operate in FS mode.

1.7 Existing CSP Hybrid Power Plants

Okoroigwe and Mdhlopa summarized solar hybrid sites around the world according to the date of the Okoroigwe and Madhlopa publication (2016) [29]. There are currently 12 CSP hybrid plants throughout the world in operation or under construction [11, 30, 31]. All operational plants use parabolic trough collectors (PTC) and offset natural gas with the exception of the Dadri Hybrid Plant in India (under construction) which will be the only hybrid plant in operation to use linear Fresnel reflectors (LFR) and the only plant augmenting coal [32]. Previously, the Liddell Power Station in Australia used LFR to offset coal, but the CSP addition was non operational as of 2017 [33]. Similarly, the Palmdale hybrid plant (Palmdale, CA) was amended to no longer include CSP because the CSP plant was never built [34] and has since been canceled altogether and the Victorville hybrid was also cancelled, allegedly due to economic trouble, suspected wasteful spending, and lack of a partner [35]. Since Behar's study, the status of the hybrid planned for Ningxia, China has been suspended [36]. Studies demonstrating the use of CSP in integrated solar combined cycles with natural gas show considerable benefits in hybrid performance [37], but a way for developers to evaluate hybrid feasibility has not been explored.

1.8 Research Objectives

While several studies have demonstrated the process of evaluating hybridization feasibility for specific locations [26, 30, 38–43], there is no known generalized method available to evaluate hybridization feasibility while simultaneously estimating changes in desired parameters such as efficiency, LCOE, and reduction in GHG emissions.

Table 1.1: List of the world hybrid power plants. On average, CSP contributes 5% of the power generated in these hybrid plants [24, 33]

Plant Name (Location)	Tech	Fossil Fuel	Total Output [MW_e]	Solar Contribution [MW_e]
Medicine Hat (Canada)	PTC	NG	203	1.1
Aïn Beni Mathar (Morocco)	PTC	NG	470	20
Hassi R'mel (Algeria)	PTC	NG	150	20
Kuraymat (Egypt)	PTC	NG	140	20
Martin Next Generation (Florida, USA)	PTC	NG	1150	75
Archimede (Italy)	PTC	NG	130	5
Yazd* (Iran)	PTC	NG	467	17
Al-Abdaliyah* (Kuwait)	PTC	NG	280	60
Waad Al Shamal* (Saudi Arabia)	PTC	NG	1390	50
Agua Prieta II* (Mexico)	PTC	NG	478	12
Duba 1* (Saudi Arabia)	PTC	NG	605	43
Dadri* (India)	LFR	Coal	490	14

*Plant under construction

The purpose of this study is to develop and demonstrate a generalized method for evaluating CSP-coal hybrid feasibility based on thermoeconomic performance that can be applied to any coal power plant with feedwater heating and reheating. A representative model of coal power plants is presented and validated by data available in archival literature. The methods of estimating solar resource, solar field size, and financial performance are described. Optimization methods are shown with discussion about fitness function development including the calculation of solar contribution (\dot{W}_s) to plant power output. The optimization methods are demonstrated using Hunter Unit 3 in Castle Dale, UT as a representative coal power plant. This study focuses primarily on retrofit projects and is most related to fuel saving mode [23] to reduce the cost and complexity of retrofitting a power plant with solar collectors while still increasing efficiency.

CHAPTER 2. METHODS

Each coal plant differs from the next, but several hardware components are common to most power plant configurations. A representative plant model is developed that generally operates in a similar way to most coal plants but with simplifications that make it applicable to most coal plants. The solar integration model developed in this study, consisting of the representative plant and solar exchange (SX) model, assumes the coal plant of interest has at least one FWH in the low pressure (LP condensate stage and one FWH in the high pressure (HP) feedwater stage. Specific examples are calculated based on data for the Hunter Unit 3 in Castle Dale, UT Provided by PacifiCorp and validated where possible by data published in archival literature.

2.1 Power Plant Model

There are several power generation components that are consistently used in coal power plant configurations:

- Multiple turbines (Typically high, intermediate, and low pressure turbines)
- High pressure feedwater heating (HP FWH) from high and intermediate pressure turbines' (HPT and IPT, respectively) extraction and exhaust steam
- HPT exhaust reheating
- Low pressure feedwater heating (LP FWH) from low pressure turbine (LPT) extraction steam

2.1.1 Representative Plant Model

Each coal plant differs from the next, but several hardware components are common to most power plant configurations. The Hunter 3 Unit includes all of the standard components identified in the introduction. Data made available by PacifiCorp on the Hunter Unit performance provides a reliable source to benchmark the representative model introduced in this report.

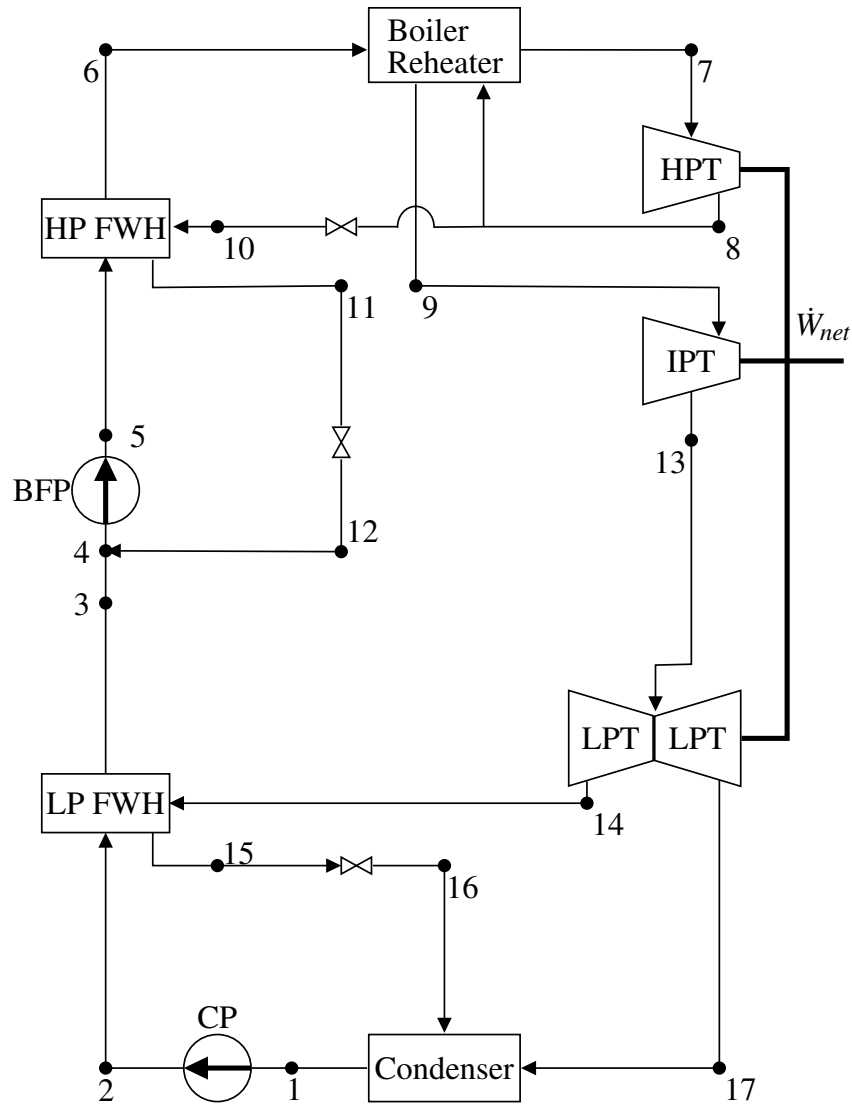


Figure 2.1: Schematic of the representative plant model analyzed in this study.

Justification for the plant simplification is provided below. First, the thermodynamic principles that allow the simplification are described. Then the methods used to extract or calculate representative model inputs are explained. Finally, possible sources of error are discussed.

Combining Feedwater Heaters

As noted in Chapter 1, FWHs are common points of access for solar heating so attention is given to modeling the FWH processes accurately. The major focus of the plant simplification

centered around reducing the number of FWHs and the amount of steam and the pressure at which the steam is extracted to run the FWHs.

The FWHs used in the representative plant model are modeled as open FWHs, similar to those found in published articles and in the Hunter heat balance diagram. The drain cooler (DC) is used to fix the operating parameters in the representative plant model. The DC sets the temperature difference between the drain outlet and the FWH inlet streams.

A mass-averaged approach is used to approximate the DC for both the HP and LP FWH. As a sample case, consider a system of three LP FWHs that extract steam from the LPT at three different pressures. The extraction mass flow rates are converted to percentages of the total mass of steam extracted for that stage. Each LPT extraction is divided by the total mass flow rate from the three LPT extraction streams to obtain mass fractions A, B, and C (where $A+B+C=1$). The overall DC is determined by multiplying each mass fraction (A, B, and C) by its corresponding FWH DC and adding the three mass fraction-DC products. If the hypothetical FWHs have a DC of 5 (stream A), 7 (stream B), and 10 (stream C) °C, then the overall DC to be used in the representative plant model would be $DC = 5A + 7B + 10C$. This process is repeated for the HP FWH overall DC and both LP and HP DC.

It is efficient to incrementally heat the feedwater in multiple stages where the temperature of the extracted steam increases alongside the increase in pressure stage. The pressure of the feedwater ideally does not change significantly as it passes through each FWH. Each FWH can then be modeled as a simplified, isobaric heating process. There are changes to the exergy destruction when the feedwater is not heated incrementally by progressively higher temperatures, but the FWHs are modeled as a single heating process.

As can be seen in Choudhary [44], heat transfer devices (FWHs and boiler) are significant sources of entropy generation, so reducing the number of and operating parameters for the FWHs is expected to have a non-negligible impact on the overall entropy generated in the cycle and, consequently, the 2nd law efficiency. This change in entropy generation will be captured in calculations of \dot{W}_s (Appendix A).

Boiler Feed Pump Turbine

The inlet and exhaust pressures of the boiler feed pump turbine (BFPT) are the same as the LPT inlet and exhaust. Rather than modeling a branch from the IPT exhaust, the amount of steam that would go through the BFPT is sent through the LPT. To compensate for the additional mass going through the LPT, the power required for the BFP is added to the gross work output requirement from the representative model.

Steam Extraction Selection

From the Hunter heat balance diagram and the Adibhatla and Kaushik schematic [28], all LP FWHs use extracted steam from the LPT. The steam used for the LP FWH in the representative model should be steam extracted from the LPT. The mass-averaged pressure of the extraction lines in the Hunter plant is used as the extraction pressure in the representative model. More detail about how the mass-average method is applied to calculate the extraction steam pressure is presented in Appendix B.

The HP FWHs in coal plants use varying combinations of steam extracted from both the HPT and IPT. The representative model assumes that the HP FWH uses steam extracted from the HPT exhaust before the reheat process and is throttled to the mass-averaged pressure. The inclusion of the throttling valve adds entropy generation unique to the representative model. Compared to modeling the HP FWH steam as extraction from the IPT in the representative model, throttling the HPT exhaust to the mass-averaged pressure was selected to achieve model accuracy and preserve simplicity. More details on the decision between modeling the HP FWH extraction is provided in Appendix C.

The efficiency of each turbine is also determined using the mass-averaged approach between the inlet pressure and each extraction and exhaust pressure. The mass-averaged efficiency and the pressures discussed above are sufficient to determine the other fluid properties throughout the cycle. The methods of calculating each individual state point for the representative model are provided in Appendix B.

Representative Model Simulation

Coal power plants control the total power generation of the cycle by adjusting the HPT 1st stage pressure (P_{s1}) and the working fluid mass flow rate. The representative model was modified to calculate the plant performance, limited by a maximum power output constraint, when allowing bypass of a single FWH by solar heating (i.e. solar bypass). After simulating the turbine power generation with the recalculated extraction pressure, power output constraints for the overall plant and each individual turbine can be compared to the respective calculated values. If a constraint is violated, P_{s1} is incrementally reduced by 5% until all constraints are satisfied.

Changing P_{s1} has downstream effects on the mass flow rate, boiler operating temperature, and pressure ratios between the inlet to a turbine and each respective extraction or exhaust stream. Relationships between P_{s1} and each operating property must be determined and included in the model. Specifically, the properties for which a correlation is required include:

- Condenser pressure
- All FWH extraction pressure ratios
- Boiler inlet pressure
- Boiler outlet pressure
- Boiler operating temperature
- Boiler inlet mass flow rate
- Deaerator (DA) inlet water mass flow rate
- Extraction fractions for each FWH
- HPT, IPT, LPT isentropic efficiencies
- IPT, LPT extraction pressure ratios

Specific correlations for each property listed above are provided in Table F.1 along with a detailed description of how each state point is calculated in Appendix B.

2nd Law Efficiency

The 2nd Law Efficiency (η_{II}) is a value that quantifies the ability of a process to convert its work potential into useful work. Calculating η_{II} requires assuming a dead state, or the conditions at which no further work can be performed. For this analysis, the dead state temperature is assumed

to be equivalent to the saturation temperature inside the condenser. The advantages of this choice will be clarified after the efficiency model is developed.

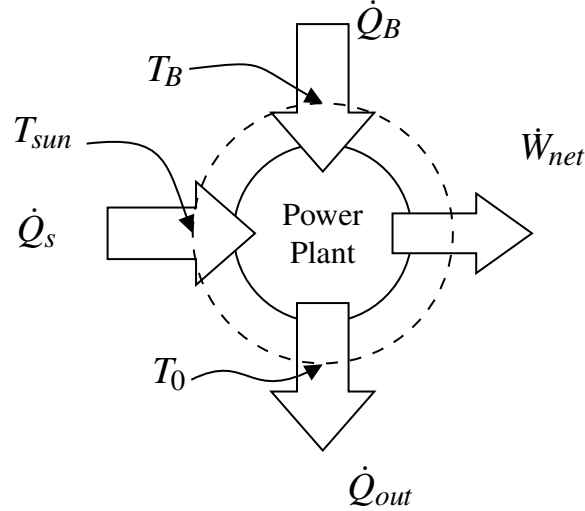


Figure 2.2: Simplified heat engine schematic. The system of interest is enclosed by the dashed circle.

Figure 2.2 shows a simplified heat engine schematic with arrows indicating the exergy interactions that cross the dashed boundary of the power plant: the heating done in the boiler, the net power output, and the energy rejected in the condenser as well as the energy rejected due to inefficiencies in the plant hardware.

The exergy rate for net power out (\dot{X}_W) is equal to the net power out of the cycle (Equation 2.1).

$$\dot{X}_W = \dot{W}_{net} \quad (2.1)$$

The exergy rate for heating is defined in Equation 2.2 [45].

$$\dot{X}_Q = \sum_k^N \left(1 - \frac{T_0}{T_k}\right) \dot{Q}_k \quad (2.2)$$

where T_k is the boundary temperature at which the respective heating (\dot{Q}_k) occurs, T_0 is the temperature of the dead state, and N is the number of heating interactions. For the case of the boiler heating (\dot{Q}_b), the boundary temperature will be the temperature of the flame. Solar heating

is provided by the sun, and to include all exergy destruction within the analysis, the temperature of the sun is used for calculating solar exergy ($T_{\text{sun}}=5800$ K). In this study, it will be assumed that the fuel is Bituminous Coal with an adiabatic flame temperature of 2172 °C. Using the adiabatic flame temperature results in a lower bound for η_{II} . More accurate results can be obtained by using the actual flame temperature for the boiler in the plant of interest. For the energy rejection (\dot{Q}_{out}), it is rejected to the dead state, so $T_k = T_0$ and $\dot{X}_{Q,\text{out}} = 0$.

Analyzing an exergy balance of Figure 2.2,

$$\dot{X}_{\text{sys}} = \dot{X}_{\text{in}} - \dot{X}_{\text{out}} - \dot{X}_d \quad (2.3)$$

where \dot{X}_{sys} and \dot{X}_d are the exergy rates of the whole system and the exergy destruction, respectively. For a plant operating at steady state, $\dot{X}_{\text{sys}} \approx 0$. The remaining balance is

$$\dot{X}_d = \dot{X}_{\text{in}} - \dot{X}_{\text{out}} \quad (2.4)$$

Exergy is added to the system through boiler heating ($\dot{X}_{\text{in}} = \dot{X}_Q$) and exergy leaves the system by net power output ($\dot{X}_{\text{out}} = \dot{X}_W$). η_{II} is defined in Cengel and Boles [45]

$$\eta_{\text{II}} = 1 - \frac{\dot{X}_d}{\dot{X}_{\text{in}}} \quad (2.5)$$

Substituting Equation 2.4 into Equation 2.5 yields

$$\eta_{\text{II}} = 1 - \frac{\dot{X}_{\text{in}} - \dot{X}_{\text{out}}}{\dot{X}_{\text{in}}} \quad (2.6)$$

Finally, simplifying and substituting the definitions for \dot{X}_{in} and \dot{X}_{out} yields Equation 2.7.

$$\eta_{\text{II}} = \frac{\dot{W}_{\text{net}}}{\sum_k^N \left(1 - \frac{T_0}{T_k}\right) \dot{Q}_k} \quad (2.7)$$

With the summation in Equation 2.7, the solar heating is combined with the boiler heating. With the inclusion of CSP heating, boiler heating is reduced as discussed in Section 2.3. However, because the boundary temperature for solar heating is so high, the exergy in from low solar aug-

mentation will increase at a slower rate than the boiler exergy decreases. The expected result is a decrease in η_{II} for low solar augmentation.

While this study analyzes steady state models, the potential use of the models for dynamic simulations is also of interest. Equation 2.7 poses a problem for dynamic simulations when $\sum_k^N \left(1 - \frac{T_0}{T_k}\right) \dot{Q}_k = 0$ as this condition results in $\eta_{II} \rightarrow \infty$. Such a condition is only possible when either $\dot{Q}_k = 0$ or $T_k = T_0$. However, those conditions are unlikely after the plant is operating. After the plant is operating and the CSP field begins collecting energy, there is heating from the boiler and from the solar field (i.e. $\dot{Q}_k \neq 0$). Similarly, if any coal is being burned, the coal flame temperature will always be greater than the temperature of the surroundings, or dead state. And for the case of $\dot{Q}_s > 0$, the boundary temperature used is the sun, as discussed above, and $T_{\text{sun}} > T_0$.

2.1.2 Adibhatla and Kaushik Configuration

The performance of the representative model is validated by comparing power output, heating power input, thermal efficiency, and 2nd law efficiency to actual data from the Hunter 3 Unit heat balance diagram and data published by Adibhatla and Kaushik [28]. The plant analyzed in Adibhatla and Kaushik is a 500 MWe plant with 3 LP FWHs and only 2 HP FWH (Figure 2.3).

Similar to the Hunter 3 Unit, the HPT exhaust and IPT extraction are used for FWH, but the IPT is used in the DA in Adibhatla and Kaushik instead of for a third HP FWH as in Hunter. The number of extraction streams is the same between the two plants, but the exhaust from the Adibhatla and Kaushik LPT goes directly to the condenser as opposed to an LP FWH as in Hunter. These differences will show the versatility of the proposed representative plant model to be applied to coal power plants of varying configurations.

2.1.3 Representative Model Validation

In order to validate the representative model, the power output, boiler heating power, thermal efficiency, and 2nd law efficiency were calculated for the representative plant model and compared to data from Hunter Unit 3 and Adibhatla and Kaushik (Table 2.1) [28].

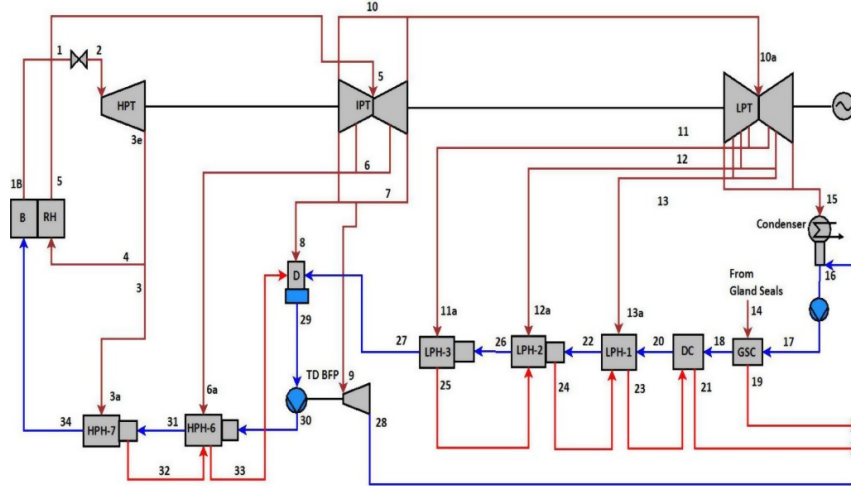


Figure 2.3: Schematic for the power plant analyzed in Adibhatla and Kaushik [28]

		\dot{W}_{net}	\dot{Q}_{in}	η_{th}	η_{II}
		[MW]	[MW]	[%]	[%]
Hunter	Reported Cycle Performance	511	1273	37.3	46.1
	Representative Model	505	1276	39.6	45.1
	Change (%)	-1.2	0.2	6.2	-2.2
Adibhatla & Kaushik	Reported Cycle Performance	500	1300	38.5	44.2
	Representative Model	511	1332	38.3	43.7
	Change (%)	2.2	2.5	-0.4	-1.1

Table 2.1: Results of applying the representative plant model to the Hunter 3 Unit and the data provided in Adibhatla and Kaushik [28].

The largest error is in the thermal efficiency. The thermal efficiency error likely stems from using mass-averaged values and other simplifications listed in this report. Using mass-averaged values approximates the changes in turbine efficiency with flow rate which affects the reported power output. Assuming constant pressure through FWH stages also reduces the power required by the CP and BFP. However, the net power output error is consistent between the two examples, so altering input parameters, e.g. solar augmentation, should have a consistent effect on the reported

net power output. The boiler heating model is more accurate and will closely approximate the heating load on the system and corresponding emissions reduction from solar augmentation.

It is important to also note how the representative model compares to Hunter and Adibhatla and Kaushik's data for the entire cycle in addition to the parameters outlined in Table 2.1. More accurate approximations of the power plant in Adibhatla and Kaushik may be attainable with operating data similar to the data made available for the Hunter Unit 3. Figure 2.4 shows the comparison of the predicted state points from the representative model with the Hunter Unit 3 (Figure 2.4a) and Adibhatla and Kaushik (Figure 2.4b). The representative model sacrifices some accuracy to achieve consistency in modeling power plants with different configurations. Thus, results for this study will be obtained by varying the amount of solar augmentation to produce results that can be compared to each other based on changes in fuel consumption

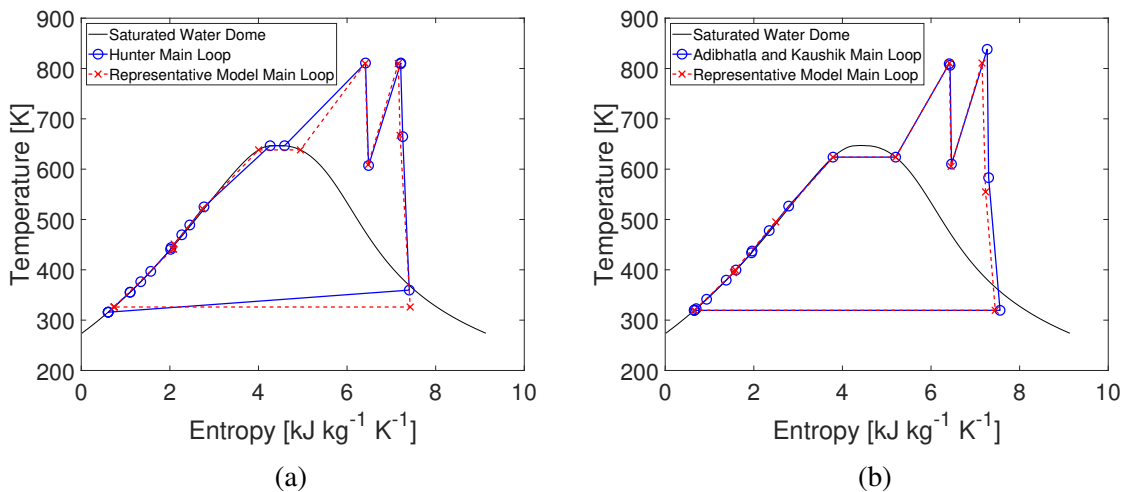


Figure 2.4: T-s diagrams comparing the performance of the representative model with (a) Hunter 3 Unit and (b) data in Adibhatla and Kaushik [28].

One notable difference is the discrepancy between the temperature of the mass entering the condenser of the Hunter Unit, located at the bottom right of the cycle diagram in Figure 2.4a. The data used to define the Hunter Unit main loop is obtained directly from the heat balance diagram. The Hunter operating data suggests the LPT exhaust is actually at a lower pressure than is reported on the diagram. Using experimental data for the LPT exhaust would improve the Hunter

comparison in Figure 2.4a. The error in power output can be seen in Figures 2.4 by the space between the vertical lines on the far right of each diagram denoting the IPT and LPT processes. As noted above, the error in estimates of power generation is expected when mass-averaged values are used for efficiencies. The \dot{W}_{net} error is compounded as the same method of using mass averaged values is applied to all turbines. However, the actual plant and respective model diagrams match well and appear to be consistent, regardless of plant configuration.

2.2 Solar Resource

The amount of solar resource available per unit area is referred to in this study as the direct normal insolation (DNI). Since DNI is susceptible to fluctuations due to weather, the maximum possible DNI for a given time is based on calculations for a clear sky (CSDNI), such that $\text{DNI} \leq \text{CSDNI}$. The following sections describe methods to estimate the expected DNI at any given geography and its use in the SX model.

2.2.1 NSRDB Data

The National Renewable Energy Laboratory (NREL) reports solar resource data in the National Solar Resource Database (NSRDB) [46] for a number of locations in the United States, Canada, and South America. Sengupta et al. describes the method of retrieving data from the online NSRDB data viewer in depth [47]. The NSRDB has data from several meteorological measurements. For the methods described in Section 2.2.2, DNI [W m^{-2}], CSDNI [W m^{-2}], solar zenith angle (θ_z) [degrees], temperature [$^{\circ}\text{C}$], and pressure [mbar] are utilized.

2.2.2 Solar Data Processing

A MATLAB script (Appendix H.4) has been written to process data downloaded from the NSRDB as described below. The average DNI for each day is calculated according to Equation 2.8 where N is the number of possible daylight data points. N is determined for each day by counting the number of data points for which $\text{CSDNI} > 0$.

$$\text{DNI}_{\text{avg}} = \frac{1}{N} \sum_{i=1}^N \text{DNI}_i \quad (2.8)$$

Once the daily average is calculated for each day in the year file, the script then opens the next file, calculates daily averages and adds the averages from the currently open file to the sum of the average values from the previous files. Dividing the data array by the number of data files (or number of years) provides the multiple year daily average for each parameter. The multiple year daily averages are then averaged to generate the total multi-year average. When the multi-year average DNI is multiplied by the multi-year average daylight time (N), the multi-year average solar energy is calculated.

For Castle Dale, UT, the calculated multi-year average DNI and daylight time are 542 W m^{-2} and 11.9 h , respectively. The calculated value for multi-year average solar energy then is 6.45 kWh m^{-2} . The NSRDB reports 6.48 kWh m^{-2} as the nominal energy flux value for Castle Dale, UT. The calculated error then is 0.5% of the reported value by NREL. This multi-year average accounts for days of varying solar resource strength and useful time. For the steady state application in this study, it is assumed that the solar resource is available at the multi-year average DNI for a duration of the multi-year average solar time ($h_{\text{sun}} [\text{hrs day}^{-1}]$).

2.2.3 Technology References

PTC and LFR are both categorized as line-focusing CSP technology because they use mirrors to focus the solar irradiation onto a linear receiver. While the performance of LFR systems are comparable with PTC [48], PTC has had the benefit of design improvements and reduction in equipment costs. While it has been shown that the performance of PTC exceeds that of LFR in hybrid systems [49], LFR is included in this analysis as a secondary feasible hybrid design option.

Collection Equipment

In order to calculate the useful thermal energy transferred from the SX model, it is important to first understand the roles of solar collection geometry and solar field configuration.

For this study, a *solar module* will be defined as the assembly of a single set of individual parts. A PTC module consists of several curved mirrors attached end to end and a receiver tube at the geometric focus of the row of parabolic mirrors and spanning the length of the combined mirrors. A *Solar Collection Assembly* (SCA) is used in this study to describe the assembly of

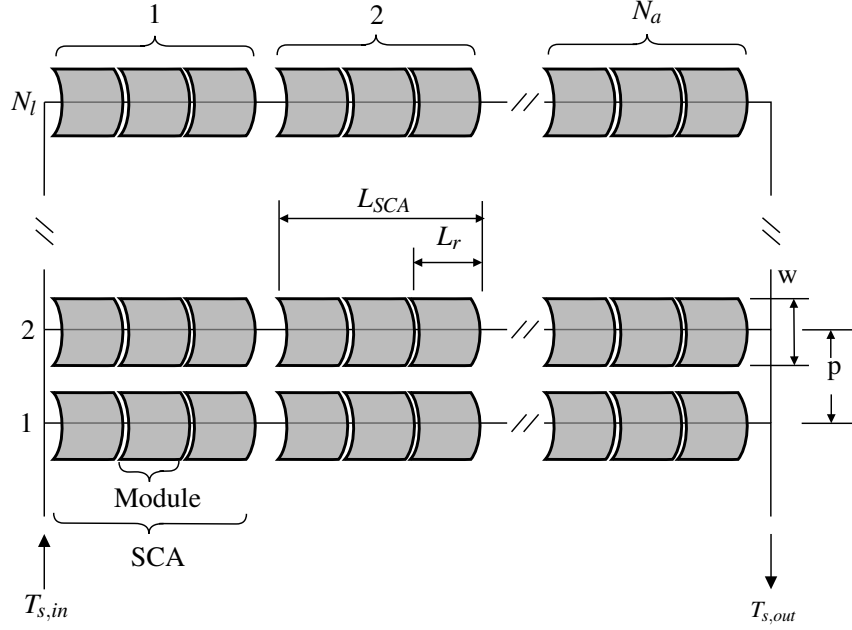


Figure 2.5: Sample PTC solar field array nomenclature.

	Plant Name	L_{SCA} [m]	Configuration $N_l \times N_a$	d_r [m]	W_p [m]
LFR	eLLO	340	1x27	0.08	14
	Puerto Errado 1	806	1x2	0.08	16
PTC	Andasol-1	144	4x156	0.07	5.7
	Aste 1A	150	4x156	0.115	5.4
	Borges	96	6x56	0.115	5.7
	Extresol 1	144	4x156	0.07	5.7
	Enerstar	150	4x105	0.07	5.4
	Godawari	144	4x120	0.07	5.7

Table 2.2: Solar field comparison of existing CSP plants [33].

multiple solar modules. A *loop* is defined as a single row of multiple SCA and includes the tracking technology used to rotate the mirrors. Figure 2.5 illustrates the nomenclature used to describe the solar field in this study.

LFR plants combine several solar modules in series into a continuous loop. PTCs are combined in smaller increments such as 8 or 12 modules per SCA for many of the plants listed in

Table 2.3: Typical dimensions for one CSP module used in power plants currently in operation [33]

Technology	d_r [m]	W_p [m]	r_c	L_r [m]
PTC	0.08	5.6	20	10
LFR	0.08	15	60	10

Table 2.2 [33]. For the current study, dimensions for physical components will be based on those used in the projects listed in Table 2.2. Most projects use a receiver tube from either Siemens (UVAC 2010) or Schott (PTR 70). The eLLO and PE1 plants use SUNCNIM and Novatec Solar assemblies, respectively, which have an average aperture width of $W = 15$ m. Most of the PTC projects listed in Table 2.2 use solar assemblies from Siemens or Sener. The average values from NREL data are included in Table 2.3 and will be used in simulating the solar field area.

The receiver area (A_r) is defined as the area absorbing the radiation. A_r is equivalent to the receiver surface area that is experiencing concentrated solar radiation, using the receiver diameter (d_r) and length (L_r) [50].

$$A_r = \pi d_r L_r \quad (2.9)$$

For LFR systems, the receiver is often covered from above by a trapezoidal reflector (shown in Figure 1.1b) to focus the thermal radiation onto the entire receiver. However, receivers on PTC modules do not absorb concentrated radiation through areas outside the focal area, or the area onto which thermal radiation is concentrated. The focal area depends on the aperture width and curvature of the PTC mirrors. To simplify the analysis in this report, the focal area of PTC modules will be assumed to be approximately equal to A_r , noting that the actual thermal energy collected over this area will be slightly less and accounted for when simulating the configuration of the solar field.

Aperture area (A_p) is defined as the area through which radiation enters the collector. In the case of PTC, A_p is the projected area of the mirror calculated by the product of L_r and the perpendicular opening width (W_p). The A_p for LFR would be the product of the length of each mirror and the width of the overall mirror array.

The goal of CSP technology is to maximize the ratio between A_p and A_r , or concentration ratio (Equation 2.10).

$$r_c = \frac{A_p}{A_r} \quad (2.10)$$

If A_r is 50 times smaller than A_p , the heat flux absorbed by the receiver (q_r'') would be 50 times greater than the solar heat flux (DNI) entering the aperture area (Equation 2.11).

$$q_r'' = r_c \text{DNI} \quad (2.11)$$

Heat Transfer Fluid

CSP systems require a HTF to be pumped through the collection vessel and often use a heat exchanger to move the absorbed thermal energy for use elsewhere. Typical HTFs include air, water, molten solar salts (i.e. NaNO_3 , KNO_3 , etc. [51]), and thermal oils.

Air is a useful HTF due to its availability and versatility. While air does have a lower thermal capacitance compared to the other HTF in Table 2.4, it also avoids complications associated with phase change. The gas properties of air (including viscosity in Table 2.4) make it much easier to pump through a CSP system or compress to allow for a greater change in temperature. The thermal properties reported in Table 2.4 are largely what limit the application of air as a HTF. The specific heat of air is comparable to the other HTFs but for the same temperature difference, the volume of air required to match the mass of the liquid fluids is significantly higher. The thermal conductivity of air is also considerably lower than the liquid alternative HTFs. The drastic increase in thermal performance from using a liquid HTF can reduce the required collection area to offset HTF capital costs that are not present when using air.

Water is also used for its availability as well as its excellent thermal capacity but has a relatively low boiling point. The properties provided in Table 2.4 are for saturated liquid water at 300 °C, which requires the water be compressed to approximately 8.6 MPa. Otherwise, the liquid water may boil which complicates the selection of an appropriate pump and heat exchanger. CSP linear receivers are typically thin-walled to minimize radial temperature differences and may not be suited for the high pressures that would be required to maintain water at a liquid state. Unlike

Table 2.4: Properties for common HTF used in CSP systems.

Fluid at 300 °C	Specific heat [kJ kg⁻¹ K⁻¹]	Thermal Conductivity [mW m⁻¹ K⁻¹]	Viscosity [mPa s]	Reference
Air	1.04	44.41	0.030	[52]
Liquid Water (8.6 MPa)	5.7504	552.65	0.086	[52]
Steam (0.1 MPa)	2.01	43.5	0.020	[52]
Therminol VP-1*	2.314	96.4	0.221	[53]
Nitrate Salt	1.4946	500	3.26	[51]

*Selected as solar collection fluid in this work

liquid water, steam has thermal properties much similar to air and would be less desirable as an HTF for the same reasons discussed above.

Solar salts have high melting points (typ. >300 °C for Nitrate salts) and excellent thermal capacity. However, line focusing technology typically operates close to 300-400 °C [11], often precluding the use of solar salts due to the potential for solidification. Point focusing technologies have higher concentration ratios and can maintain temperatures well above the freezing point of common solar salts. Increased performance has been shown for advanced LFR with solar salts as the heat transfer fluid [54], but the capital costs associated with this design may critically hinder the feasibility of LFR hybridization. Thus, solar salts are most commonly used with point focusing technologies and will not be considered in this study.

Vignarooban et al. performed an extensive study on heat transfer fluids available for CSP systems [55]. The data in Vignarooban et al. suggests that a thermal oil is the ideal choice for the design points in this study. Oils, like Therminol VP-1 from Eastman Chemical Company, are engineered specifically to operate in the temperature range for ideal line-focusing CSP applications [53]. While the thermal properties of oils are less impressive when compared to liquid water or solar salts, thermal oils are most often used due to their stability in typical line-focusing temperature ranges. For this study, properties for Therminol VP-1 will be used for solar collection calculations.

2.2.4 Solar Field Simulation

While the concentration ratio is determined by the installed hardware, the length used for collection can be adjusted. However, a straight line of CSP collectors for several miles is often not desirable so collectors are placed in arrays. For N_l loops of collection, the equation for the thermal power absorbed by the solar field ($q_{\text{abs},f}$) can be related to collection geometry using Equation 2.12.

$$q_{\text{abs},f} = N_l r_c \text{DNI} A_r \quad (2.12)$$

Alternatively, $q_{\text{abs},f}$ can also be calculated using the change in temperature (ΔT_s) and specific heat ($c_{p,s}$) of the solar heat transfer fluid (Equation 2.13) assuming the fluid does not undergo a phase change.

$$q_{\text{abs},f} = \dot{m}_s c_{p,s} \Delta T_s \quad (2.13)$$

The solar heat transfer fluid can then be routed to each collector either in parallel or in series. Series flow assumes that, even if the collectors are in an array, the mass flow rate is constant throughout each loop and the fluid is routed in a serpentine manner. Parallel flow assumes that a uniform fraction of mass flow rate is divided among each loop and mixes at the end before entering the solar heat exchanger. For the case of a CSP array with N_l loops, Equation 2.12 can be altered such that

$$q_r = r_c \text{DNI} \eta_c \sum_{i=1}^{N_l} A_{r,i} \quad (2.14)$$

where $A_{r,i}$ is the receiver area for the i^{th} loop and η_c is the overall collection efficiency of the SCA. If each loop is assumed to be uniform (i.e. uniform length, mass flow), then Equation 2.14 can be further simplified and combined with Equation 2.13 (where $\dot{m}_l = \frac{\dot{m}_s}{N_l}$).

$$q_r = N_l r_c \text{DNI} \eta_c A_{r,l} = N_l \dot{m}_l c_{p,s} \Delta T_s \quad (2.15)$$

From Equation 2.15 it can be seen that ΔT_s will be less for parallel flow. To achieve the same $q_{\text{abs},f}$, the total mass flow rate must be larger than in series. The large ΔT_s that can be expected in a series configuration is not desirable if the process is operating close to the boiling point of the

heat transfer fluid. Large temperature gradients may also cause warping in receiver tubes that can result in the defocusing of the receiver and radiation leakage.

The equation for $A_{r,\text{tot}}$ can be determined using Equation 2.15 where the total receiver area is equal to the product of the number of collection loops and the receiver area for each loop ($A_{r,\text{tot}} = N_l A_{r,l}$).

$$A_r = \frac{q_s}{\varepsilon \eta_c r_c \text{DNI}} \quad (2.16)$$

In terms of the augment fraction ($k = \dot{Q}_s / \dot{Q}_{B,\text{nom}}$), the minimum receiver length required can be determined by combining Equations 2.9 and 2.16

$$L_{\min} = \frac{k \dot{Q}_{B,\text{nom}}}{\text{DNI } \varepsilon \eta_c r_c \pi d_r} \quad (2.17)$$

For an assumed SCA length of 30 m, the minimum number of required SCA to meet the specifications set by k is the ratio of L_{\min} to L_{SCA} rounded up to the nearest whole assembly.

In order to simulate the layout of the solar field, it will be assumed that the SCA are installed in a rectangular array with multiple loops of uniform length. Consistent with commercial CSP projects and a study published by Channiwala and Ekbote, it is assumed that each PTC loop is installed with a pitch of $p = 15$ m between each receiver tube or $p = 20$ m for LFR [56].

The length of each loop is maximized to avoid as much unused land as possible by initially assuming each loop of the solar field spans the maximum latitudinal length of the available land specified as an input to the model. The number of SCA in a loop (N_a) is equal to the ratio of the maximum field length to the length of a single assembly. For a rectangular array of SCA in an $N_a \times N_l$ configuration, N_a may not be a whole number factor of N_{SCA} , meaning consistent loop lengths is not feasible. To check the configuration, the remainder of N_{SCA} / N_a is calculated and compared to N_a . If the remainder is greater than half of N_a , then N_{SCA} is rounded up to complete that loop and $N_l = N_{\text{SCA,new}} / N_a$. Rounding up is a slight overestimate for this simulation and can be considered to partially offset the overestimate of A_r such that the resulting solar field configuration from this method will approach the field size required to supply the energy specified by k . If the remainder is less than half of N_a , then N_a is decremented and the above process is repeated until a uniform

array can be generated. The total estimated land area used (A_t) is approximated by the total length of a single loop ($L_r N_a$), W_p , and the loop pitch (p).

$$A_t = (L_r N_a)[W_p N_l + (p - W_p)(N_l - 1)] \quad (2.18)$$

The effect of maximum loop length ($L_{l,max}$) and k on the amount of receiver area and the size of the total solar field for both PTC and LFR is shown in Table 2.5. There does not appear to be a significant effect of $L_{l,max}$ on A_r . For most instances, increasing $L_{l,max}$ reduces A_{sf} , which is expected due to the potential reduction in total number of loops and unused land due to spacing needs. However, the changes in A_{sf} from $L_{l,max}$ are not significant, so the estimates of A_{sf} from this analysis are largely independent of the geometry of the land designated for the solar field.

2.3 Solar Integration Model

Solar Integration

Thermal energy collected by the solar field is assumed to be integrated into the coal power block by means of FWH bypass. The water bypasses the designated FWH and instead passes through a different heat exchanger in which the solar thermal energy is transferred to the water. Because the CSP energy is replacing the role of steam extracted from a turbine, that extraction mass flow is then assumed to continue through the cycle, increasing the total inlet enthalpy of the applicable turbine and all downstream hardware. Increasing the total enthalpy in turn increases the total power generated by each turbine. However, the simplified coal model used in this study assumes the FWH process is done by a single FWH at constant pressure. These changes in the power block thermodynamics require an update to the simplified model to allow for single FWH bypass and limits to total power generation.

The steam extraction pressure is calculated using the mass-averaged pressure approach assuming all flow rates are unchanged with the exception of the extraction line tied to the bypassed FWH and the main line. In the solar integration model, this is illustrated by placing the solar heat exchanger (SX) in series before the constant pressure FWH (Options A and C in Figure 2.6) with thermal input from the solar field to the SX if the FWH being bypassed is followed by another

Table 2.5: Effect of technology and maximum loop length ($L_{l,\max}$) on receiver area (A_r) and solar field size (A_{sf})

$L_{l,\max}$ [m]	k [%]	Technology	A_r [10^3 m^2]	A_{sf} [ac]
300	1	PTC	2.1	30.4
		LFR	1.1	21.1
	6	PTC	12.4	182.8
		LFR	6.5	127
	10	PTC	20.7	305.1
		LFR	10.8	211.4
500	1	PTC	2.1	30.2
		LFR	1.1	21.6
	6	PTC	12.4	182.2
		LFR	6.5	127.2
	10	PTC	20.8	305
		LFR	10.8	210.8
1000	1	PTC	2.2	29.8
		LFR	1.2	22.3
	6	PTC	12.4	181.2
		LFR	6.5	127.2
	10	PTC	20.8	303.9
		LFR	10.8	211.3

FWH in the real cycle. For FWHs not followed by another FWH (i.e. before the boiler or BFP, as in Options B and D in Figure 2.6), the SX was modeled after the combined FWH in the representative model. State 4 (Figure 2.6) represents the mixing done in the DA. While the DA may be thought of as an open FWH, only closed FWHs are considered as candidates for solar integration. However, the FWH numbering scheme common to coal power plant schematics is preserved in this study and FWH 4 is omitted from FWH bypass results discussed in Section 3.

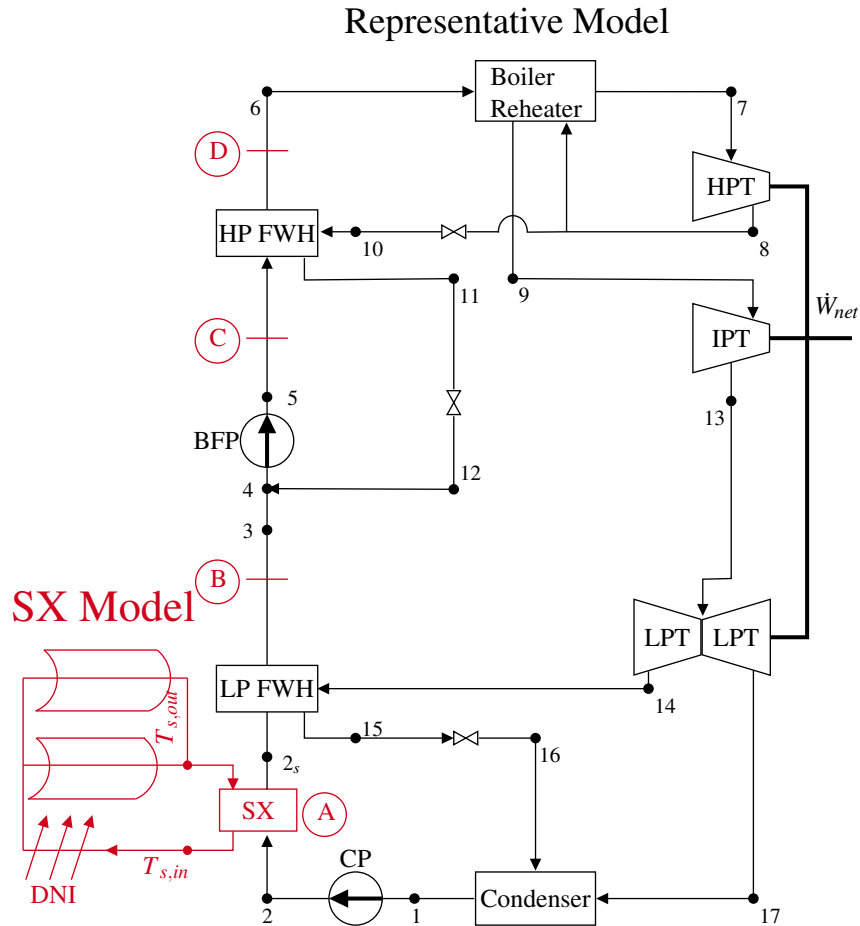


Figure 2.6: Sample solar integration model. Solar thermal energy is transferred from the solar field to the power block working fluid through a solar heat exchanger (SX) at one of the integration options A-D (Option A shown here in series before the low pressure feedwater heater (LP FWH)).

2.4 Solar Contribution

Hou et al. defined a method to calculate the solar work contribution, \dot{W}_s , that involved an exergy analysis on subsystems of the overall hybrid plant [57]. An adaptation of their approach for the solar integration model is presented here.

Subsystem boundary lines are selected based on the pressure level of the turbine stage included in the subsystem as shown in Figure 2.7a with extraction and exhaust pressures. However since steam is not extracted from the IP turbine, the boundary line corresponds with the pressure at state 13. Figure 2.7b illustrates the boundary lines for each subsystem when plotted on a T-s diagram and shows the highlighted area under the subsystems which is integrated to calculate \dot{W}_s . Each subsystem remains consistent across multiple solar integration configurations (Options A-D

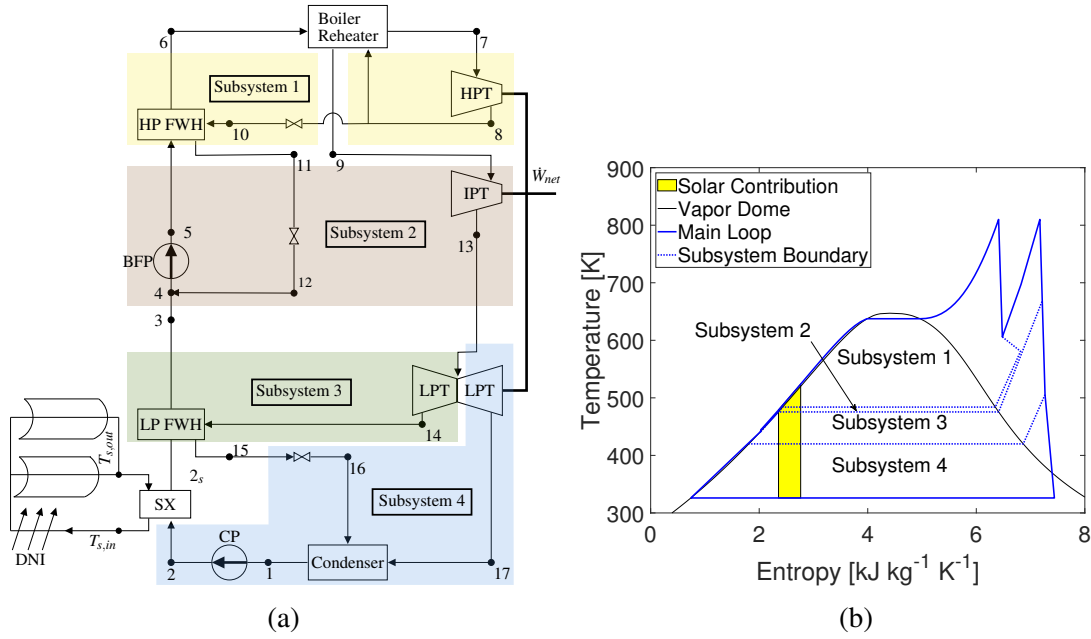


Figure 2.7: (a) Subsystem division for LP FWH1 or FWH 2 bypass and (b) T-s plot of \dot{W}_s for FWH 7 bypass at $k=1\%$

in Figure 2.1). The only modification is the inclusion of the SX model in different subsystems as the integration location changes. For example, Subsystem 4 always contains the lower stages of the LPT, the Condenser, CP, and drain cooler throttling after the LP FWH. For the lowest pressure solar integration (Figure 2.7a), the SX occurs before LP FWH and splits that boundary between subsystems 3 and 4. Similarly for options B-D, the subsystem boundaries are drawn to exclude the solar integration.

To test the model for \dot{W}_s calculation, the model was compared to the case study done by Hou et al. for a 600 MW hybrid plant with FWH 7 bypass, at $k=5.5\%$ [57]. The study by Hou et al. yielded a \dot{W}_s of 25.70 MW which results in a \dot{W}_s fraction of 4.28%. The model presented in this study for FWH 7 bypass at $k = 5.5\%$ yielded a \dot{W}_s of 21.7 MW from a calculated $\dot{W}_{net} = 494$ MW and \dot{W}_s fraction of 4.4%. Having computed comparable \dot{W}_s fractions from Hou et al. and the current study shows that the application of Hou et al.'s process is successful and that \dot{W}_s can be used in this study as a parameter to evaluate CSP hybrid performance.

2.5 Financial Model

This study uses an annual cash flow analysis, based on the methods used in the System Advisor Model (SAM) by NREL, to calculate the LCOE and payback time (PBT). The LCOE calculated from this study is treated as a solar marginal value that can be added to the LCOE of the parent coal plant to estimate the overall hybrid LCOE. The annual cash flow (C_{net}) is approximated (Equation 2.19) using annual costs (C_n) from operation and maintenance (O&M), financing, and taxes scaled by a nominal discount rate ($r_{d,\text{nom}}$). Input values used to approximate C_n are provided in Table 2.6.

$$C_{\text{net}} = \sum_{n=0}^N \frac{C_n}{(1 + r_{d,\text{nom}})^n} \quad (2.19)$$

Values selected for calculation of the Hunter plant are provided in Table 2.6. More details on the use of the values in Table 2.6 can be found in Appendix D.

The LCOE is calculated by dividing the annual costs by the annual \dot{W}_{net} , energy (E_n), and adjusting to a net present value (Equation 2.20), where r_r is the real discount rate.

$$\text{LCOE} = \frac{C_{\text{net}}}{\sum_{n=1}^N \frac{E_n}{(1+r_r)^n}} \quad (2.20)$$

O&M, tax costs, and loan payments are approximated using values shown in Table 2.6. Information on how to use the values in Table 2.6 is provided in Appendix D.

Two PBTs were calculated for this study. PBT1, used for the current analysis, assumes that the fuel savings resulting from operating a hybrid plant in fuel saving mode provide the benefit that offsets all accumulated costs inherent in the hybridization process. PBT2, discussed further in Appendix D, assumes that the fuel savings provide the benefit that offsets only the initial investment. The fuel savings are calculated using the fuel offset and the lower heating value of the coal (Equation 2.21). Annual fuel savings are subtracted from the annual costs until the savings are greater than or equal to the cumulative costs.

$$\text{FS} = \frac{E_{\text{sav}} F_F}{\text{LHV}_F} \quad (2.21)$$

Table 2.6: Selected input values used for the cash flow cost analysis

Parameter Name	Variable	Selected Input	Source
Capital Cost			
Site Improvements	F_{SI} [USD m ⁻²]	25	[58]
Solar Field	F_{SF} [USD m ⁻²]	170	[58]
Heat Transfer Fluid	F_{HTF} [USD m ⁻²]	60	[58]
Heat Exchanger	F_{HX} [MMUSD]	1.73	[59]
Contingency	r_{cont} [%]	7	[58]
Engineer-Procure-Construct	r_{EPC} [%]	11	[58]
Sales Tax Amount	$F_{t,sal}$ [% of CC]	80	[58]
Sales Tax Rate	$r_{t,sal}$ [%]	5	[58]
Annual Operating Expenses			
Fixed O&M	F_{FOM} [USD kW _e ⁻¹]	12	[60]
Variable O&M	F_{VOM} [USD MWh ⁻¹]	4	[61]
Property Tax Amount	$F_{t,prp}$ [% of CC]	80	[61]
Property Tax Rate	$r_{t,prp}$ [% of basis]	0.6	[62]
Insurance Rate	r_{ins} [% of CC]	0.5	[61]
Annual Loan Payment			
Loan Amount	F_L [% of CC]	50	[63]
Total Loan Period	P [years]	25	[61]
Loan Interest Rate	r_{int} [% of remaining balance]	5	[61]
Annual Tax Credits and Incentives			
Federal ITC Rate	$r_{ITC, fed}$ [% of CC]	10*	[64]
State ITC Rate	$r_{ITC, st}$ [% of CC]	0	[61]
Annual State and Federal Income Tax			
Depreciation Schedule	SC_{dep} [% of CC]	MACRS**	[61]
Federal Tax Rate	$r_{t, Fed}$ [%]	21	[61]
State Tax Rate	$r_{t, st}$ [%]	5	[62]

* r_{ITC} was set in 2019 to depreciate from 30% to 10% by 2022 [64].

**The modified accelerated cost recovery system (MACRS) is the name given to the federal depreciation schedule and has a separate value for the first five years of the project as shown in the following vector (20, 32, 19.2, 11.52, 11.52, 5.76).

The development of this financial model closely reflects the calculations performed within SAM by NREL; comparative tests during development showed agreement between the models to the order of rounding error. Savings obtained from fuel offset is a departure from the scope of SAM. The effect of augmentation and integration site on LCOE and PBT1 are explored further in Section 3.2.

Carbon tax is an incentive that has been introduced in certain countries and areas of the US to boost renewable energy projects over fossil fuel projects by penalizing the emission of greenhouse gases [65]. Though not widely implemented in the US, hypothetical values for a carbon tax are publicly available [66]. In this work, the effect of the carbon tax income is calculated from \dot{Q}_{fo} and the useful solar operating conditions. Results from the implementation of a solar premium and carbon tax are provided in Section 3.2.

Another option for improving financial feasibility is the consideration of a premium rate applied to the electricity consumer. A study by O'Shaughnessy et al. states that the average green energy premium paid by residential electricity consumers in 2016 was 0.018 USD kWh⁻¹ [67]. In this study, the income from increasing the electricity price for the consumer and the carbon tax are benefits that are treated similarly to income in the calculation. For each year, the premium benefit is calculated from the premium rate and the total energy provided by the power plant during average operating conditions. Alternatively, the green premium can charge the consumer based on the solar contribution to the power generation. Since the \dot{W}_s reported in Table 3.1 are up to 25 MW for higher k , the effect of the green premium price decreases but the consumer would only be paying for the electricity attributed to the renewable resource.

2.6 Optimization

The following models presented to this point comprise the hybrid model:

- SI model (Section 2.3)
- Solar contribution (Appendix A)
- Solar field configuration (Section 2.2.4)
- Financial model (Section 2.5)

The hybrid model has been designed such that the only inputs, or design variables, required to calculate hybrid performance are technology type (PTC or LFR), the number of the bypassed

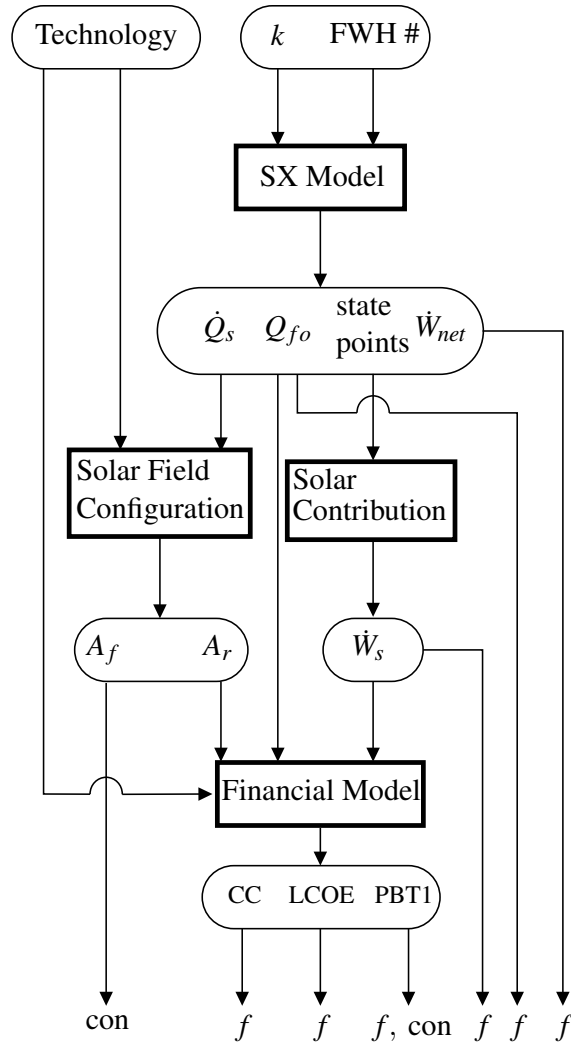


Figure 2.8: Overview of the interchange of parameters within the hybrid model. Bold rectangles indicate computational models with arrows connecting the necessary inputs and the reported outputs. Input and output variables are contained within rounded rectangles.

FWH, and k . All other model outputs or required inputs are calculated within the hybrid model and are passed between the internal functions as necessary.

The list above is also the order in which the models must be executed. The flow of parameters within the hybrid model is illustrated in Figure 2.8. Each model shown in Figure 2.8 requires inputs that are either calculated in a model higher in the chart or specified as part of the optimization searching algorithm. The hybrid model has been designed such that the only inputs, or design variables, required to calculate hybrid performance are technology type (PTC or LFR), the number of the bypassed FWH, and k . All other variables shown in Figure 2.8 are calculated

within models as specified by arrows leaving the square boxes. The variables used at the end of the hybrid model simulation are sorted in Figure 2.8 by their use in the objective function (f) or application to a constraint (con). All possible combinations of the design variables that fit within the constraints specified below are referred to as the *design space*. The selected searching algorithm will explore the design space by iterate through different combinations of the design variables to find the optimal design.

Searching Algorithm

Instead of looking at the hybrid plant as a problem with 2 discrete variables (FWH number and Technology) and 1 continuous variable (k), the problem can be expanded to be a series of continuous problems resulting in an optimization searching method referred to as an *exhaustive search*.

To implement the exhaustive search, all possible combinations of the discrete variables are treated as individual designs and processed as continuous problems. For the hybrid model, this means that for i possible CSP technologies and j possible integration sites, there will be $i \times j$ continuous optimization problems processed to determine the overall optimum for all possible technology/FWH/ k combinations. This exhaustive search is laid out in Figure 2.9 where each circle is a design variable and each line is a possible value of that variable. Only FWH bypass is considered for this study, so j is equal to the number of closed FWHs. Two feasible CSP technologies are considered: PTC and LFR. Thus, $i = 2$ and $j = 6$ because FWH 4 is an open FWH/deaerator (Section 2.3), and the total number of combinations analyzed is $i \times j = 12$.

Objective

The various optimization objectives that have been analyzed in other studies capture important parameters but do not necessarily consider all the factors that impact the overall quality of a design [68–75]. The following parameters have been identified as candidates for the optimization objective.

- Solar work contribution (\dot{W}_s) [MW]
- Fuel offset (\dot{Q}_{fo}) [MW]

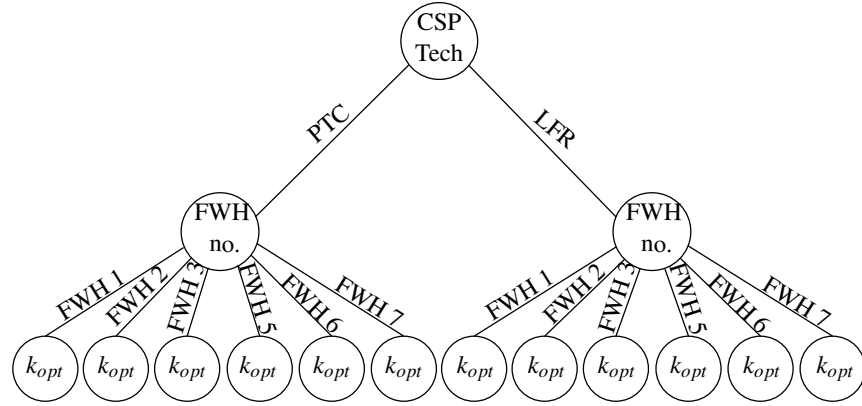


Figure 2.9: Visualization of the exhaustive search implemented in determining the optimal k (k_{opt}) for each technology/FWH combination.

- Levelized cost of electricity (LCOE) [USD kWh⁻¹]
- Payback time 1 (PBT1) [yrs]
- Fuel earnings (FE) [USD]

When multiple variables are used in an objective, the units should be consistent and each combination of parameters should conflict with the others. Conflicting objectives provide a way to limit the search. For example, if maximizing \dot{W}_s is used as the only objective, the expected outcome would be to increase the augment fraction as high as possible until a constraint is violated. However, when opposed by financial parameters such as minimizing LCOE, the optimization will have to find some intermediate k that has the largest \dot{W}_s and the lowest LCOE.

The MATLAB function ‘`fmincon`’, included within the MATLAB optimization package, has been selected to perform the continuous search for this study. Because ‘`fmincon`’ searches for the minimum value of the specified objective, care must be given to combine the variables above such that the ideal value will be a minimum. For best performance, multiple objectives should also have consistent units and be of comparable orders of magnitude.

If the sub-objectives are of different orders of magnitude, one objective will dominate the convergence criteria specified for the optimization termination. For example, if one sub-objective has an initial value of 100 and a second sub-objective is 1, the total objective could be 101. The next iteration in the optimization search may not result in any change in sub-objective 1, but a 100% increase in sub-objective 2. The total objective value would then be 102 with less than 1%

change. Thus, sub-objectives may require an additional constant multiple to achieve consistent orders of magnitude.

Objective parameters are separated in two categories based on impact of plant thermodynamics or economics. The total objective (f) can then be expressed in terms of the objective parameters (Equation 2.22) where \dot{W}_s and \dot{Q}_{fo} are scaled by the net work output by the plant (\dot{W}_{net}). The financial parameters are combined to achieve dimensional homogeneity. To penalize $\dot{Q}_{fo} < 0$, the optimization is set up such that each sub-objective would drive toward a maximum. Multiplying by -1 effectively turns the maximization problem into a minimization problem, satisfying ‘fmincon’ minimum search preference. Each sub-objective will have units kW USD⁻¹.

$$f \propto -\frac{\dot{Q}_{fo} \dot{W}_s}{CC \dot{W}_{net}} - \frac{1}{LCOE (365 \text{ PBT1 } h_{sun})} \quad (2.22)$$

Further control of sub-objective impact is achieved by applying weights (ω) to each sub-objective. The weight for each sub-objective is determined by the developer, but the sum of all weights should equal 1 ($\omega_1 + \omega_2 + \dots + \omega_N = 1$). As an example, for plants that have strict environmental goals, increasing \dot{Q}_{fo} may be more important than financial outcomes, so this process can be implemented with $\omega_1 > \omega_2$. Conversely, if financial performance is most important, $\omega_2 > \omega_1$ will provide the desired optimum.

$$f = -\omega_1 \frac{\dot{Q}_{fo} \dot{W}_s}{CC \dot{W}_{net}} 10^7 - \omega_2 \frac{1}{LCOE (365 \text{ PBT1 } h_{sun})} 10^2 \quad (2.23)$$

Additional constants are multiplied with the objectives as necessary to reach comparable orders of magnitude and dimensional homogeneity, such as converting PBT1 from years to hours by multiplying 365 days/year and h_{sun} .¹ For best optimization results, the starting point given to ‘fmincon’ should be within the feasible design space.

The range of financially feasible designs can be approximated by analyzing the behavior of \dot{Q}_{fo} with respect to k , as shown in Figure 2.10. All bypass options are negative for low k . Each option seems to approach 0 at k_{FWH} , or the k equivalent to the heating load of the bypassed FWH at nominal operating conditions. Analyzing the state points of the solar integration model for each of the LP integration options shows that the water boils at $k > 3\%$. Considering $k_{FWH} \approx 2 - 3\%$ for

¹11.9 hr day⁻¹ in Castle Dale

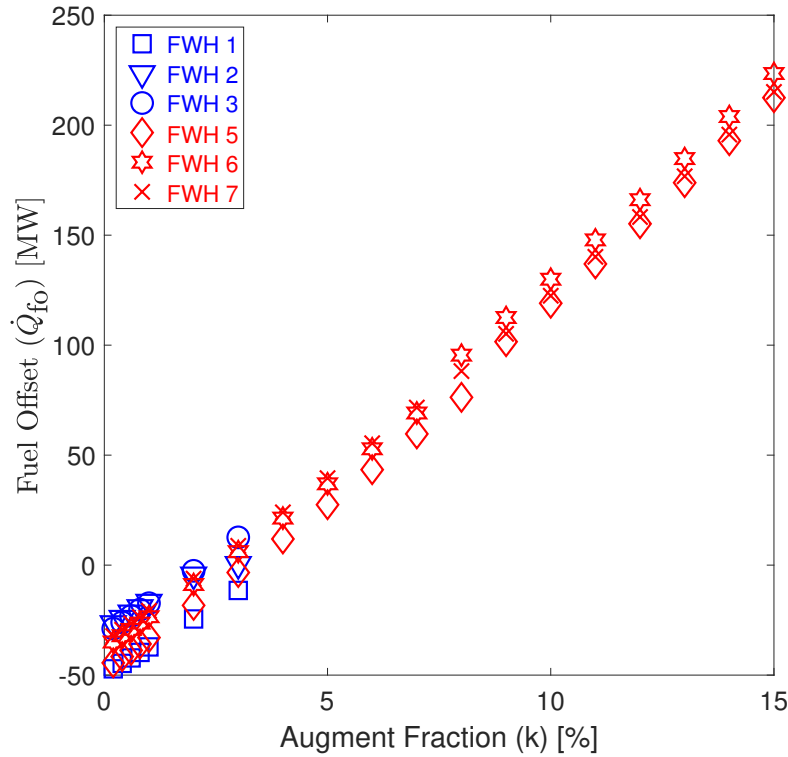


Figure 2.10: Behavior of \dot{Q}_{fo} . FWH 1 and FWH 2 bypass does not show a decrease in fuel consumption. Other bypass options only reduce fuel consumption once $k > k_{FWH}$.

all LP integration options, no LP option is considered feasible for complete FWH bypass. Once $k > k_{FWH}$, the CSP field is starting to contribute more thermal energy and \dot{Q}_{fo} increases. One option to expand the region of feasible designs based on \dot{Q}_{fo} is partial FWH bypass as opposed to complete FWH bypass, the focus of this current work. Partial FWH bypass is discussed further in Chapter 5.

Constraints

Additional constraints were placed within the individual models used in the optimization to ensure the outputs were feasible, such as confirming the components within the hybrid model simulation met requirements for the conservation of energy. However, additional constraints are required to ensure the designs generated in the optimization search are feasible for the desired application.

Two additional constraints have been applied restricting the size of the solar field and the duration of PBT1. The optimization constrained the designs to limit the size of the solar field area below a maximum size specified by the user. For this analysis, it is assumed there is an area of 20 ac (81,000 m²) available for a solar field.² A second constraint specifies that the PBT1 be less than the expected project lifetime specified by the user. A project life of 30 years is assumed for this study.

²For Hunter, an area of approximately 45000 m² (12 ac) has been identified as a candidate for CSP installation.

CHAPTER 3. RESULTS

The results presented here are for the models described in Chapter 2. Unless otherwise specified, the specific values reported and conclusions drawn are based on data for the Hunter Unit 3 coal power plant in Castle Dale, UT.

3.1 Solar Contribution

The methods used to calculate \dot{W}_s were tested for several k at each integration site. The energy transferred in each FWH accounts for approximately 3% of the overall heating power done in a coal power plant. Thus, $k = 3\%$ CSP effectively replaces each FWH while providing the same amount of thermal power as the bypassed FWH would and $k = 1\%$ and 6% are used as lower and upper bounds, respectively. As expected, Table 3.1 shows that increasing k and increasing the pressure stage of FWH bypass generally increases \dot{W}_s . Of note is the relative effect of k on \dot{W}_s as compared to integration site. While \dot{W}_s depends on the amount of steam typically extracted from the bypassed FWH, the increase from changing integration site is small as compared to the increase in \dot{W}_s with increasing k . The choice between k and integration site allows for flexibility in design and operation decisions. Determining the size of a solar field is a decision that must be made in the design stage of a project, but the results in Table 3.1 suggest that the choice of integration site is much more flexible in that changing the integration from bypassing one FWH to another FWH at a similar pressure stage should not significantly affect the performance of the hybrid plant.

Table 3.1: Results for solar contribution based on FWH number and the solar augment fraction (k). Compare with results for $k = 0\%$ in Table 2.1.

LP FWH #	k [%]	\dot{W}_s [MW]	\dot{Q}_B [MW]	η_{th} [%]	η_{II} [%]	HP FWH #	k [%]	\dot{W}_s [MW]	\dot{Q}_B [MW]	η_{th} [%]	η_{II} [%]
1	1	1.24	1313	38.6	43.9	5	1	3.23	1309	38.7	44.0
	3	4.53	1287	38.5	43.8		3	10.35	1279	38.7	44.0
	6	11.42	1276	37.7	42.8		6	21.97	1233	38.9	44.1
2	1	1.24	1293	39	44.5	6	1	3.23	1299	38.8	44.2
	3	4.53	1276	38.8	44.1		3	10.38	1270	38.9	44.3
	6	11.40	1276	37.6	42.6		6	22.12	1223	39.1	44.3
3	1	2.74	1293	39.1	44.6	7	1	3.48	1297	37.7	43.0
	3	8.88	1263	39.2	44.6		3	110.4	1267	37.8	43.0
	6	18.24	1213	39.2	44.5		6	24.02	1221	37.9	43.0

For the HP configurations that have been shown to be feasible, both η_{th} and η_{II} increase slightly. This behavior was predicted in Section 2.1, though both η_{th} and η_{II} are lower than the nominal values reported in Table 2.1.

3.2 Financial

A sample of financial results is provided in Figures 3.1 and 3.2. Of note in Figure 3.1 is the LCOE order of magnitude. The LCOE reported here is a marginal value representing the ratio of the costs associated only with the integration of CSP to the total hybrid plant energy output. This marginal value can then be added to the LCOE of the coal plant to approximate the overall hybrid LCOE. Figure 3.1 shows that the LCOE depends mainly on k and does not vary considerably for different locations of solar integration in the plant. The general trend for integration options is that the LCOE is less for LP integration.

The fuel offset power (\dot{Q}_{fo}) is the parameter that has the largest effect on PBT1. The variation in PBT1 with k is shown in Figure 3.2 for HP integration options and 0 USD sh.tn.⁻¹ carbon tax. As was shown in Section 2.6, \dot{Q}_{fo} was negative for FWH 1 and FWH 2 but became positive for all other FWHs once k passed the k_{FWH} . Until $k > k_{FWH}$, there is no benefit for PBT1. However, the costs of the plant continue to increase with k so integration options only become feasible when \dot{Q}_{fo} gets sufficiently large. The \dot{Q}_{fo} for HP integration configurations does not vary

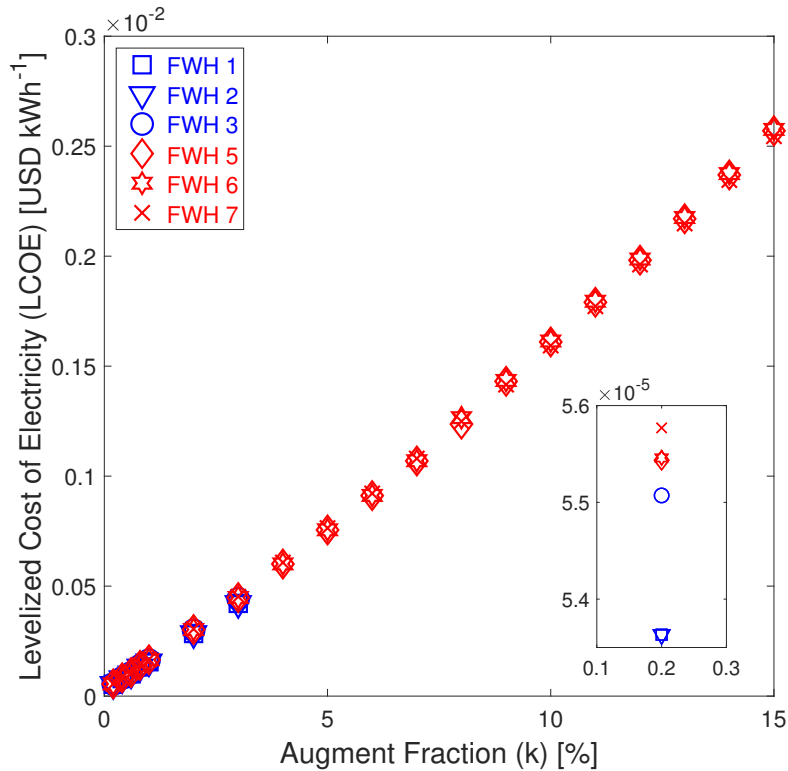


Figure 3.1: Variation in LCOE with augment fraction, k . The LCOE for each FWH generally increases in the order $1 \approx 2 < 3 < 5 \approx 6 < 7$ as shown in the insert.

greatly between each FWH, resulting in nearly identical PBT1 results for each HP configuration (Figure 3.2).

Figure 3.3 shows the effect of carbon tax on the LCOE (Figure 3.3a) and on PBT1 (Figure 3.3b) for FWH 3 and FWH 7 bypass.

Values for the carbon tax used to generate Figures 3.3a and 3.3b are moderate (16 USD sh.tn.⁻¹; similar to California Emission Trading System), aggressive (30 USD sh.tn.⁻¹; similar to Iceland carbon tax) and very aggressive (50 USD sh.tn.⁻¹; France carbon tax) [65, 66]. Even for a moderate carbon tax (16 USD sh.tn.⁻¹), significant changes in both LCOE and PBT1 are seen in Figure 3.3. This sensitivity to carbon tax suggests that hybridization is more likely to have a wider range of feasible designs for locations with carbon taxes in place. Having an LCOE less than 0 (as in Figure 3.3a) occurs when the financial benefit exceeds the cumulative costs. After the initial investment, the annual net costs must be negative (net financial gain) in order for the project to make money. For projects without carbon tax, the initial investment and annual loan payments are

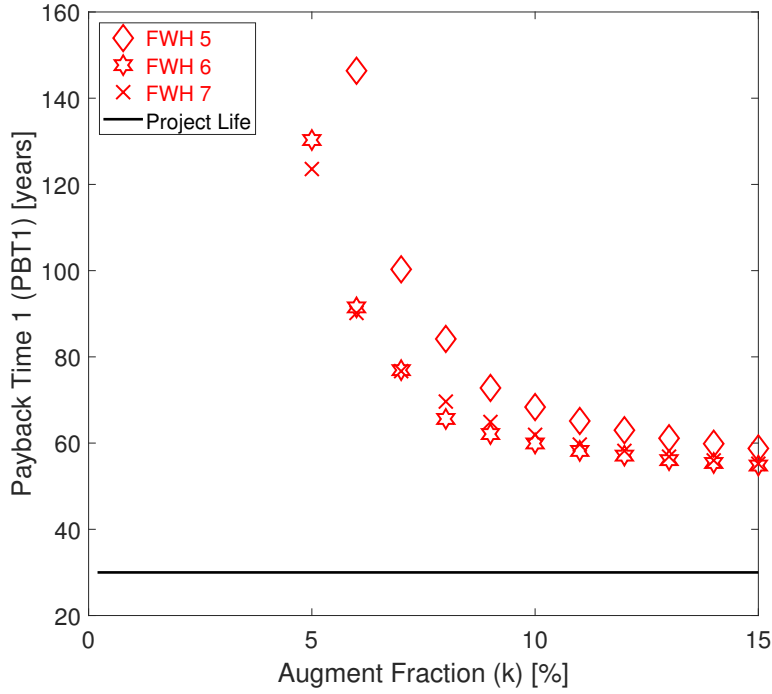


Figure 3.2: Calculated PBT1 for solar integration at HP FWHs with 0 USD sh.tn.⁻¹ carbon tax. The horizontal line at PBT1=30 years signifies the typical life of coal power plant.

large enough that the summation of each negative LCOE does not make up the difference. With a carbon tax in place, the negative LCOE for each year in the cash flow analysis will increase in magnitude with increasing carbon tax to the point that the summation of negative LCOE for each year surpasses the cumulative LCOE from the initial investment and annual loan payments. In this study, negative LCOE typically corresponds with an aggressive carbon tax or large \dot{Q}_{fo} .

Applying a green energy premium value of 0.018 USD kWh⁻¹, as reported in O'Shaughnessy et al. [67], reduces PBT for PTC bypass of FWH 6 at $k = 9\%$ with a 0 USD sh.tn.⁻¹ from 62.1 to 3.9 years (94% reduction), resulting in a feasible condition for that k/technology/FWH configuration. As is shown in Figure 3.4, the PBT with the premium based on \dot{W}_s still decreases but at a lower rate than the PBT with the premium based only on \dot{W}_{net} . For FWH 6 at $k = 9\%$, no carbon tax, and the average green energy premium value of 0.018 USD kWh⁻¹, the PBT comparison from Figure 3.4 is 3.9 years when based on \dot{W}_{net} and 22.5 years when based on \dot{W}_s .

Consumer electricity rates are highly dependent on location, so the sensitivity of feasibility to green premium price can be seen in Figure 3.4 for PTC bypass of FWH 6 at $k = 6, 9,$ and 10%

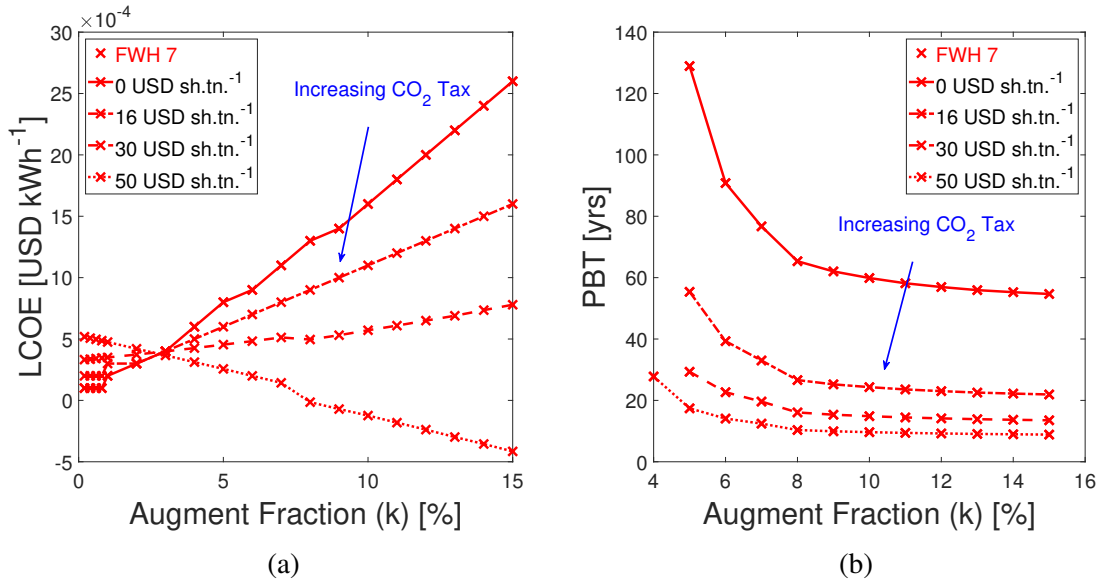


Figure 3.3: Effect of carbon tax on (a) LCOE and (b) PBT1. FW H 6 is used as an example of HP integration. LCOE and PBT1 trends for other bypass options are similar to those shown in Figures 3.1 and 3.2.

with a 0 USD sh.tn.⁻¹ carbon tax. The main conclusion from Figure 3.4 is that applying a premium considerably decreases PBT with all else constant. However, there is a limit at which increasing the premium price no longer shows significant decreases in PBT. For Figure 3.4, the change in PBT is less than 2% when it is increased beyond 0.0155 USD kWh⁻¹. The premium of 0.0155 USD kWh⁻¹ is sufficient to reduce PBT to 4.3 years for $k = 9\%$.

Looking at the effect of a carbon tax (Figure 3.3b) and a green premium electricity price (Figure 3.4) show similar trends in the effect on PBT from carbon tax and green premium. Increasing a carbon tax or green premium will decrease the PBT, but adjusting the green premium has a greater impact than increasing the carbon tax. This is due to how each value is implemented in this study, as discussed in Section ???. A carbon tax is applied to the coal saved by solar augmentation, typically as high as 100 MW for low-solar augmentation. The green premium, however, is applied to all the electricity generated during h_{sun} throughout the year. For the Hunter Unit 3 plant with a nameplate generation of almost 500 MW_e, the green premium is effectively applied to a greater source of power.

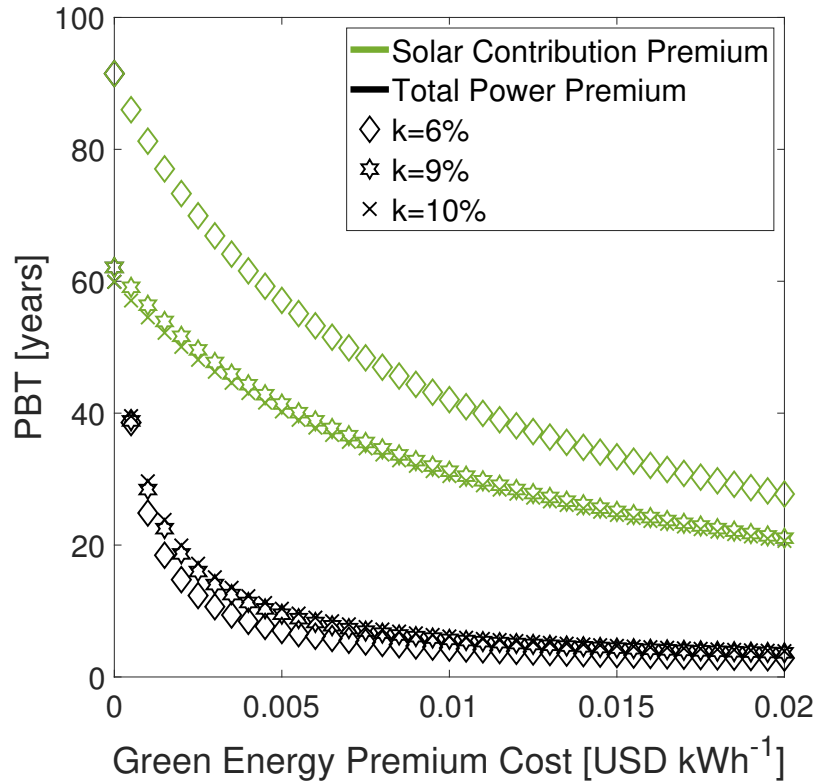


Figure 3.4: Effect of green premium price and k on PBT1.

3.3 Optimization

As described in Section 2.6, hybrid performance is divided in thermodynamic and economic categories. Figure 3.5 shows the relationship between the two objectives for weights in increments of $\omega = 0.2$ (i.e. $\omega_1 = [0, 0.2, 0.4, \dots, 1]$, and $\omega_2 = [1, 0.8, 0.6, \dots, 0]$) for HP FWHs and 16 USD sh.tn.⁻¹ carbon tax. The curves represented by the trendlines fit to the calculated optimums are Pareto fronts. The Pareto front for two-objective optimization is a curve that represents the hypothetical boundary for feasible designs. In the case of this study, the optimization objective was written such that the optimal design would trend towards the minimum of each objective. In Figure 3.5, the Pareto fronts suggest that the majority of other feasible designs result in a higher value for at least one of the two objectives.

As expected, the trendline reflects an inverse relationship and the objectives contradict each other. The trendline fit to the sample simulations demonstrates the expected pareto front of feasible designs for different possible ω combinations. The results in Figure 3.5 result in the majority of

the ω combinations lying closer toward a thermodynamic minimum, suggesting that OBJ1 may be dominating the optimization. In general, the trendline representing the Pareto front for FWH 6 bypass lies below all other designs, suggesting FWH 6 bypass is most likely to be the optimal integration site for a hybrid plant when compared to results for each of the other FWHs.

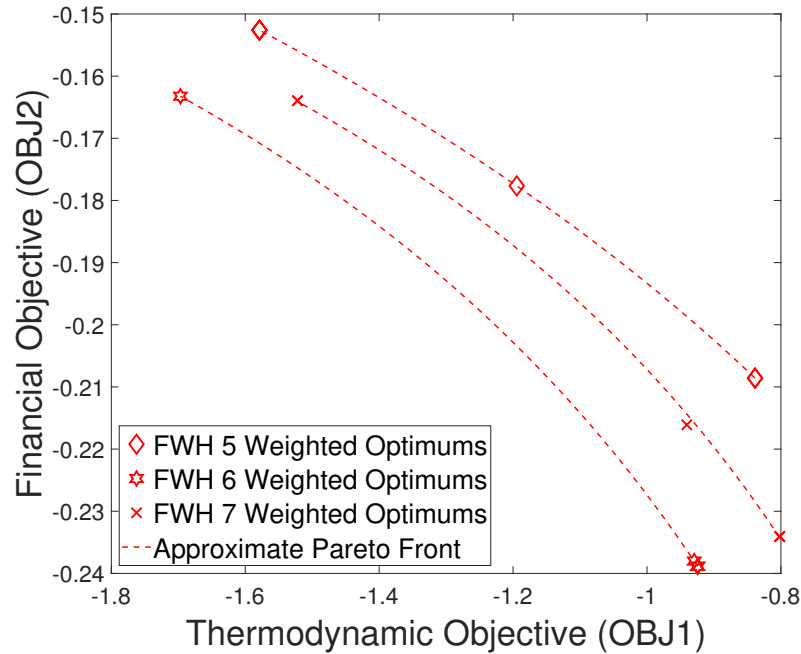


Figure 3.5: Pareto fronts for HP FWH bypass displaying the competing optimization objectives for the current study and 16 USD sh.tn.⁻¹ carbon tax. A minimum in OBJ1 corresponds to a maximum in OBJ2 and vice-versa for each FWH option.

Results from Section 3.2 show that k , directly tied to the capital cost, has the largest impact on financial performance and overall feasibility of a hybrid project once $\dot{Q}_{f0} > 0$ (Figure 3.1). Thus, more weight is given to the financial objective, or $\omega_1 = 0.2$, $\omega_2 = 0.8$. Optimization results for each FWH and Technology type are given in Table 3.2 assuming a project life of 30 years and a maximum allowable solar field of 30 ac. As shown in Figure 2.9, k_{opt} is found for each FWH bypass option combined with either PTC or LFR for the solar field.

The optimization results in Table 3.2 show the k_{opt} for each technology/FWH combination. The overall hybrid optimal design is found by selecting the configuration resulting in the lowest (most negative) value for f (Section 2.6). For this study, $k = 9\%$ PTC bypassing FWH 6 is the

Table 3.2: Optimums at for each FWH bypass option for $\omega_1 = 0.2$, $\omega_2 = 0.8$, and 16 USD sh.tn.⁻¹ carbon tax. f is a minimizing function, so the smallest value (or most negative) is considered the best.

	FWH #	k_{opt} [%]	\dot{Q}_{fo} [MW]	A_{sf} [ac]	LCOE [10 ⁻⁴ USD kWh ⁻¹]	PBT1 [years]	f [kW USD ⁻¹]
PTC	5	14.5	202.7	517.9	16	23.7	-0.79
	6	9	112.6	301.4	9.5	25.2	-0.92
	7	9	105.1	301.4	9.6	27.1	-0.84
LFR	5	14.8	208.5	366.5	24	> 30	-0.46
	6	13.2	188.6	320.9	21	> 30	-0.48
	7	14.7	209.2	364.2	23	> 30	-0.46

optimal configuration for 16 USD sh.tn.⁻¹ carbon tax. This result is consistent with similar work published in archival literature suggesting hybrid performance improves as the integration site approaches the boiler stage [40, 76]. It was expected that LFR integration would be generally less feasible than PTC due to higher capital costs. This is evident in that none of the optimal designs for LFR had feasible PBT1. However, the efficiency of LFR land use is apparent throughout Table 3.2, but particularly for FWH 5 bypass where the estimated solar field for the LFR configuration is similar to the PTC configuration despite a higher k_{opt} than PTC FWH 5 bypass [77].

3.4 Geography

Changing the geographic location of hybridization also has a significant effect on financial parameters. DNI is highly dependent upon geography, which has a strong impact on the size of the solar field required (Equation 2.16). Changing location also may change state or federal tax information. As an example of the effect geography has on the optimization results, Table 3.3 shows the optimal configurations for a plant with parameters consistent with Hunter Unit 3 operating in a city with lower DNI (Cleveland, OH) and a city with higher DNI (El Paso, TX) for FWH 7 bypass and an aggressive carbon tax (50 USD sh.tn.⁻¹).

In comparing the optimization fitness, the minimal f is expected to be in El Paso, TX, depending on the specific operating procedure of a power plant in that area. This confirms the high

Table 3.3: Effect of geography on hybrid performance. Castle Dale, UT is the benchmark with Cleveland, OH and El Paso, TX as examples of lower and upper DNI, respectively. Local tax and financing parameters are not included.

Location	DNI [W m ⁻²]	k_{opt} [%]	A_{sf} [ac]	LCOE [10 ⁻⁴ USD kWh ⁻¹]	PBT1 [yrs]	f [kW USD ⁻¹]
Cleveland, OH	326	14.7	875	30	> 30	-0.35
Castle Dale, UT	542	9	301.4	9.5	25.2	-0.92
El Paso, TX	624	9	263.4	8.0	21.5	-1.26

dependence CSP technology has on installation geography. A proposed hybrid project is most likely to be feasible if the location of interest has high DNI.

CHAPTER 4. CONCLUSION

The data presented shows that the integration site in the power plant causes the greatest effect on plant performance; k and CSP technology type have the greatest impact on financial performance. Hybridization has an impact beyond just plant efficiency and LCOE.

The US Energy Information Administration reports that the amount of CO₂ emissions from a coal power plant can be estimated by the conversion factor 205 lb. CO₂ MMBTU⁻¹ for bituminous coal [12]. With FWH 6 bypass as an example, Table 3.2 shows that 52 MW worth of coal is offset during hybrid mode. Using the effective solar time to convert from MW to MMBTU and projecting throughout the year, the conversion from the Energy Information Administration results in a CO₂ emissions reduction of approximately 171 tons per year. According to Bernal et al. [78], a typical temperate, dry conifer forest (the most prominent forest in UT) removes approximately 6.4 t CO₂ ha⁻¹ year⁻¹. Thus, CSP augmentation in UT reduces emissions equivalent to approximately 27,000 ha of dry conifer forest for $k = 9\%$ PTC augmentation at FWH 6 bypass.

This study analyzes a retrofit hybrid model operating in fuel saving mode, but Manente showed that plants constructed with hybrid capabilities, typically operating in power boost mode, can also see considerable benefits [23]. Manente's study, focused on integrated solar combined cycles, shows that the inclusion of solar in the power generation process can add 50 MW_e to an existing plant without changing any equipment. Included in Manente's study was the requirement to upgrade the turbine to account for the potential increase in capacity. This suggests that a power boost analysis is best for initial construction and plants anticipating upgrades to turbines or electrical transformers due to the added capital cost of higher capacity components whereas fuel saving mode is best for retrofit projects.

The impact of hybridization can be extended with the addition of thermal energy storage (TES). Storage technology has been studied for use in building energy efficiency [79] as well as CSP. Common options for storage materials include phase change materials [80, 81], large col-

lections of rock [82], and molten salts [83]. Studies show that TES can add considerably to the hybridization benefit [84–87]. The inclusion of TES would cause changes in the financial performance of a hybrid plant necessitating edits to the model presented in the current study. The operation of the plant would largely be the same with the exception that the hybrid plant would be able to operate in fuel saving mode for a longer period of time. This increase in effective solar time is expected to increase the total amount of coal saved over time and cause a potential decrease in LCOE and PBT1 depending on the selection of TES technology.

While benefits of hybrid technology have been explored in published literature, this study has contributed a simplified method to evaluate preliminary hybridization feasibility based on a representative coal power plant. The representative model was shown to be applicable to Hunter Unit 3 in Castle Dale, UT and a separate coal power plant with a different configuration [28]. Using solar data from NREL and standard equipment dimensions, the solar resource for the hybrid geography was quantified and combined with the representative model in the solar integration model. The fraction of power out of the hybrid power plant that can be attributed to the solar integration was calculated using an exergy analysis. A financial model was used to calculate comparative parameters including LCOE, PBT1, and fuel earnings. The performance of the solar heat exchange model is combined with the financial performance to define the optimization objective used to find the optimal configuration for a proposed hybrid retrofit project. Results from simulating CSP integration into Hunter Unit 3 suggest that hybridization may be feasible considering the expected thermodynamic benefits to the power plant and the LCOE and PBT1 for small k . LFR requires less land for a solar field than PTC, but higher capital costs universally preclude the use of LFR in hybrid projects according to the assumptions of this analysis. As expected, areas with higher average DNI are more promising candidates for \dot{W}_s and areas with lower DNI are less feasible. It is shown that for a possible scenario including a carbon tax, the LCOE and PBT1 will decrease accordingly and increase the feasibility of hybridization. The impact of a green premium on consumer electricity prices is also demonstrated to have a dramatic effect on decreasing PBT1. Carbon taxes and green premium prices are common in communities across the world [65,67], so a combination of both incentives makes CSP-coal hybridization feasible and competitive with other power generation options. The method presented in this paper, while simplified, is largely irrespective of any particular coal plant, geography, or local tax code. The results suggest a generous range of

feasible hybrid configurations, but do not provide an explicit commentary on public policy. While the effects of carbon tax on feasibility as defined in this analysis are substantial, there are many and various effects of carbon tax on an economy and social structure such that this study alone cannot be used to argue for or against the implementation of a carbon tax or other applicable policies. Instead, it is only suggested that hybridization be considered where such policies may be in place.

CHAPTER 5. FUTURE WORK

5.1 Partial FWH Bypass

One option to expand the range of feasible designs is to develop a model for partial FWH bypass. As discussed in Section 2.6, the CSP field must be able to provide at least as much energy as the bypassed FWH does during nominal operating conditions in order to see any reduction in fuel consumption. This is because this study only considered complete FWH bypass. It is likely that considering partial FWH bypass would increase the range of feasible designs. However, that would require another set of operating correlations for each property associated with each FWH (i.e. extraction pressure, extraction temperature, etc.).

5.2 Minimum Spacing

The pitch for the PTC array discussed in Section 2.2.4 is based on common practice and a study by Channiwala and Ekbote [56]. Padilla discusses at length the effect of row spacing on shading [88]. Equations are provided relating to the collector geometry and position of the sun. It follows that these equations can be used in a continuous optimization problem to determine the optimal spacing and SCA azimuth angle to reduce shading. Due to the tilt of the Earth with respect to the sun, the path the sun takes during a day changes throughout the year and will affect the amount of shading experienced in the solar field. An objective for this optimization problem should have a built-in preference toward optimal spacing and γ_s for days of typically high solar resource availability. While the DNI varied greatly with location in Section 3.4, the CSDNI for each location is much similar. Castle Dale, UT and El Paso, TX have comparable CSDNI at 756 and 759 W m^{-2} , respectively, and Cleveland, OH is lower at 615 W m^{-2} . However, Cleveland experiences more weather that impedes with solar collection which reduces the multi-year average DNI. If the spacing for a plant is optimized for operation during clear periods, the solar field will

perform as needed during peak collection with less curtailment and shading effects will not be as significant during off-peak weather periods as solar availability is in general lower. Incorporating shading and optimal spacing into this study may limit some hybrid designs that would theoretically require more than 15 m and improve other designs that require less than 15 m.

5.3 Retrofit vs. Initial Construction

The analysis provided in this study focused on steady-state operation of an existing coal power plant retrofitted with CSP integration. The methods provided in Chapter 2 will vary significantly when considered for a plant initially designed and constructed as a CSP hybrid power plant. The solar integration (Section 2.3) is still relevant for FWH bypass configurations, but has not been equipped for other integration options. As discussed in Chapter 1, a study from EPRI found the optimal CSP integration options for coal power plants was at high temperatures and pressures, conditions only feasibly met by solar tower technology [16]. Increasing the frequency of initial construction CSP hybrid power plants may increase the installation of solar tower technologies and improve solar tower technology feasibility for other applications in the future.

The financial model to calculate solar marginal LCOE and PBT1, as defined in Section 2.5, relies on coal offset to provide the financial benefit. For an initial construction CSP hybrid power plant, the marginal LCOE model would need to be redefined to identify a different solar benefit or to abandon solar marginal LCOE and report an overall hybrid LCOE and PBT.

5.4 Natural Gas Hybrids

Table 1.1 lists the planned and operational hybrids throughout the world; all but one use PTC to offset natural gas. EPRI showed that the optimal configuration was using CSP for direct steam generation at the HP superheater outlet [16]. The integration options identified by EPRI for natural gas integration had comparable solar use efficiencies to those integration options for coal (FWH bypass was dismissed by EPRI with <30% solar use efficiency). The integration of CSP with a natural gas combined cycle, or integrated solar combined cycle, has been widely studied in archival literature [60, 89, 90]. Alqahtani and Patiño-Echeverri showed that for several locations,

ISCC have reduced LCOE compared to standalone CSP and can be cheaper than standard natural gas combined cycles depending on the price of fuel [37].

While the operating principle of heating feedwater or HP steam is the same for coal and natural gas, the implementation and modeling of each is very different. With the development of an accurate natural gas combined cycle model, the methods for solar field simulation, financial analysis, and optimization should be compatible to natural gas implementation. The development of a natural gas model can then be analyzed using the process outlined in Section 2.4 to define sub-systems for the calculation of solar contribution. It is expected that the optimization sub-objectives will still be valid for natural gas hybridization, though the scaling factors may need to be adjusted, as discussed in Section 2.6.

5.5 Photovoltaic Hybrids

Photovoltaic (PV) panels are a common technology used to offset auxiliary power throughout the developed world [91]. Direct generation-weighted average land use for PV panels ($2.9 \text{ ac GW}^{-1} \text{ yr}^{-1}$) is generally higher than for LFR and PTC (1.7 and $2.5 \text{ GW}^{-1} \text{ yr}^{-1}$, respectively). According to data from PacifiCorp, Hunter Unit 3 uses around 30 MW of auxiliary power that would be a candidate for PV hybridization. Using PV panels to offset the auxiliary power would lessen the electricity load from the plant on the turbine and allow that power to be sold to the consumer. With all else held constant, it seems reasonable to suggest that less coal would be required to meet grid demand when plant auxiliary power is offset with PV energy, allowing similar calculations for LCOE and PBT1 (Section 2.5).

A challenge with PV panels is their efficiency is highly dependent on operating temperature, so PV panels are often combined with active hydraulic cooling resulting in the popular photovoltaic thermal (PVT) solar collection technology [17]. PVT is a common technology used in residential markets to offset electricity demand and supplement the work of in-home water heaters [92]. Riggs et al. showed that PVT systems can be cost-competitive with natural gas for heating applications, particularly in states with high solar resource or high electricity and natural gas prices (HI, CA, AZ, NM). Chen et al. analyzed the possibility of PVT integration using methods similar to those discussed in Chapter 2. While Chen et al. were able to show that PVT can use less space than CSP, the benefit of PVT to coal plants is limited. The electricity generated from

the PV portion can effectively offset auxiliary power, but average temperatures for HTF in PVT systems are near 90 °C which would only provide a high enough temperature difference for for FWH 1 bypass or for preheating in series before FWH 1. And, as shown in Table 3.2, FWH 1 bypass optimization did not return a feasible value for both PTC and LFR and with no carbon tax.

5.6 Thermal Energy Storage

TES is a common solution to address the problem of CSP intermittency. TES can take many forms [79, 86, 93]

- Sensible Heat: Thermal energy is stored in a substrate, often liquid (molten salt TES) or solid (packed bed TES) [94, 95]
- Latent Heat: Thermal energy is transferred to a material that changes phase with the additional energy (phase change materials) [80, 85]
- Chemical Heat: Thermal energy is stored by causing a reversible chemical reaction [96]

Each technology is designed to quickly dispatch the energy stored throughout the day. The benefit of TES installation to CSP systems has been shown to increase the time CSP can be used to generate power, particularly during peak time or higher-priced hours depending on the market [97], improved power cycle efficiency [98], steady output temperature [99], higher and more stable electricity generation, and increase the daily average solar contribution [100].

The addition of TES to CSP-hybrid systems requires additional land and capital cost, but has been shown to be theoretically profitable. Zhai et al. showed in the lifecycle assessment (Chapter 1 that the CSP-hybrid configurations with TES all performed better than the best configuration without TES and far better than a coal power plant [22]. Ellingwood et al. has also shown reduction in LCOE when implementing storage and an increase in solar contribution to a natural gas power plant with solar tower integration [101]. A study on the Al-Abdaliyah hybrid plant in Kuwait (Table 1.1) has shown that adding TES increases the capacity of the hybrid plant in addition to the benefits listed above [30]. As research in TES systems continues, the associated capital costs and land use will likely decline and improve the feasibility of implementation in both standalone CSP systems and CSP-hybrid power plants.

REFERENCES

- [1] U.S. Energy Information Administration, 2020. Annual Energy Review <https://www.eia.gov/totalenergy/data/annual/> (Accessed on 07 Jan 2021). 1
- [2] Keho, Y., 2016. “What drives energy consumption in developing countries? The experience of selected African countries.” *Energy Policy*, **91**, 4, pp. 233–246. 1
- [3] U.S. Energy Information Administration, 2016. Carbon Dioxide Emissions Coefficients by Fuel. 1
- [4] Kostic, M. M., 2015. “Energy: Global and historical background.” *Encyclopedia of Energy Engineering*, 06, p. 15. 1
- [5] Stevens, L., Anderson, B., Cowan, C., Colton, K., and Johnson, D., 2017. The Footprint of Energy: Land Use of U.S. Electricity Production Tech. rep., Strata, 6. 2
- [6] National Renewable Energy Laboratory, 2020. Annual Technology Baseline <https://atb.nrel.gov/electricity/2020/> (Accessed on 09 Oct. 2020). 2
- [7] Zhang, H. L., Baeyens, J., Degrève, J., and Cacères, G., 2013. “Concentrated solar power plants: Review and design methodology.” *Renewable and Sustainable Energy Reviews*, **22**, pp. 466–481. 2
- [8] Zoschak, R., and Wu, S., 1975. “Studies of the direct input of solar energy to a fossil-fueled central station steam power plant.” *Solar Energy*, **17**(5), 11, pp. 297–305. 2
- [9] De Laquil III, P., Kearney, D., Geyer, M., and Diver, R., 1993. “Solar-Thermal Electric Technology.” In *Renewable Energy: Sources for Fuels and Electricity*, T. B. Johansson, H. Kelly, A. K. N. Reddy, and R. H. Williams, eds. Island Press, Washington, D.C., ch. 5, pp. 234–6. 2
- [10] Turchi, C., Langle, N., Bedilion, R., and Libby, C., 2011. Solar-Augment Potential of U.S. Fossil-Fired Power Plants Tech. rep., National Renewable Energy Laboratory, Golden, CO. 2
- [11] Pramanik, S., and Ravikrishna, R. V., 2017. “A review of concentrated solar power hybrid technologies.” *Applied Thermal Engineering*, **127**, pp. 602–637. 4, 9, 28
- [12] U.S. Energy Information Administration, 2016. Carbon Dioxide Emissions Coefficients by Fuel https://www.eia.gov/environment/emissions/co2_vol_mass.php (Accessed on 14 Apr. 2020). 4, 55
- [13] New York Times, 1916. American Inventor Uses Egypt’s Sun for Power, 7. 5

- [14] Kalogirou, S., 2007. “Recent Patents in Solar Energy Collectors and Applications.” *Recent Patents on Engineering*, **1**(1), 2, pp. 23–33. xi, 5, 6
- [15] Peterseim, J. H., White, S., Tadros, A., and Hellwig, U., 2013. “Concentrated solar power hybrid plants, which technologies are best suited for hybridisation?.” *Renewable Energy*, **57**, pp. 520–532. 6
- [16] Libby, C., Meagher, P., and Cerezo, L., 2010. Solar-Fossil Hybrid Power Plants: Summary Report on Conceptual Designs, 1022418 Tech. rep., Electric Power Research Institute, Palo Alto, CA. 7, 9, 60
- [17] Powell, K. M., Rashid, K., Ellingwood, K., Tuttle, J., and Iverson, B. D., 2017. “Hybrid concentrated solar thermal power systems: A review.” *Renewable and Sustainable Energy Reviews*, **80**, pp. 215–237. 7, 9, 61
- [18] Li, Y., and Yang, Y., 2014. “Thermodynamic analysis of a novel integrated solar combined cycle.” *Applied Energy*, **122**, pp. 133–142. 7
- [19] Zhao, Y., Liu, M., Wang, C., Li, X., Chong, D., and Yan, J., 2018. “Increasing operational flexibility of supercritical coal-fired power plants by regulating thermal system configuration during transient processes.” *Applied Energy*, **228**(July), pp. 2375–2386. 7
- [20] Mohammadi, K., Khanmohammadi, S., Khorasanizadeh, H., and Powell, K., 2020. “A comprehensive review of solar only and hybrid solar driven multigeneration systems: Classifications, benefits, design and prospective.” *Applied Energy*, **268**(March). 7
- [21] Ihsan, A., Jeppesen, M., and Brear, M. J., 2019. “Impact of demand response on the optimal, techno-economic performance of a hybrid, renewable energy power plant.” *Applied Energy*, **238**(January), pp. 972–984. 7
- [22] Zhai, R., Li, C., Chen, Y., Yang, Y., Patchigolla, K., and Oakey, J. E., 2016. “Life cycle assessment of solar aided coal-fired power system with and without heat storage.” *Energy Conversion and Management*, **111**, pp. 453–465. 7, 62
- [23] Manente, G., 2016. “High performance integrated solar combined cycles with minimum modifications to the combined cycle power plant design.” *Energy Conversion and Management*, **111**, pp. 186–197. 8, 9, 11, 55
- [24] Behar, O., Khellaf, A., Mohammedi, K., and Ait-Kaci, S., 2014. “A review of integrated solar combined cycle system (ISCCS) with a parabolic trough technology.” *Renewable and Sustainable Energy Reviews*, **39**, 7, pp. 223–250. ix, 9, 10
- [25] Rech, S., Lazzaretto, A., and Grigolon, E., 2018. “Optimum integration of concentrating solar technologies in a real coal-fired power plant for fuel saving.” *Energy Conversion and Management*, **178**(October), pp. 299–310. 9
- [26] Peng, S., Wang, Z., Hong, H., Xu, D., and Jin, H., 2014. “Exergy evaluation of a typical 330 MW solar-hybrid coal-fired power plant in China.” *Energy Conversion and Management*, **85**, pp. 848–855. 9

- [27] Zhao, Y., Hong, H., and Jin, H., 2017. "Optimization of the solar field size for the solarcoal hybrid system." *Applied Energy*, **185**, pp. 1162–1172. 9
- [28] Adibhatla, S., and Kaushik, S. C., 2017. "Energy, exergy, economic and environmental (4E) analyses of a conceptual solar aided coal fired 500 MWe thermal power plant with thermal energy storage option." *Sustainable Energy Technologies and Assessments*, **21**, pp. 89–99. ix, xi, 9, 16, 20, 21, 22, 56, A-1, C-3
- [29] Okoroigwe, E., and Madhlopa, A., 2016. "An integrated combined cycle system driven by a solar tower: A review." *Renewable and Sustainable Energy Reviews*, **57**, pp. 337–350. 9
- [30] Binamer, A. O., 2019. "Al-Abdaliya integrated solar combined cycle power plant: Case study of Kuwait, part I." *Renewable Energy*, **131**, 2, pp. 923–937. 9, 62
- [31] Sheu, E. J., Mitsos, A., Eter, A. A., Mokheimer, E. M. A., Habib, M. A., and Al-Qutub, A., 2012. "A Review of Hybrid SolarFossil Fuel Power Generation Systems and Performance Metrics." *Journal of Solar Energy Engineering*, **134**(4), p. 041006. 9
- [32] Sinha, M., 2017. NTPC's Dadri unit set to install solar-thermal hybrid power plant <https://energy.economictimes.indiatimes.com/news/renewable/ntpc-dadri-set-to-install-solar-thermal-hybrid-plant/57804545> (Accessed on 12 Jun. 2020). 9
- [33] National Renewable Energy Laboratory, 2020. Concentrating Solar Power Projects <https://solarpaces.nrel.gov/> (Accessed on 19 Nov. 2020). ix, 9, 10, 25, 26
- [34] Madler, M., 2017. Regulators Approve Palmdale Power Plant <https://sfvbj.com/news/2017/aug/11/regulators-approve-palmdale-power-plant/> (Accessed on 23 Apr. 2019). 9
- [35] Johnson, S., 2018. Plug pulled on Victorville power plant as land lease pursued <https://www.vvdailypress.com/news/20180425/plug-pulled-on-victorville-power-plant-as-land-lease-pursued> (Accessed on 23 Apr. 2019). 9
- [36] New Energy Update, 2017. CSP Today Global Tracker <http://tracker.newenergyupdate.com/tracker/projects> (Accessed on 12 Jun. 2020). 9
- [37] Alqahtani, B. J., and Patiño-Echeverri, D., 2016. "Integrated Solar Combined Cycle Power Plants: Paving the way for thermal solar." *Applied Energy*, **169**. 9, 61
- [38] Abdelhafidi, N., Bachari, N. E. I., Abdelhafidi, Z., Cheknane, A., Mokhnache, A., and Castro, L., 2019. "Modeling of integrated solar combined cycle power plant (ISCC) of Hassi R'mel, Algeria." *International Journal of Energy Sector Management*, **14**(3), p. 22. 9
- [39] Tannous, C., Ahlam, D., and Rosa, M., 2016. "Renewable energy integration into existing plants: Application: Deir Ammar thermal plant-North Lebanon." In *2016 3rd International Conference on Renewable Energies for Developing Countries, REDEC 2016*, Institute of Electrical and Electronics Engineers Inc., p. 9. 9

- [40] Wang, F., Li, H., Zhao, J., Deng, S., and Yan, J., 2016. “Technical and economic analysis of integrating low-medium temperature solar energy into power plant.” *Energy Conversion and Management*, **112**, pp. 459–469. 9, 52
- [41] Bakos, G. C., and Tsechelidou, C., 2013. “Solar aided power generation of a 300MW lignite fired power plant combined with line-focus parabolic trough collectors field.” *Renewable Energy*, **60**, pp. 540–547. 9
- [42] Zhao, Y., Hong, H., and Jin, H., 2015. “Thermo-economic Optimization of Solar-Coal Hybrid Systems.” *Energy Procedia*, **75**, pp. 457–461. 9
- [43] Mokheimer, E. M., Dabwan, Y. N., and Habib, M. A., 2017. “Optimal integration of solar energy with fossil fuel gas turbine cogeneration plants using three different CSP technologies in Saudi Arabia.” *Applied Energy*, **185**, pp. 1268–1280. 9
- [44] Choudhary, T., and Sanjay, 2017. “Thermodynamic assessment of SOFC-ICGT hybrid cycle: Energy analysis and entropy generation minimization.” *Energy*. 15
- [45] Cengel, Y. A., and Boles, M. A., 2011. *Thermodynamics: An Engineering Approach.*, 7 ed. McGraw-Hill, New York, NY. 18, 19, A-6, B-1
- [46] National Renewable Energy Laboratory, 2018. National Solar Radiation Database <https://maps.nrel.gov/nsrdb-viewer> (Accessed on 6 Nov. 2019). ix, 23, E-1
- [47] Sengupta, M., Xie, Y., Lopez, A., Habte, A., Maclaurin, G., and Shelby, J., 2018. “The National Solar Radiation Data Base (NSRDB).” *Renewable and Sustainable Energy Reviews*, **89**, 6, pp. 51–60. 23
- [48] Sait, H. H., Martinez-Val, J. M., Abbas, R., and Munoz-Anton, J., 2015. “Fresnel-based modular solar fields for performance/cost optimization in solar thermal power plants: A comparison with parabolic trough collectors.” *Applied Energy*, **141**, 3, pp. 175–189. 24
- [49] Rovira, A., Barbero, R., Montes, M. J., Abbas, R., and Varela, F., 2016. “Analysis and comparison of Integrated Solar Combined Cycles using parabolic troughs and linear Fresnel reflectors as concentrating systems.” *Applied Energy*. 24
- [50] Moya, E. Z., 2012. “7 - Parabolic-trough concentrating solar power (CSP) systems.” In *Woodhead Publishing Series in Energy*, K. Lovegrove and W. B. T. C. S. P. T. Stein, eds. Woodhead Publishing, pp. 197–239. 26
- [51] Zavoico, A. B., 2001. Solar Power Tower - Design Basis Document Tech. Rep. SAND2001-2100, Sandia National Laboratories, San Francisco, CA. 27, 28
- [52] Lemmon, E. W., , Bell, I. H., Huber, M. L., and McLinden, M. O., 2018. NIST Standard Reference Database 23: Reference Fluid Thermodynamic and Transport Properties-REFPROP, Version 10.0, National Institute of Standards and Technology <https://www.nist.gov/srd/refprop> (Accessed on 8 Jun. 2020). 28

- [53] Eastman Chemical Company, 2019. THERMINOL VP-1 heat transfer fluid brochure <https://www.therminol.com/product/71093459?pn=Therminol-VP-1-Heat-Transfer-Fluid> (Accessed on 8 Jun. 2020). 28
- [54] Qiu, Y., He, Y. L., Cheng, Z. D., and Wang, K., 2015. “Study on optical and thermal performance of a linear Fresnel solar reflector using molten salt as HTF with MCRT and FVM methods.” *Applied Energy*, **146**, pp. 162–173. 28
- [55] Vignarooban, K., Xu, X., Arvay, A., Hsu, K., and Kannan, A. M., 2015. “Heat transfer fluids for concentrating solar power systems - A review.” *Applied Energy*, **146**, pp. 383–396. 28
- [56] Channiwala, S. A., and Ekbote, A., 2015. “A Generalized Model to Estimate Field Size for Solar-Only Parabolic Trough Plant.” *Third South African Solar Energy Conference*, **3**(May), pp. 283–288. 30, 59
- [57] Hou, H., Xu, Z., and Yang, Y., 2016. “An evaluation method of solar contribution in a solar aided power generation (SAPG) system based on exergy analysis.” *Applied Energy*, **182**, pp. 1–8. 33, 34, A-1, A-2, A-4, A-9
- [58] Freeman, J., Blair, N., Guittet, D., Boyd, M., Neises, T., Wagner, M., Janzou, S., and Gilman, P., 2018. System Advisor Model. 36, D-1, D-2, D-3, D-4, D-7, D-8
- [59] GmbH, B.-D., Band, D., and Michalzik, R., 2009. BUDGET OFFER REVISION 3 Solar Steam Generator System PROJECT: SOLANA Tech. rep., SPX, Ratingen. 36
- [60] Montes, M. J., Rovira, A., Muñoz, M., and Martínez-Val, J. M., 2011. “Performance analysis of an Integrated Solar Combined Cycle using Direct Steam Generation in parabolic trough collectors.” *Applied Energy*, **88**, pp. 3228–3238. 36, 60
- [61] Turchi, C., 2010. Parabolic Trough Reference Plant for Cost Modeling with the Solar Advisor Model (SAM) Tech. Rep. July, National Renewable Energy Laboratory, Golden, CO. 36
- [62] Tax-Rates, 2020. Utah Property Taxes 2020 <http://www.tax-rates.org/> (Accessed on 25 Jan. 2020). 36
- [63] Bailey, N., 2019. Interview With Nathan Bailey from PacifiCorp. 36
- [64] Energysage, 2020. Investment tax credit for solar power <https://www.energysage.com/solar/cost-benefit/solar-investment-tax-credit/> (Accessed on 24 Jan. 2020). 36
- [65] Ramstein, C., Dominion, G., Ettehad, S., Lam, L., Quant, M., Zhang, J., Mark, L., Nierop, S., Berg, T., Leuschner, P., Merusi, C., Klein, N., and Trim, I., 2019. State and Trends of Carbon Pricing 2019 Tech. Rep. June 2019, World Bank Group, Washington, D.C. 37, 47, 56
- [66] PacifiCorp IRP Resource Planning, 2019. 2019 Integrated Resource Plan Tech. rep., PacifiCorp, Portland, OR. 37, 47

- [67] O'Shaughnessy, E., Heeter, J., Cook, J., and Volpi, C., 2017. Status and Trends in the US Voluntary Green Power Market (2016 Data) Tech. Rep. TP-6A20-70174, National Renewable Energy Laboratory, Golden, CO. 37, 48, 56
- [68] Zhai, R., Zhao, M., Tan, K., and Yang, Y., 2015. "Optimizing operation of a solar-aided coal-fired power system based on the solar contribution evaluation method." *Applied Energy*, **146**, 5, pp. 328–334. 39, A-1
- [69] Wang, Y., Xu, J., Chen, Z., Cao, H., and Zhang, B., 2017. "Technical and economical optimization for a typical solar hybrid coal-fired power plant in China." *Applied Thermal Engineering*, **115**, pp. 549–557. 39
- [70] Quirante, N., Caballero, J. A., and Grossmann, I. E., 2017. "A novel disjunctive model for the simultaneous optimization and heat integration." *Computers & Chemical Engineering*, **96**, 1, pp. 149–168. 39
- [71] Donado, K., Navarro, L., Quintero, M. C. G., and Pardo, M., 2019. "HYRES: A multi-objective optimization tool for proper configuration of renewable hybrid energy systems." *Energies*, **13**(1), 12. 39
- [72] Wang, J., Duan, L., Yang, Y., Yang, Z., and Yang, L., 2019. "Study on the general system integration optimization method of the solar aided coal-fired power generation system." *Energy*, 2, pp. 660–673. 39
- [73] Baghernejad, A., and Yaghoobi, M., 2011. "Exergoeconomic analysis and optimization of an Integrated Solar Combined Cycle System (ISCCS) using genetic algorithm." *Energy Conversion and Management*, **52**(5), 5, pp. 2193–2203. 39
- [74] Zhong, W., Chen, X., Zhou, Y., Wu, Y., and López, C., 2017. "Optimization of a solar aided coal-fired combined heat and power plant based on changeable integrate mode under different solar irradiance." *Solar Energy*, **150**, pp. 437–446. 39
- [75] Bravo, R., and Friedrich, D., 2018. "Two-stage optimisation of hybrid solar power plants." *Solar Energy*, **164**(January), pp. 187–199. 39
- [76] Qin, J., Hu, E., and Nathan, G. J., 2016. "The performance of a Solar Aided Power Generation plant with diverse configuration-operation combinations." *Energy Conversion and Management*, **124**, pp. 155–167. 52
- [77] Ong, S., Campbell, C., Denholm, P., Margolis, R., and Heath, G., 2013. Land-Use Requirements for Solar Power Plants in the United States Tech. rep., National Renewable Energy Laboratory, Golden, CO. 52
- [78] Bernal, B., Murray, L. T., and Pearson, T. R., 2018. "Global carbon dioxide removal rates from forest landscape restoration activities." *Carbon Balance and Management*, **13**(1). 55
- [79] Lizana, J., Chacartegui, R., Barrios-Padura, A., and Valverde, J. M., 2017. "Advances in thermal energy storage materials and their applications towards zero energy buildings: A critical review." *Applied Energy*, **203**, pp. 219–239. 55, 62

- [80] Pereira da Cunha, J., and Eames, P., 2016. “Thermal energy storage for low and medium temperature applications using phase change materials - A review.” *Applied Energy*, **177**, pp. 227–238. 55, 62
- [81] Xu, B., Li, P., and Chan, C., 2015. “Application of phase change materials for thermal energy storage in concentrated solar thermal power plants: A review to recent developments.” *Applied Energy*, **160**, pp. 286–307. 55
- [82] Flueckiger, S., Yang, Z., and Garimella, S. V., 2011. “An integrated thermal and mechanical investigation of molten-salt thermocline energy storage.” *Applied Energy*, **88**(6), pp. 2098–2105. 56
- [83] Tian, Y., and Zhao, C. Y., 2013. “A review of solar collectors and thermal energy storage in solar thermal applications.” *Applied Energy*, **104**, pp. 538–553. 56
- [84] Wu, J., Hou, H., Yang, Y., and Hu, E., 2015. “Annual performance of a solar aided coal-fired power generation system (SACPG) with various solar field areas and thermal energy storage capacity.” *Applied Energy*, **157**, pp. 123–133. 56
- [85] Reddy, K. S., Mudgal, V., and Mallick, T. K., 2018. “Review of latent heat thermal energy storage for improved material stability and effective load management.” *Journal of Energy Storage*, **15**, pp. 205–227. 56, 62
- [86] Kumar, A., and Shukla, S. K., 2015. “A Review on Thermal Energy Storage Unit for Solar Thermal Power Plant Application.” *Energy Procedia*, **74**, pp. 462–469. 56, 62
- [87] Dowling, A. W., Zheng, T., and Zavala, V. M., 2017. “Economic assessment of concentrated solar power technologies: A review.” *Renewable and Sustainable Energy Reviews*, **72**(January), pp. 1019–1032. 56
- [88] Vasquez Padilla, R., 2011. “Simplified Methodology for Designing Parabolic Trough Solar Power Plants.” PhD thesis, University of South Florida. 59
- [89] Manente, G., Rech, S., and Lazzaretto, A., 2016. “Optimum choice and placement of concentrating solar power technologies in integrated solar combined cycle systems.” *Renewable Energy*, **96**, pp. 172–189. 60
- [90] Korzynietz, R., Brioso, J. A., Del Río, A., Quero, M., Gallas, M., Uhlig, R., Ebert, M., Buck, R., and Teraji, D., 2016. “Solugas - Comprehensive analysis of the solar hybrid Brayton plant.” *Solar Energy*, **135**, pp. 578–589. 60
- [91] Masson, G., and Kaizuka, I., 2019. Trends in photovoltaic applications Tech. rep., International Energy Agency. 61
- [92] Hohne, P. A., Kusakana, K., and Numbi, B. P., 2019. “A review of water heating technologies: An application to the South African context.” *Energy Reports*, **5**, pp. 1–19. 61
- [93] Alva, G., Lin, Y., and Fang, G., 2018. “An overview of thermal energy storage systems.” *Energy*, **144**, pp. 341–378. 62

- [94] Li, G., 2016. “Sensible heat thermal storage energy and exergy performance evaluations.” *Renewable and Sustainable Energy Reviews*, **53**, pp. 897–923. 62
- [95] Yang, Z., and Garimella, S. V., 2010. “Thermal analysis of solar thermal energy storage in a molten-salt thermocline.” *Solar Energy*, **84**(6), pp. 974–985. 62
- [96] Li, L., Huang, H., Deng, L., Li, S., Li, J., Kobayshi, N., and Kubota, M., 2020. “Research progress of low-grade energy chemical heat storage materials.” *Huagong Jinzhan/Chemical Industry and Engineering Progress*, **39**(9), 9, pp. 3608–3616. 62
- [97] Sioshansi, R., and Denholm, P., 2010. “The Value of Concentrating Solar Power and Thermal Energy Storage in A production cost model.” *IEEE Transactions on Sustainable Energy*, **1**(3), pp. 173–183. 62
- [98] Kelly, B., Price, H., Brosseau, D., and Kearney, D., 2009. “Adopting Nitrate/Nitrite Salt Mixtures as the Heat Transport Fluid in Parabolic Trough Power Plants.” *Proceedings of ES2007*, pp. 1033–1040. 62
- [99] Pelay, U., Luo, L., Fan, Y., Stitou, D., and Rood, M., 2017. “Thermal energy storage systems for concentrated solar power plants.” *Renewable and Sustainable Energy Reviews*, **79**(March), pp. 82–100. 62
- [100] Grange, B., Dalet, C., Falcoz, Q., Ferrière, A., and Flamant, G., 2016. “Impact of thermal energy storage integration on the performance of a hybrid solar gas-turbine power plant.” *Applied Thermal Engineering*, **105**, pp. 266–275. 62
- [101] Ellingwood, K., Safdarnejad, S., Rashid, K., and Powell, K., 2018. “Leveraging Energy Storage in a Solar-Tower and Combined Cycle Hybrid Power Plant.” *Energies*, **12**(1), p. 40. 62
- [102] Zhai, R., Yang, Y., Zhu, Y., and Chen, D., 2013. “The evaluation of solar contribution in solar aided coal-fired power plant.” *International Journal of Photoenergy*, **2013**. A-1
- [103] Hu, E., Yang, Y. P., Nishimura, A., Yilmaz, F., and Kouzani, A., 2010. “Solar thermal aided power generation.” *Applied Energy*. A-1
- [104] Zhu, G., Neises, T., Turchi, C., and Bedilion, R., 2015. “Thermodynamic evaluation of solar integration into a natural gas combined cycle power plant.” *Renewable Energy*, **74**, pp. 815–824. A-1
- [105] Zhao, Y., Hong, H., and Jin, H., 2014. “Evaluation criteria for enhanced solar-coal hybrid power plant performance.” *Applied Thermal Engineering*, **73**(1), pp. 575–585. A-1
- [106] Valero, A., Serra, L., and Uche, J., 2006. “Fundamentals of exergy cost accounting and thermoeconomics. Part II: Applications.” *Journal of Energy Resources Technology, Transactions of the ASME*, **128**(1), 3, pp. 9–15. A-1
- [107] Li, J., Yu, X., Wang, J., and Huang, S., 2016. “Coupling performance analysis of a solar aided coal-fired power plant.” *Applied Thermal Engineering*, **106**, 8, pp. 613–624. xii, C-3, C-4

- [108] Cambell, M., 2008. The Drivers of the Levelized Cost of Electricity for Utility-Scale Photovoltaics Tech. rep., Sunpower Corporation, San Jose, CA. D-1
- [109] U.S. Energy Information Administration, 2019. Levelized Cost and Levelized Avoided Cost of New Generation Resources-AEO2019 Tech. rep., U.S. Energy Information Administration. D-1
- [110] Short, W., Packey, D., and Holt, T., 1995. A manual for the economic evaluation of energy efficiency and renewable energy technologies Tech. rep., National Renewable Energy Laboratory (NREL), Golden, CO, 3. D-2, D-5, D-6
- [111] Finance Formulas, 2019. Loan Payment https://financeformulas.net/Loan_Payment_Formula.html (Accessed on 25 Jan. 2020). D-3
- [112] The United States of America Congress, 2016. Consolidated Appropriations Act of 2016. D-4
- [113] Turchi, C., Mehos, M., Ho, C. K., and Kolb, G. J., 2010. “Current and future costs for parabolic trough and power tower systems in the US market.” *Renewable Energy*(October), p. 11. D-7
- [114] Adibhatla, S., and Kaushik, S. C., 2017. “Energy, exergy, economic and environmental (4E) analyses of a conceptual solar aided coal fired 500 MWe thermal power plant with thermal energy storage option.” *Sustainable Energy Technologies and Assessments*, **21**, pp. 89–99. D-8
- [115] Duffie, J. A., and Beckman, W. A., 1985. “Solar Engineering of Thermal Processes.” *American Journal of Physics*, **53**(4), pp. 382–382. D-9, D-10
- [116] U.S. Energy Information Association, 2019. Utah State Energy Profile Tech. rep., U.S. Energy Information Association, Washington, D.C. D-10
- [117] World Nuclear Association, 2016. Heat values of various fuels <https://www.world-nuclear.org/information-library/facts-and-figures/heat-values-of-various-fuels.aspx> (Accessed on 29 Jan. 2020). D-10
- [118] Lilliestam, J., Thonig, R., Gilmanova, A., Zang, C., and Trondle, T., 2020. CSP Database csp.guru (Accessed on 06 Jan. 2021). D-10

APPENDIX A. SOLAR CONTRIBUTION

A.1 Introduction

To better understand the benefits of integrating concentrated solar power (CSP) with coal power generation, a process of estimating the solar contribution (\dot{W}_s) of a hybrid solar and coal power plant is developed. \dot{W}_s is the portion of power generated from the hybrid power plant that can be directly credited to the CSP augmentation.

To understand the amount of generated electricity that can be attributed to CSP, researchers have developed various methods to calculate \dot{W}_s . Based on a study conducted by Zhai et al. [102], approaches to analyzing \dot{W}_s have focused primarily on energy balance [28, 103–105], exergy balance [68], and thermoeconomics [106]. Hou et al. [57] states that methods that rely exclusively on energy flow result in an over estimate of \dot{W}_s because either the change of coal unit efficiency is ignored or the difference of quality between solar energy and coal is not considered. To account for energy grade differences, Hou used a method "Based on the first and second laws of thermodynamics and the characteristics of exergy flows crossing the boundaries of the subsystems" [57]. The method of calculating the solar contribution based primarily off of the method used by Hou with various changes for use in the optimization of CSP hybridization is discussed below. Results based on various locations of CSP integration and varying augment fractions are also included.

A.2 Method

The methods used to estimate \dot{W}_s are based primarily on the method developed by Hou et al. [57]. Hou developed this model for solar contribution by first dividing the power plant into subsystems and then calculating the portion of solar exergy destruction in each subsystem. The solar contribution was estimated by determining the difference between solar exergy addition and solar exergy destruction. This study adapts Hou's methods for a generalized, non-ideal cycle.

A.2.1 Equation for Calculation of Solar Contribution

\dot{W}_s is calculated by determining the exergy from the solar field that is converted to usable work. Equation A.1 from Hou et al. [57] estimates \dot{W}_s from the sum of the solar proportion of work output (r_s) and exergy destroyed (x_d) for the i^{th} subsystem up to N subsystems, the maximum mass flow rate of steam (\dot{m}_{max}), and the exergy transferred from the CSP augmentation (x_s).

$$\dot{W}_s = \frac{1}{1000} \dot{m}_m (x_s - \sum_{i=1}^N r_{s,i} \cdot x_{d,i}) \quad (\text{A.1})$$

A.2.2 Solar Heat Exchange Exergy Flow

x_s is calculated as shown in Equation A.2 from Hou et al. [57]. Equation A.2 uses the specific enthalpy (h kJ kg⁻¹) and specific entropy (s kJ kg⁻¹ K⁻¹) flowing into and out of the solar heat exchanger, T_0 , \dot{m}_m , and the mass flow rate through the solar heat exchanger (\dot{m}_{SX}).

$$x_s = \frac{\dot{m}_{SX}}{\dot{m}_m} [(h_{in} - h_{out}) - T_0(s_{in} - s_{out})] \quad (\text{A.2})$$

A.2.3 Division of Subsystems

Following the method from Hout et al., the block is divided into subsystems. Hou et al. developed subsystems by dividing the power plant according to the exhaust ports in the turbines, such that each subsystem aligns with the pressure stages of the turbines. The model used in this study can be divided into four subsystems following the method in Hou et al. (Figure A.1). When combined, the subsystems should include all components with the exception of the boiler and HTF to water solar heat exchanger (SX). Each subsystem remains consistent across multiple solar integration configurations. The only modification is the inclusion of the solar integration in different subsystems as the integration location changes. For example, Subsystem 4 always contains the lower stages of the LPT, the Condenser, CP, and drain cooler throttling after the LP FWH. For the lowest pressure solar integration (Figure 2.8a), the SX occurs before LP FWH and splits that boundary between subsystems 3 and 4. Similarly for options B-D, the subsystem boundaries are

drawn to exclude the solar integration. The subsystem divisions for each configuration considered in this study are included in Appendix G.

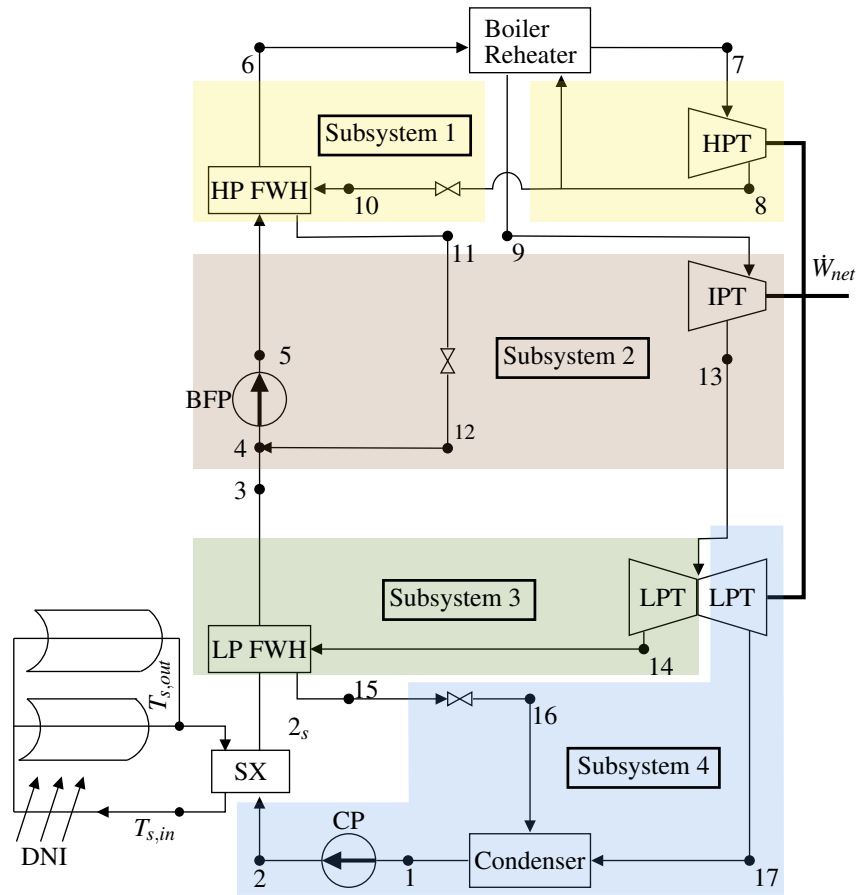


Figure A.1: CSP-coal hybrid power plant diagram with subsystem divisions for bypass of FWHs 1 & 2

Subsystem boundary lines are selected based on the level of turbine as shown in Figure A.1 with extraction and exhaust pressures. However, since steam is not extracted from the IP turbine, the boundary line is determined from the pressure at node 13. Figure A.2 illustrates the boundary lines for each subsystem when plotted on a T-s diagram.

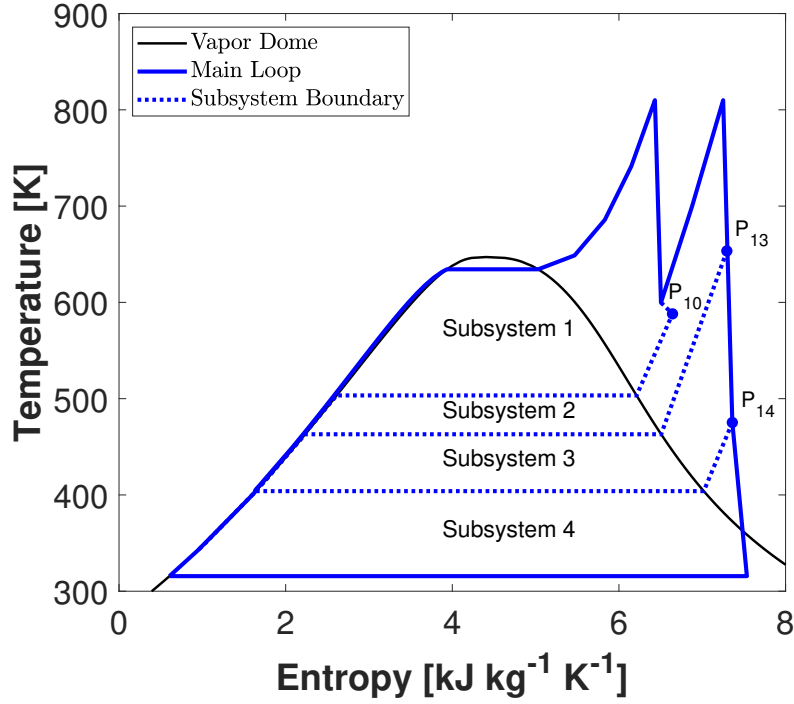


Figure A.2: Temperature vs entropy plot of main loop of CSP-coal hybrid power plant subsystems.

A.2.4 Calculation of Solar Proportion of Work Output

Once subsystems are determined, the next step is to calculate the solar proportion of work output (r_s). Equation A.3 defines r_s as the ratio of reversible solar work output ($\dot{w}_{s,rev}$) to the total reversible work output (\dot{w}_{rev}) where \dot{w}_{rev} is the sum of $\dot{w}_{s,rev}$ and the coal work output $\dot{w}_{f,rev}$.

$$r_s = \frac{\dot{w}_{s,rev}}{\dot{w}_{rev}} = \frac{\dot{w}_{s,rev}}{\dot{w}_{s,rev} + \dot{w}_{f,rev}} \quad (\text{A.3})$$

Hou et al. [57] defines $\dot{w}_{s,rev}$ and $\dot{w}_{f,rev}$ as the integral of the temperature curve through the solar heat exchange and the boiler respectively. Using the equations for reversible work assumes that the heat transfer out of the subsystem is negligible compared to the irreversibilities contained within the subsystem. Equations A.4 and A.5 demonstrate the process to calculate $\dot{w}_{s,rev}$ and $\dot{w}_{f,rev}$ respectively. Figure A.3 illustrates this process for subsystem 3.

$$\dot{w}_{s,rev,i} = \frac{\dot{m}_s}{\dot{m}_m} \int_{S_{s,1}}^{S_{s,2}} [T_{i-1}(s) - T_i(s)] ds \quad (\text{A.4})$$

$$\begin{cases} \dot{w}_{f,rev,i} = \int_{S_6}^{S_7} [T_{i-1}(s) - T_i(s)] ds & i = 1 \\ \dot{w}_{f,rev,i} = \int_{S_6}^{S_7} [T_{i-1}(s) - T_i(s)] ds + \frac{\dot{m}_{th}}{\dot{m}_m} \int_{S_8}^{S_9} [T_{i-1}(s) - T_i(s)] ds & i = 2, 3, 4 \end{cases} \quad (\text{A.5})$$

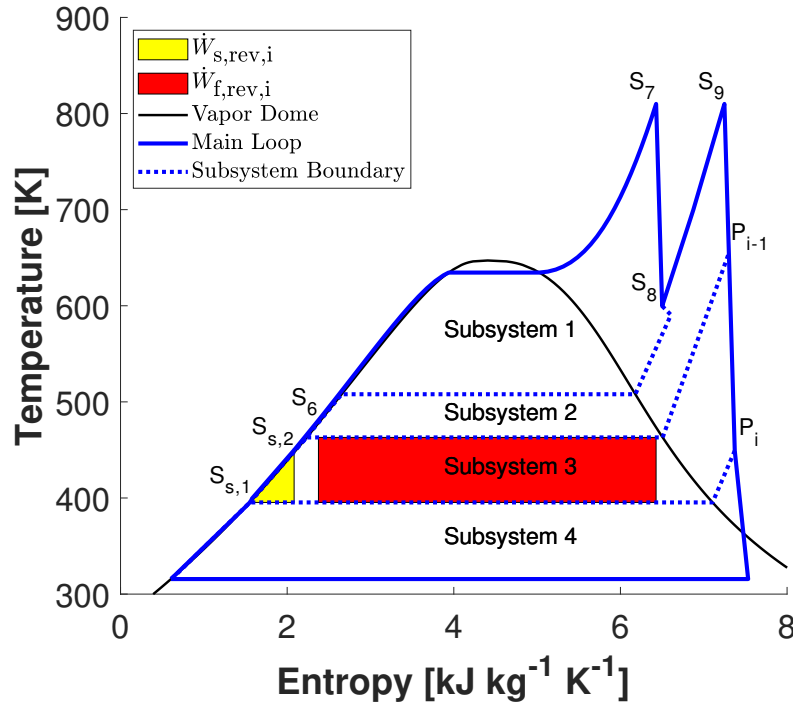


Figure A.3: Temperature vs entropy plot of main loop of CSP-coal hybrid power plant subsystems demonstrating the calculation of reversible work for subsystem i

Figure A.3 illustrates the process for calculating reversible work for subsystem 3 bounded by P_9 and P_{14} . The boundary line between subsystems 1 and 2 varies due to the throttle between nodes 8 and 10. Since P_8 is different than P_{10} , P_i for subsystem 2 is equal to P_8 before the throttle and is throttled down to equal P_{10} after the throttle. This allows for the temperature curve to account for the throttling between nodes 8 and 10.

Since the solar integration site changes, the location of $S_{s,1}$ and $S_{s,2}$ is subject to change. For the scenario that the solar exchange occurs after node 6, S_6 would be adjusted to be equal to $S_{s,2}$.

Equations A.4 and A.5 are applied by using the trapezoid rule to estimate the area under the temperature curves for each constant pressure boundary line. The upper boundary curve for subsystem 1 cannot be represented by a constant pressure line because of the pressure drop across the boiler. To account for the pressure drop in subsystem 1, $\dot{w}_{f,\text{rev}}$ is determined by setting it equal to the heat transferred into the water from the boiler. This process is justified by rearranging the entropy balance and energy balance equations to solve for heat transferred into the boiler [45]. The process for determining the heat transferred into the boiler q is demonstrated in Equation A.6 where T is the temperature curve through the boiler and upper boundary line for subsystem 1.

$$q = \int T(s)ds = h_7 - h_6 \quad (\text{A.6})$$

Equation A.6 shows that q is equal to the integral under the temperature curve through the boiler which allows for $\dot{w}_{f,\text{rev}}$ to be determined for subsystem 1 by finding the difference between q and the area under the lower boundary line of subsystem 1. Equation A.7 solves for $\dot{w}_{f,\text{rev}}$ by substituting Equation A.6 for the integral over $T_{i-1}(s)$ in Equation A.4. For Equation A.7, $T_i(s)$ is the temperature curve for the the lower boundary line of subsystem 1.

$$\dot{w}_{f,\text{rev}} = h_7 - h_6 - \int_{s_6}^{s_7} T_i(s)ds \quad (\text{A.7})$$

A.2.5 Calculation of Exergy Destruction

Exergy destruction is calculated by treating each subsystem as a control volume and performing an exergy balance. Equation A.8 expresses the exergy balance for steady flow systems where T_0 is the dead state temperature, T_k is the boundary temperature, \dot{Q}_k is the rate of heat crossing the boundary at T_k , \dot{W}_{out} is the rate that work crosses the boundary line, \dot{X}_{in} and \dot{X}_{out} are respectively exergy entering and leaving the subsystem through mass flow, and \dot{X}_d is the exergy destroyed [45]. \dot{Q}_k is assumed to be entering and \dot{W}_{out} is assumed to be leaving the subsystem.

$$\sum_k^N \left(1 - \frac{T_0}{T_k}\right) \dot{Q}_k - \dot{W}_{\text{out}} + \dot{X}_{\text{in}} - \dot{X}_{\text{out}} - \dot{X}_d = 0 \quad (\text{A.8})$$

The only subsystem that has a value for \dot{Q}_k is subsystem 4 as a result of the condenser, however it is assumed that $T_0 = T_b$ for the condenser to include all irreversibilities in the system. Work leaving each subsystem can be divided into work leaving through the turbine (\dot{W}_t) and entering through the pump (\dot{W}_p). Equation A.8 is simplified to solve for \dot{X}_d .

$$\dot{X}_d = \dot{X}_{\text{in}} - \dot{X}_{\text{out}} + \dot{W}_p - \dot{W}_t \quad (\text{A.9})$$

It is important to note that each of the subsystems have multiple mass flow rates (\dot{m}) crossing the boundary line. For example, in subsystem 2 \dot{m} through the IPT is different than \dot{m} through the BFP. To allow for the value of \dot{X}_d in each subsystem to be considered for the solar contribution of the entire power plant, \dot{X}_d is scaled by the mass flow rate of the main stream (\dot{m}_m) as demonstrated in Equation A.10.

$$x_d = \frac{\dot{X}_d}{\dot{m}_m} \quad (\text{A.10})$$

A.3 Results

The validity of the solar contribution analysis presented here compared to results published in Hou et al. is demonstrated in Section 2.4.

The methods used to calculate solar contribution were tested for several k at each integration site, results for which are provided in Table 2.1. T-s diagrams for different solar contribution simulations are provided for $k = 3\%$ bypassing FWHs 3 and 7 (Figure A.4) and FWH 7 bypass of $k = 1, 6\%$ (Figure A.5).

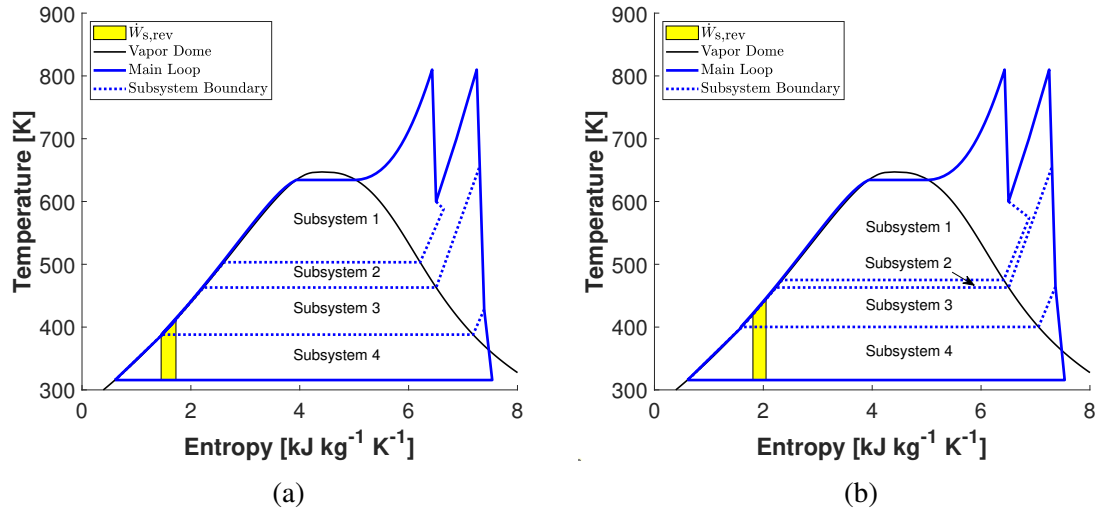


Figure A.4: Temperature vs entropy plot for FWH 3 bypass with an augment fraction of $k = 3\%$ (a) and FWH 7 bypass with an augment fraction of $k = 3\%$ (b).

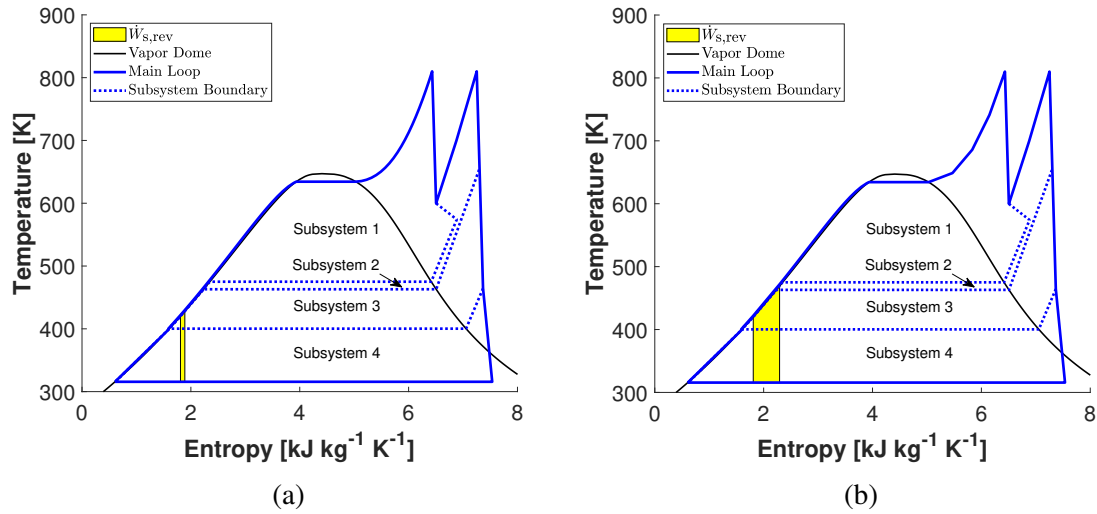


Figure A.5: Temperature vs entropy plot for FWH 7 bypass with an augment fraction of $k = 1\%$ (a) and FWH 7 bypass with an augment fraction of $k = 6\%$ (b).

A.4 Conclusion

CSP integration close to the boiler at a high k value maximises the solar contribution. This conclusion was determined by estimating the solar contribution based on the process described in Hou et al. [57] and adapted to a simplified model. The process developed in this study generalized the division of the power plant into subsystems, and calculated the solar proportion of exergy destroyed in each subsystem. This allowed for the solar contribution to be determined from the difference of the exergy transferred from the solar field and the exergy destroyed.

APPENDIX B. STATE PROPERTIES

Simulating the performance of the simplified model requires multiple input values, relationships, and equations relating to equipment performance or operating behavior of the hardware being modeled. A derivative of the state postulate requires two independent, intensive properties to fix the state of a simple compressible system [45]. Thus, for each state in the representative model, two properties that are independent of each other and do not depend on mass (intensive) must be provided to determine the other properties of interest at that state.

For the model presented in this work, we are particularly interested in the following properties.

- Pressure (P [MPa])
- Temperature (T [K])
- Specific enthalpy (h [kJ kg⁻¹])
- Specific entropy (s [kJ kg⁻¹ K⁻¹])
- Steam quality (x) $\frac{m_{\text{vapor}}}{m_{\text{total}}}$

The information required to obtain these properties can be separated into four categories

1. Correlation provided by user (Table F.1)
2. Process design points
3. Conservation of energy
4. Efficiency

We have selected the HPT 1st stage pressure as the control parameter used to adjust the power generation of the plant. Because this pressure is the independent variable, all correlations (category 1) used to calculate the properties for the simulation of the Hunter plant are related to the HPT 1st stage pressure (Table F.1).

The description of state point values are provided sequentially below beginning with state 1. When the properties of a state are dependent on a process related to a later state, some conditions are introduced out of order.

The pressure at state 1 is equivalent to the condenser operating pressure, provided as a correlation in Table F.1 (category 1). The water in condensers is designed to exit as a saturated liquid, so the second property to fix state 1 is $x = 0$ (category 2).

The feedwater in the condensate stage of real power plants incrementally increases in pressure as it is heated until it enters the DA. In the simplified model, the condensate stage is assumed to take place at constant pressure ($P_2 = P_3 = P_4$), as opposed to the gradual compression experienced in the real plant. This pressure is approximated using a correlation in Table F.1 for the DA extraction pressure (category 1). The CP is assumed to have a constant isentropic efficiency. The isentropic efficiency of a pump is defined as the ratio of the isentropic work ($\Delta s = 0$) to the actual work. For pumps with an outlet enthalpy (h_e) and inlet enthalpy (h_i), the work done by that pump can be derived from conservation of energy to get Equation B.1.

$$W_{\text{pump}} = \dot{m}(h_e - h_i) \quad (\text{B.1})$$

The isentropic efficiency can then be written in terms of the actual work (W_a) and isentropic work (W_s) in Equation B.2.

$$\eta_{\text{pump}} = \frac{W_s}{W_a} = \frac{h_{e,s} - h_i}{h_{e,a} - h_i} \quad (\text{B.2})$$

After finding the isentropic enthalpy of state 2 ($h_{e,s} = h(P_2, s_1)$), the actual enthalpy can be calculated using the isentropic efficiency (Equation B.2), which fixes state 2 (category 4).

The enthalpy of state 3 is determined using the FWH efficiency. This method can be written in terms of states 2, 14, and 15 in Equation B.3 (category 2).

$$h_3 = \frac{\eta_{\text{FWH}}}{\dot{m}_{14}(h_{14} - h_{15})} + h(2) \quad (\text{B.3})$$

State 3 is then fixed knowing h_3 and that $P_3 = P_2$, as stated previously (category 2).

State 4 is a simplified model of the DA used in coal plants to remove air from the feedwater before it enters the boiler. The ideal version of a DA is a mixing chamber. In the case of state 4, condensate stream 3 and FWH drain exit (state 12) enter the chamber at equal pressure and exit at

the same pressure ($P_3 = P_4 = P_{12}$, category 2). State 4 is fixed after finding the enthalpy of state 4 using the conservation of energy (category 3). For a steady, open system with no external heating or work interactions, N inlet streams, and M exit streams,

$$\sum_j^M (\dot{m}_j h_j)_{\text{exit}} = \sum_k^N (\dot{m}_k h_k)_{\text{in}} \quad (\text{B.4})$$

and, therefore,

$$h_4 = \frac{1}{\dot{m}_4} (\dot{m}_3 h_3 + \dot{m}_{12} h_{12}) \quad (\text{B.5})$$

However, h_{12} is still unknown for this process. In order to calculate states 4, 11, and 12, a temperature for state 5 is assumed and used with a correlation for pressure in Table F.1 (category 1) to fix the state. The temperature for state 11 is determined using the Drain Cooler (DC) temperature difference specification for FWHs. The DC approach assumes that the drain of the FWH exits at a specified temperature difference above the feedwater inlet temperature. In the case of the HP FWH, T_{11} can be related to the assumed T_5 using Equation B.6 (category 2).

$$T_{11} = T_5 + DC \quad (\text{B.6})$$

It is assumed that the steam exits the FWH for state 11 at the same pressure as the extraction inlet ($P_{11} = P_{10}$, category 2). State 11 is then fixed and can be used to determine state 12.

It has been identified previously that state 12 is at the same pressure as states 3 and 4. A relationship for the throttling process is useful to fix state 12 (category 3). A general expression for a control volume at steady state with no external heating or work interactions is presented in Equation B.5. Equation B.7 shows the results for a single inlet and exit. Since $\dot{m}_{12} = \dot{m}_{11}$, the enthalpy at states 11 and 12 are equivalent.

$$\sum_j^M (\dot{m}_j h_j)_{\text{exit}} = \sum_k^N (\dot{m}_k h_k)_{\text{in}} \quad (\text{B.7})$$

State 4 is then fixed as previously described and can be used to evaluate the assumed T_5 . The new state 5 is fixed using the boiler feed pump (BFP) efficiency (category 4), as described for state 2 (Equation B.2) and a pressure calculated from a correlation in Table F.1 (category 1). The temperature from the new state 5 is compared to the assumed state. A tolerance of 0.1% is applied

for sensitivity when comparing the assumed and calculated state 5 temperatures. The properties of the calculated state 5 are then used to iterate through the calculations for states 4, 11, and 12 until the tolerance requirement is met.

State 6 is calculated assuming a FWH efficiency (η_{FWH}) based on the conservation of energy (category 3). For a FWH, the amount of energy transferred between the streams can be determined by analyzing the heat transfer material, or the space between the extraction and feedwater streams. Since the extracted steam and feedwater heat rates are related by η_{FWH} ,

$$\eta_{FWH} \dot{m}_{10-11}(h_{10} - h_{11}) = \dot{m}_{5-6}(h_6 - h_5) \quad (\text{B.8})$$

and, therefore,

$$h_6 = h_5 + \eta_{FWH} \frac{\dot{m}_{10-11}}{\dot{m}_{5-6}}(h_{10} - h_{11}) \quad (\text{B.9})$$

State 6 can then be fixed using Equation B.9 and the pressure, assuming $\eta_{FWH} \approx 99\%$.¹ Similar to the LP FWH, the feedwater exit is assumed to be at the same pressure as the inlet ($P_6 = P_5$, category 2).

State 7 is at the exit of the boiler. For lack of a model for pressure losses in the boiler, a correlation is provided for the boiler outlet pressure in Table F.1 (category 1). It is assumed that a boiler operates at constant temperature (category 1).²

The exhaust or extraction properties from a turbine are dependent on turbine pressure limits and its isentropic efficiency. For the example of the HPT exhaust (state 8), the inlet pressure has already been calculated (P_7). The pressure ratio from the inlet of the HPT to the exhaust varies with P_{s1} , but it is assumed that the pressure ratio from P_{s1} to the HPT exhaust is constant.³ Since the 1st stage pressure is set for a plant operating condition, the HPT exhaust pressure can be calculated using a constant pressure ratio (category 1).

The isentropic efficiency of an adiabatic turbine is similar to Equation B.2 for compressor efficiency.

$$\eta_{\text{turb}} = \frac{W_a}{W_s} = \frac{h_{e,a} - h_i}{h_{e,s} - h_i} \quad (\text{B.10})$$

¹ $\eta_{FWH} = 99\%$ confirmed with operating data from Hunter Unit 3

²Data from Hunter Unit 3 confirms constant operating temperature as reported in Table F.1.

³The constant P_{s1} -HPT exhaust pressure ratio is confirmed with data from Hunter Unit 3.

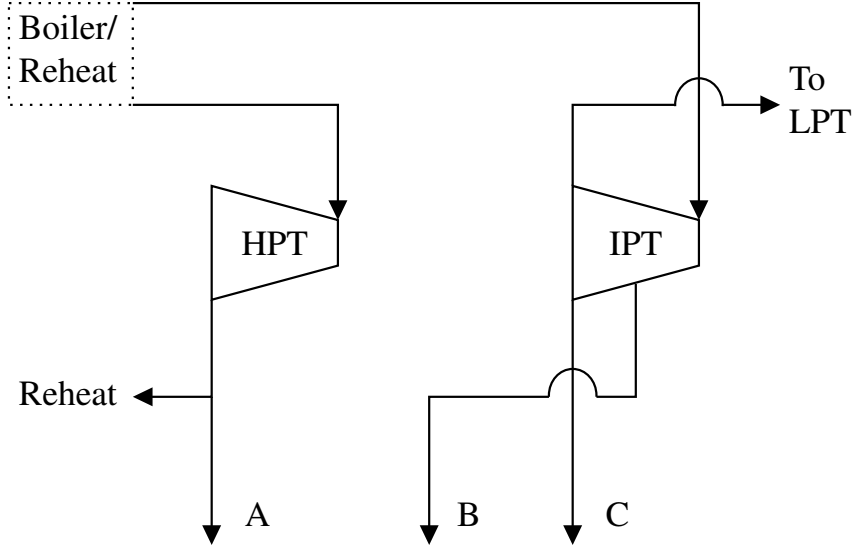


Figure B.1: Generalized schematic to illustrate the process of calculating the mass-averaged pressure used in the simplified model.

For a specified turbine efficiency (category 1), the exit state can be fixed by rearranging Equation B.10 to solve for $h_{e,a}$ (category 4).

The boiler reheating is assumed to be a constant pressure process ($P_9 = P_8$, category 2). As discussed previously, the boiler operates at a consistent temperature, thus it is assumed that $T_9 = T_7$ (category 2). As long as the water is not a saturated liquid-vapor mixture, pressure and temperature are independent and state 9 is fixed.

Multiple options for modeling state 10 have been considered (Appendix C); the selected option is to throttle a fraction of the steam extracted from the HPT exhaust to the mass-averaged pressure. The process to calculate the mass-averaged pressure is based on a generalized schematic in Figure B.1.

In the case represented in Figure B.1, there are 3 HP FWHs with a single extraction from the HPT exhaust (A) and 2 extractions from the IPT (B, C). First, the FWH mass fraction (mf) is calculated using a ratio of the respective extraction mass flow rate to the total mass extracted, as in Equation B.11 for the FWH mass fraction of stream A.

$$mf_A = \frac{\dot{m}_A}{\dot{m}_A + \dot{m}_B + \dot{m}_C} \quad (\text{B.11})$$

The mass-averaged pressure is assumed to be the combination of each of the individual extraction pressures (Equation B.12) while the extraction mass flow rate in the simplified model is assumed to be equal to the sum of the extraction flow rates.

$$P_{\text{mavg}} = mf_A P_A + mf_B P_B + mf_C P_C \quad (\text{B.12})$$

This mass-average process is implemented using the correlations for turbine pressure ratios and mass fractions listed in Table F.1 (category 1) to determine the throttling pressure and extraction mass flow rate for state 10 (category 2). State 10 is fixed using the isenthalpic valve assumption as in Equation B.7 (category 3).

The extraction mass flow rate used in the mass-average process is calculated using extraction fractions (m_{ef}). For HP extractions, m_{ef} is the fraction of the mass differential between the main steam flow (\dot{m}_7) and the DA inlet (\dot{m}_3). The LP m_{ef} are the fractions of the mass flow into the LPT (\dot{m}_{13}). Values for m_{ef} are determined by plant operating data.

The pressure at the exit of the IPT (state 13) is specified by a correlation for the IPT pressure ratio in Table F.1 (category 1). The enthalpy for state 13 is determined using the turbine isentropic efficiency (Equation B.10, category 4).

States 14 and 17 are also fixed using exit pressures and the LPT isentropic efficiency (Equation B.10, category 1). The extraction pressure (P_{14}) is assumed to be at the mass-averaged pressure from the real power plant LP FWHs as described in Equation B.12 (category 2). The LPT is assumed to exhaust to the condenser, i.e. $P_{17} = P_1$ (category 2).

States 15 and 16 are determined in the same way as states 11 and 12, using the DC approach (Equation B.6, category 2) at constant pressure ($P_{15} = P_{14}$, category 2) and isenthalpic valve assumption (Equation B.7, category 3) exiting at the condenser pressure ($P_{16} = P_1$, category 2).

In summary, below is a list of inputs the model requires in order to simulate the power plant performance:

- Condenser pressure
- All FWH extraction pressures
- Boiler inlet pressure

- Boiler outlet pressure
- Boiler operating temperature
- Boiler inlet mass flow rate
- DA inlet water mass flow rate
- Extraction fractions for each FWH
- HPT 1st stage-exhaust pressure ratio
- HPT, IPT, LPT isentropic efficiencies
- IPT, LPT extraction pressure ratios

APPENDIX C. HP FWH EXTRACTION

C.1 Overview

Combining multiple FWHs from a plant schematic into a single FWH in the representative model simplifies calculations but creates a problem in calculating properties of the extraction steam. The extraction pressure is calculated using a mass averaged approach as has been discussed. One other property must be known in order to determine the other properties of the extraction state. Each state in the representative model is determined by correlations to actual plant data and by operating relationships for the hardware to which the state relates. In the case of the HP FWH extraction steam, knowing the pressure from the mass averaged approach is insufficient; the extraction location within the cycle must also be known.

C.2 Methods

Each coal plant has a unique FWH configuration, varying the number of heaters, extraction locations, and extraction pressures. However, HP FWHs are always operated using steam extracted from either the HPT or IPT. Thus, extraction from the HPT or IPT is considered for the representative model. Specifically, the following options were considered for FWH extraction and are illustrated in Figure C.1:

1. HPT exhaust at HPT exhaust pressure (Figure C.1a)
2. HPT exhaust throttled to mass averaged pressure (Figure C.1b)
3. IPT extraction at mass averaged pressure (Figure C.1c)

Using steam at the HPT exhaust pressure is infeasible because there would be no difference in plant performance when the FWH number from the real plant is changed. Thus, results from options 2 and 3 will be reported and discussed in terms of accuracy and computational performance.

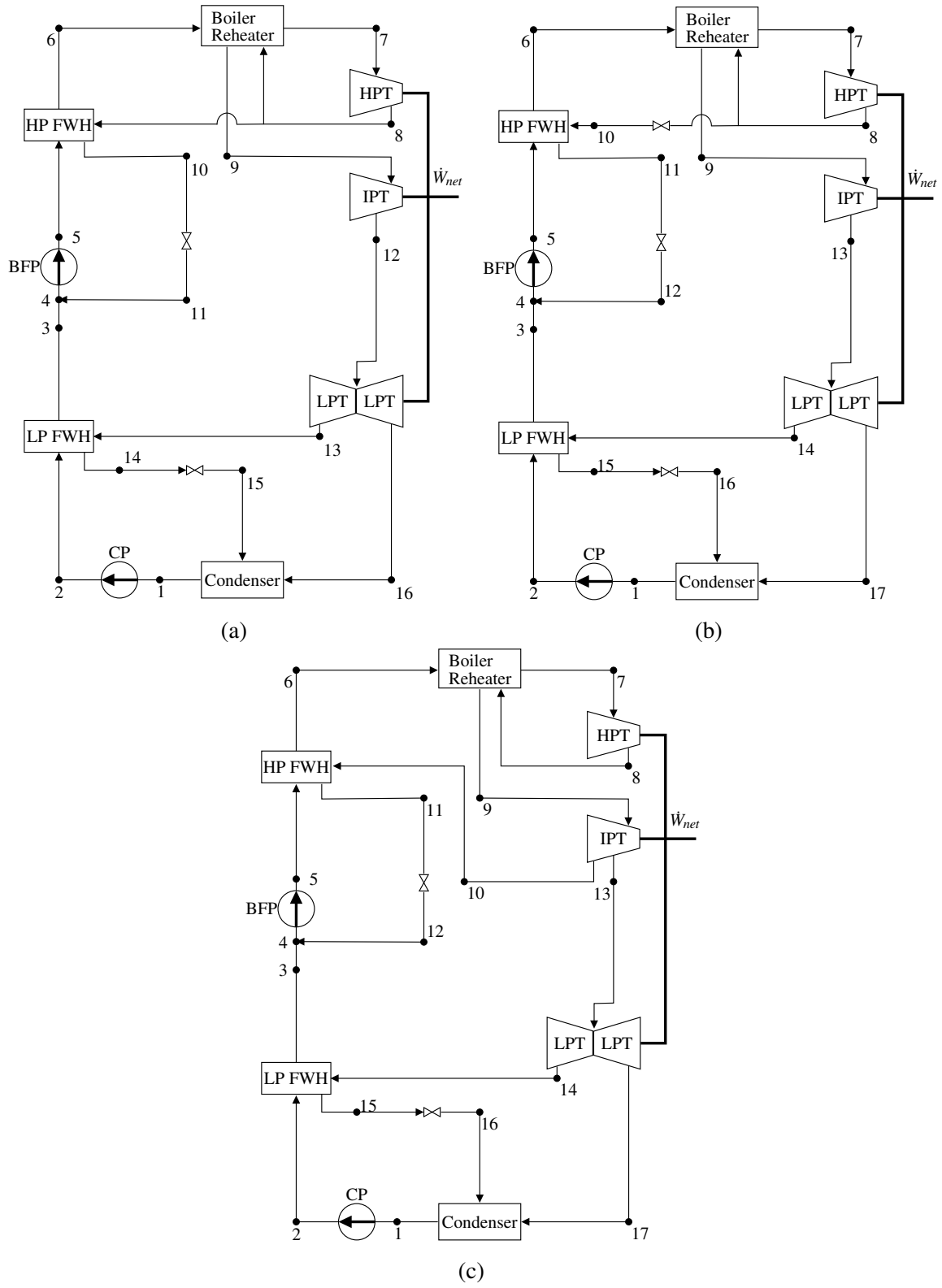


Figure C.1: Schematics for the three options considered for HP FWH extraction modeling: (a) HPT exhaust pressure, (b) throttled steam extracted from HPT exhaust, and (c) extraction from IPT.

Table C.1: Comparison of HP FWH extraction steam design options 2 and 3 to calculated performance parameters for the Hunter plant.

Data Source	\dot{W}_{net} [MW]	\dot{Q}_B [MW]	η_{th} [%]	η_{II} [%]
Hunter Plant	511	1273	40.2	45.8
Option 2	505	1276	39.6	45.1
Option 3	504	1226	41.1	46.8

C.3 Results

The remaining design options (Figures C.1b and C.1c) were simulated using the solar integration model for the Hunter Plant (Appendix H.2) assuming an augment fraction $k = 0$ and no FWH bypass. State 10 for option 2 is modeled using an isenthalpic valve to throttle the extracted HPT exhaust steam to the mass averaged pressure calculated from the plant data. For option 3, the enthalpy at state 10 is calculated using the isentropic efficiency of the IPT and the same mass averaged pressure. Results for these tests are provided in Table C.1.

Both options converged to similar accuracy for power estimates. However, option 2 stands out with superior accuracy, particularly regarding \dot{Q}_B and η_{th} .

C.4 Discussion

Plants such as the Hunter plant and the model in Adibhatla and Kaushik do not extract steam from the HPT at an intermediate pressure [28]. But there exists plants such as from Li et al. in which two extraction lines for feedwater heating come from the HPT [107].

For the schematic from Li et al. (Figure C.2), the pressure used for State 10 in the representative model (Figure 2.6 is calculated using the mass averaged approach for the two HPT extractions and the IPT extraction for H3 in Li et al. For the case where H3 is bypassed, the calculated mass averaged pressure would only consider the HPT extractions and would necessarily be greater than the inlet pressure to the IPT. This eliminates Option 3 for use in systems with multiple HPT extractions. Due to this complication and the frequency of configurations similar to Li et al., option 2 is selected to ensure this process can still be widely accessible.

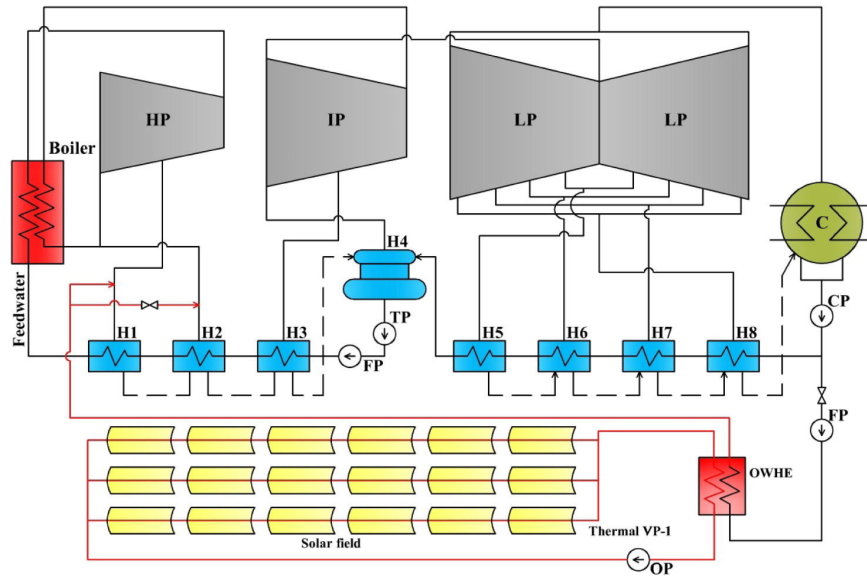


Figure C.2: CSP-coal hybrid power plant as published in Li et al. [107]. Two steam lines are extracted from the HPT for feedwater heating.

C.5 Conclusion

Option 2 has been shown to be more accurate and option 3 has been shown to be infeasible for common configurations of coal power plants. Projects with a single HPT extraction line that require greater modeling accuracy may choose to analyze their system using the approach laid out in option 3. To preserve the scope of this study, option 2 was used for the analysis in this study.

APPENDIX D. FINANCIAL PARAMETERS

D.1 Introduction

LCOE is used to compare the life-cycle costs and life-cycle energy production of the overall project [108]. LCOE calculation is accomplished by using either a discount rate and cash flow analysis, or the fixed charge rate. As will be shown below, the discount rate LCOE is a more applicable calculation method for this study. A discussion on the estimation of the capital cost and payback time is also included. To verify the methods used, this report also discusses estimations for LCOE, capital cost, and payback time for a CSP-coal hybrid plant based on the PacifiCorp Hunter Unit 3 power plant in Castle Dale, Utah.

D.2 Method

LCOE can be calculated using either a discount rate or a fixed charge rate, as discussed in Section D.2.1. Section D.2.2 describes capital cost as a combination of direct and indirect costs, and represents the investment cost of the CSP augmentation. Payback time (PBT) calculation represents the time required for the augmentation financial benefits to recover investment costs. Equations used for calculation are provided. The model for the calculations of LCOE, capital cost, and PBT is primarily based on the National Renewable Energy Laboratory (NREL) System Advisor Model (SAM) [58].

D.2.1 Methods of LCOE Calculation

LCOE represents the average revenue required to recover the costs of installing and operating a power plant for a specified project life per unit of electrical energy [109]. In general, LCOE is equal to the net cost (C_{net}) of the project scaled by the energy output (E), as shown in Equation

D.1.

$$\text{LCOE} = \frac{C_{\text{net}}}{E} \quad (\text{D.1})$$

Equation D.1 is a general calculation for LCOE but does not account for the change in value of C_{net} over time. This study focuses on two methods used to determine the LCOE; the first of which uses a discount rate and the second uses a fixed charge rate (FCR) to determine the present value of C_{net} . For clarification throughout the report, the first method will be referred to as the discount rate LCOE and the second method will be referred to as the FCR LCOE.

Discount rate LCOE requires a cash flow analysis to determine the after tax costs of the solar augmentation. The discount rate determines the present value of the annualized costs over the project life. FCR LCOE uses the FCR to determine the amount of revenue per dollar of investment cost that will need to be collected to cover the costs of the investment [110].

C_{net} for this study does not account for costs associated with the existing coal plant, rather it only accounts for the costs the associated with the CSP augmentation. The LCOE of the hybrid plant can be estimated by the sum of cost of the CSP augmentation and the cost of the existing coal plant.

Since this study uses a long term analysis, the LCOE is expressed in real dollars rather than nominal. Real refers to a constant dollar, or an inflation adjusted dollar. This is in contrast to nominal which represents a current dollar value, or a value not adjusted by inflation [58]. Equation D.2 demonstrates the process to convert real rates (r_r) to nominal rates (r_{nom}) by using the inflation rate (r_i).

$$r_{\text{nom}} = (r_i + 1) \cdot (r_r + 1) \quad (\text{D.2})$$

Discount Rate LCOE

To generate an accurate LCOE, the net cost is discounted to determine the present value of the project costs. Equation D.3 uses the nominal discount rate ($r_{d,\text{nom}}$) to determine the present value, subject to inflation, of C_{net} from the after tax costs of the project (C_{tot}) where N is the analysis period and n represents the current year. Note that $n = 0$ represents the initial project investment.

$$C_{\text{net}} = \sum_{n=0}^N \frac{C_n}{(1 + r_{d,\text{nom}})^n} \quad (\text{D.3})$$

Discount LCOE is similar to Equation D.1, however Equation D.4 shows that along with the levelized C_{net} the real discount rate ($r_{d,r}$) is applied. Although it appears that E is discounted, the LCOE is actually the value being discounted. This allows for the money value of the energy load to be considered at a present day value.

$$\text{LCOE} = \frac{C_{\text{net}}}{\sum_{n=1}^N \frac{E_n}{(1+r_r)^n}} \quad (\text{D.4})$$

An annualized cash flow analysis is used to determine the variance in C_n over the project life. The procedure to determine C_n can be separated into four categories: operating expenses, loan payments, tax credits, and income tax. All formulas for the cash flow analysis, with the exception of loan payment, were taken from the SAM financial model [58].

Operating and Maintenance Expenses

Annual operation and maintenance (O&M) expenses (C_{tot}) include fixed (C_{FOM}) and variable (C_{VOM}) O&M costs, insurance (C_{ins}), and property tax ($C_{t,\text{prp}}$). The total expenses for each year are the sum of the previously mentioned cost values as shown in Equation D.5.

$$C_{\text{tot}} = C_{\text{FOM}} + C_{\text{VOM}} + C_{\text{ins}} + C_{t,\text{prp}} \quad (\text{D.5})$$

Loan Payments

Annual loan payments are a constant yearly payment that are equal to the sum of the debt interest and the principle payment. Equation D.6 calculates the principle and interest payment ($C_{P\&I}$) from the loan rate (r_{int}), initial loan balance ($L_{\text{net},0}$), and loan period (N_L) [111].

$$C_{P\&I} = \frac{r_{\text{int}} \cdot L_{\text{net},0}}{1 - (1 + r_{\text{int}})^{N_L}} \quad (\text{D.6})$$

Tax Credits

Tax credits are an important variable when considering renewable energy sources. This study focuses primarily on the federal Investment Tax Credit (ITC) and Project Tax Credit (PTC). Other incentives used in the SAM financial model but are not included in this study are: Investment based

incentives, capacity based incentives, and production based incentives [58]. These incentives were omitted because there is not recent history of them being applicable for CSP in the United States.

ITC is a percentage of the investment for solar energy equipment, and is included in the tax refund for the year the investment was made. Equation D.7 shows the calculation of the ITC based off of the capital cost and the ITC rate (r_{ITC}).

$$ITC = CC \cdot r_{ITC} \quad (D.7)$$

The PTC is less relevant for this study since the Consolidated Appropriations Act of 2016 terminated the federal PTC for solar power generation [112]. However, Equation D.8 demonstrates how to calculate the federal PTC, in the case that it is reinstated or if a similar program is applicable in other countries, by using the PTC rate (r_{PTC}), the electrical capacity of the solar augmentation (\dot{W}_s) and the amount of sunlight hours in a year ($365 h_{sun}$), where h_{sun} is the multi-year average daily sunlight hours [hrs day^{-1}]. The PTC is only applied throughout a government specified term.

$$PTC_n = \dot{W}_s \cdot 365 h_{sun} \cdot r_{PTC} \quad (D.8)$$

ITC is included in the income tax savings during the first year of the project. PTC is included in the income tax savings during the duration of time specified by the applicable tax law.

Income Tax

Once the operating expenses, loan payment, and tax credits have been determined, it is then possible to calculate the federal and state income taxes. The calculation for both the federal and the state income taxes are almost identical, however, the state income tax is calculated before the federal income tax so that the state tax will be considered when calculating federal deductions.

Income taxes, including income tax savings (S_t), are based on state and federal income tax rates, depreciation schedule, taxable income, operating expenses, interest payments, and applicable tax credits. Calculations for S_t are more thoroughly expressed in the MATLAB code included in Appendix H and were pulled from SAM [58]; however, equation D.9 shows that in general, it consists of the sum of ITC, PTC, and federal ($S_{t,Fed}$) and state ($S_{t,st}$) income tax savings.

$$S_t = S_{t,Fed} + S_{t,st} + ITC + PTC \quad (D.9)$$

After Tax Costs

After calculating the operating expenses, loan payment, tax credits, and income taxes, C_{tot} can then be determined for each year as shown in Equation D.10.

$$C_{\text{tot}} = C_{\text{tot}} + C_{P\&I} - S_t \quad (\text{D.10})$$

Input values used to calculate the costs of the project vary depending on the location and the scale of the project. Default values used in these equations are provided in Table 2.6.

Fixed Charge Rate LCOE

When financing is neglected and energy output and O&M costs are assumed to be constant, the LCOE can be estimated by using the FCR. The FCR is used to estimate the average annual cost of capital. The benefit to using the FCR method is that it allows for the LCOE to be estimated from first year inputs without the need for a complete cash flow analysis. This eliminates the possibility of estimating PBT which is further discussed in Section D.2.2. Equation D.11 estimates the LCOE by multiplying the FCR by the capital cost (CC). The product of the FCR and CC is added to the average annual cost which is all scaled by the first year energy output (E_0).

$$\text{LCOE} = \frac{\text{FCR} \cdot \text{CC} + C_{\text{FOM},0}}{E_0} + r_{\text{VOM}} \quad (\text{D.11})$$

There are two assumptions involved in Equation D.11 that cause it to differ from the discount LCOE. Since E_0 is used instead of a discounted E , the future energy output is not scaled back to match its present money value. The second flaw with Equation D.11 is that C_{FOM} is not inflated throughout the project life which again does not allow an accurate assessment of the project present value for long term projects.

FCR is a combination of the capital recover factor (CRF), project factor (PFF), and construction factor (CFF) as shown in Equation D.12. CRF is the fraction of the capital cost that will account for annual loan payment [110]. PFF accounts for the project financing costs such as taxes

and depreciation. CFF accounts for the construction costs of the project.

$$\text{FCR} = \text{CRF} \cdot \text{PFF} \cdot \text{CFF} \quad (\text{D.12})$$

The methods used to determine CRF, PFF, and CFF are mapped out in Equations D.13 through D.19. The effective tax rate ($r_{t,e}$) and weighted average cost of capital (WACC) are both needed for determining CRF, PFF, and CFF, and are calculated in Equations D.13 through D.16. The $r_{t,e}$ accounts for both state ($r_{t,st}$) and federal ($r_{t,Fed}$) income tax rates as shown in Equation D.13.

$$r_{t,e} = r_{t,st} + r_{t,Fed} \cdot (1 - r_{t,st}) \quad (\text{D.13})$$

WACC is a weighted average of the component costs of debt, preferred stock, and common equity [110]. Equations D.14, D.15, and D.16 use the debt fraction (F_L), effective tax rate, internal rate of return (IRR), nominal interest rate (r_{int}), and inflation rate (r_i) to determine the WACC. r_{int} and IRR are converted from nominal to real, ($r_{int,r}$) and (IRR_r), respectively in Equations D.16 and D.15.

$$\begin{aligned} \text{WACC} = & \frac{1 + ((1 - F_L) \cdot ((1 + \text{IRR}_r) \cdot (1 + r_i) - 1))}{1 + r_i} \\ & + \frac{F_L \cdot ((1 + r_{int,r}) \cdot (1 + r_i) - 1) \cdot (1 - r_{t,e})}{1 + r_i} - 1 \end{aligned} \quad (\text{D.14})$$

Where,

$$\text{IRR}_r = \frac{1 + \text{IRR}}{1 + r_i} - r_i \quad (\text{D.15})$$

$$r_{int,r} = \frac{1 + r_{int}}{1 + r_i} - r_i \quad (\text{D.16})$$

Once the WACC and effective tax rate are determined, Equations D.17 and D.18 are used to determine the CRF and PFF. While Equation D.17 only uses the WACC and N, Equation D.18 also includes the depreciation schedule (SC_{dep}) and $r_{t,e}$.

$$\text{CRF} = \frac{\text{WACC}(1 + \text{WACC})^N}{(1 + \text{WACC})^N - 1} \quad (\text{D.17})$$

$$\text{PFF} = \frac{1 - (r_{t,e} \cdot \left(\sum_{n=0}^N \frac{\text{SC}_{\text{dep},n}}{(1+\text{WACC}) \cdot (1+r_i)^{n+1}} \right))}{1 - r_{t,e}} \quad (\text{D.18})$$

Equation D.19 is used to determine the CFF from the construction cost schedule (SC_{con}), $r_{t,e}$, nominal construction financing interest rate (r_{con}), and construction period in years (N_{con}).

$$\text{CFF} = \sum_{n=0}^{N_{\text{con}}} \text{SC}_{\text{con},n} \cdot (1 + (1 - r_{t,e}) \cdot ((1 + r_{\text{con}})^{n+\frac{1}{2}} - 1)) \quad (\text{D.19})$$

CRF, PFF, and CFF were estimated from the inputs provided in Table D.1 with the exception of FOC and VOC. The values in Table D.1 were taken from the default values used in SAM.

Table D.1: Default values for FCR LCOE excluded in Table 2.6

Default Input	Value	Source
IRR [%/year]	13	[113]
SC_{con}^* [%/year]	80 10 10	[58]
r_{con} [%/year]	8	[58]

*The construction cost schedule is a vector of percentages of the capital cost that are used during each year of the construction of the solar augmentation. This study assumes a three year construction period.

D.2.2 Model and Input Adjustments for Hybridization

SAM was developed to analyze standalone CSP projects. This section will discuss some of the changes required to allow for the methods used in SAM to be applied to a coal power plant augmented with solar-thermal energy. The areas that require adjustments include capital cost, O&M costs, and energy output.

Calculation of the Capital Cost

Total capital costs are a combination of direct and indirect costs. The process of calculating direct, indirect, and capital costs are included in Tables D.2 and 2.6. Both tables show methods and

values provided by SAM [58] and Adibhatla and Kaushik [114]. Some of the direct costs needed to install a parabolic trough system are based on the total aperture area of the troughs (Section 2.2).

Table D.2: Methods used to calculate the capital cost.

Cost item	Variable	Calculation method [USD]
Direct Costs (C_{DC})		
Site improvements	C_{SI}^*	$C_{SI} = F_{SI}A_p$
Solar field	C_{SF}^\dagger	$C_{SF} = F_{SF} \cdot A_p$
HTF system	C_{HTF}^\ddagger	$C_{HTF} = F_{HTF} \cdot A_p$
Heat exchanger	C_{HX}^\S	$C_{HX} = F_{HX} \cdot 1000000$
Contingency	C_{cont}	$C_{cont} = r_{cont}(C_{SI} + C_{SF} + C_{HTF} + C_{HX})$
Total direct costs	C_{DC}	$C_{DC} = C_{SI} + C_{SF} + C_{HTF} + C_{HX} + C_{cont}$
Indirect Costs (C_{IC})		
EPC and owner costs	C_{EPC}	$C_{EPC} = r_{EPC} \cdot C_{DC}$
Sales tax	$C_{t,sal}$	$C_{t,sal} = r_{t,sal} \cdot F_{t,sal} \cdot C_{DC}$
Total indirect costs	C_{IC}	$C_{IC} = C_{EPC} + C_{t,sal}$
Total Capital Cost	CC	$CC = C_{DC} + C_{IC}$

* C_{SI} : Costs for site preparation and other expenses not included in the solar field.

† C_{SF} : Costs related to the installation and purchase of parts related to the solar field.

‡ C_{HTF} : Costs accounting for installation of pumps and piping of HTF system, including labor and equipment.

§ C_{HX} : Costs accounting for the installation and purchase of a heat exchanger.

O&M Costs

For a standalone CSP plant, first year O&M costs $C_{FOM,0}$ and $C_{VOM,0}$ would be calculated using the capacity of the power block and the energy load as shown in Equations D.20 and D.21.

$$C_{FOM,0} = F_{FOM} \cdot \dot{W}_{net} \quad (D.20)$$

$$C_{FOM,0} = F_{VOM} \cdot E \quad (D.21)$$

For a hybrid power plant, the capacity and energy output used to calculate $C_{\text{FOM},0}$ and $C_{\text{VOM},0}$ for the solar augmentation are based on \dot{W}_s . To determine the $C_{\text{FOM},0}$ and $C_{\text{VOM},0}$ for the CSP portion of the power plant, E and \dot{W}_{net} need to be adjusted to represent the portion of the energy load and capacity that can be attributed to the solar augmentation (Equations D.22 and D.23).

$$C_{\text{FOM},0} = F_{\text{FOM}} \cdot \dot{W}_s \quad (\text{D.22})$$

$$C_{\text{VOM},0} = F_{\text{VOM}} \dot{W}_s h_{\text{sun}} 365 \quad (\text{D.23})$$

Calculation of Simple Payback Time

While LCOE provides important information on the cost of solar and coal hybridization, it does not provide information on the amount of time it would take to recover the costs. PBT gives further insight by reporting the time needed to recover associated costs. The definition of PBT can vary depending on the parameters that are considered and this report focuses on two definitions.

The first definition of PBT (PBT1) is the number of years required for the cumulative fuel savings (S_{an}) to equal the cumulative annual costs (C_{an}) (Equation D.24). S_{an} and C_{an} are calculated by determining the cumulative annual cash flow (A_{an}) including the capital costs.

$$A_{\text{an}} = S_{\text{an}} - C_{\text{an}} \quad (\text{D.24})$$

Equation D.24 is repeated for each year of the project until A_{an} is equal to 0. The year A_{an} is equal to 0 is the projected PBT. It is important to note that A_{an} includes the capital costs and neglects the loan payment because this method focuses only on the time required to recover the initial investment [115].

The second definition of PBT (PBT2) is the time needed for the cumulative fuel savings to equal the initial investment [115]. Equation D.25 shows that fuel savings (FS) are determined by converting the fuel offset power (\dot{Q}_{fo}), applicable only for the time the plant is operating in hybrid mode (h_{sun}), to the cost of its equivalent coal mass by using the cost (F_F), at 36.3 USD/sh.

tn. [116], and heating value (LHV_F) of coal, at 23.9 MJ/kg [117].

$$FS = \frac{365 h_{\text{sun}} \cdot \dot{Q}_{\text{fo}} \cdot F_F}{LHV_F} \quad (\text{D.25})$$

This study only calculates fuel savings as revenue generated from the project, however some countries implement a carbon tax which, if applicable, would contribute to recovering the costs of the project. To implement a carbon tax, the tax would be added to the fuel savings. Equation D.26 demonstrates a simple example of how to calculate carbon tax savings (S_{t,CO_2}) by using a tax rate (r_{t,CO_2}), E_{sav} , the CO_2 to coal mass conversion ratio (F_{cc}), and LHV_F .

$$S_{t,\text{CO}_2} = \frac{r_{t,\text{CO}_2} \cdot F_{cc} \cdot E_{\text{sav}}}{HV_F} \quad (\text{D.26})$$

Duffie and Beckman [115] provided a method to calculate PBT2 (Equation D.27) which uses the inflation rate and the capital cost.

$$\text{PBT2} = \frac{\ln\left[\frac{CC \cdot r_i}{FS}\right] + 1}{\ln(1 + r_i)} \quad (\text{D.27})$$

D.3 Results

Actual data for capital costs of CSP power plants is provided by CSP Guru in connection with SolarPACES [118]. Figure D.1 shows the comparison between the capital costs of actual power plants and the capital costs estimated using the financial model of this study. The difference between the values calculated using the financial model and the CSP Guru trend are likely attributed to the inclusion of all CSP technologies (PTC, LFR, Dish, and Tower) as well as the price of equipment not considered in the financial model such as turbines, pump for the power block, and a condenser.

Table D.3 was produced using the methods described for calculating LCOE, capital cost, PBT1, and PBT2, along with the determined input values (Table 2.6). The model is designed to iterate based on changes in the net capacity of the power block (\dot{W}_{net}), and the required receiver area (A_r). Also included in Table D.3 is the number of the feedwater heater (FWH) that is bypassed and

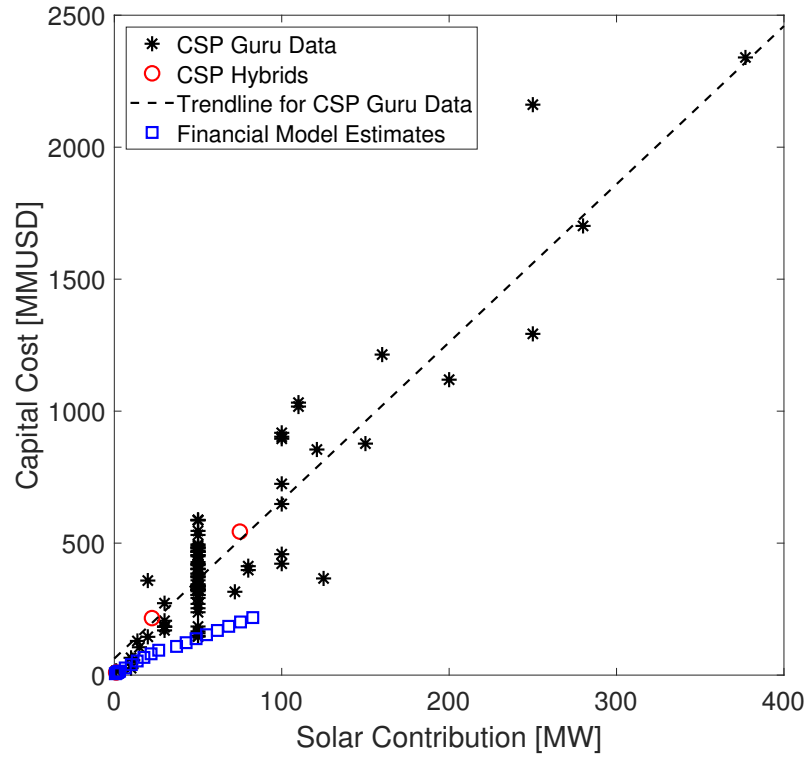


Figure D.1: Comparison of capital cost data and calculated capital costs from financial model.

k . The range for k is 1%, 5%, and the equivalent fraction of that FWH at full operating conditions (typically 2-3%).

Table D.3: Calculated values for Capital Cost (CC), LCOE, and payback time (PBT).

FWH #	k [%]	A_r [10^3 m^2]	A_{sf} [ac]	CC [MMUSD]	Discount Rate [$10^{-4} \text{ USD kWh}^{-1}$]	LCOE [$10^{-4} \text{ USD kWh}^{-1}$]	FCR LCOE [$10^{-4} \text{ USD kWh}^{-1}$]	PBT1 [years]	PBT2 [years]
5	3	6.4	92.1	39.9	4.48	7.6	200	N/A	
	6	13.3	194.2	80.7	9.11	15	146.4	41.2	
	10	23.1	337.9	138	16	26	68.35	30	
6	3	6.4	92.1	39.9	4.48	7.62	200	N/A	
	6	13.3	194.2	80.7	9.12	15	91.5	36.2	
	10	23.1	337.9	138	16	26	59.9	28.2	
7	3	6.4	92.1	39.9	4.5	7.62	200	N/A	
	6	13.3	194.2	80.7	9.21	15	90.2	35.2	
	10	23.1	337.9	138	16	26	61.9	29.5	

D.4 Conclusion

Table D.3 demonstrates that the FWH primarily affects the performance of the CSP augmentation, and k is what primarily affects the LCOE.

The difference in the discount rate and FCR methods for calculating the LCOE are also important to note. The Discount Rate LCOE varies less than the FCR LCOE and is consistently separated by about 90%. It is also important to note that the LCOE doesn't significantly change for each test. This is most likely a result of scaling by the total energy output of the coal plant which is very large in comparison to the thermal energy of the CSP.

When comparing the LCOE from the discount rate method and the FCR method, the discount rate is considered to be more applicable for this study. In addition to providing a cash flow analysis useful in calculating PBT, discount rate LCOE allows for the present value of future costs to be considered more accurately. FCR however is less applicable because constant annual costs is a poor assumption, and future cash flow is not levelized.

APPENDIX E. NSRDB DATA

Table E.1: 6/25/2018 Meteorological data for Castle Dale, UT.
Downloaded from NSRDB [46]

Hour	Minute	DNI [W m ⁻²]	CSDNI [W m ⁻²]	θ_z [degrees]	Temperature [°C]	Pressure [mbar]
0	0	0	0	117.13	15.2	830
0	30	0	0	117.43	14.8	830
1	0	0	0	116.96	14.5	830
1	30	0	0	115.71	14.1	830
2	0	0	0	113.74	13.8	830
2	30	0	0	111.12	13.5	830
3	0	0	0	107.91	13.1	830
3	30	0	0	104.19	12.8	830
4	0	0	0	100.04	12.5	830
4	30	0	0	95.52	12.9	830
5	0	56	56	90.21	13.2	830
5	30	376	376	85.47	15.4	830
6	0	592	592	80.26	17.6	831
6	30	720	720	74.83	19.7	831
7	0	803	803	69.26	21.8	831
7	30	860	860	63.57	23.4	831

8	0	899	899	57.82	25	831
8	30	928	928	52.02	26.1	831
9	0	951	951	46.21	27.3	831
9	30	970	970	40.45	28.3	831
10	0	985	985	34.78	29.3	831
10	30	999	999	29.32	30.2	831
11	0	1012	1012	24.24	31	831
11	30	1017	1017	19.87	31.7	830
12	0	1020	1020	16.8	32.3	830
12	30	1021	1021	15.82	32.7	830
13	0	1017	1017	17.31	33.1	830
13	30	1012	1012	20.73	33.3	830
14	0	1006	1006	25.3	33.4	830
14	30	998	998	30.48	33.3	830
15	0	986	986	36	33.2	829
15	30	970	970	41.69	32.8	829
16	0	949	949	47.47	32.5	829
16	30	923	923	53.28	32.5	829
17	0	887	887	59.08	31.3	829
17	30	838	838	64.82	30.3	829
18	0	772	772	70.48	29.3	829
18	30	676	676	76.03	26.8	830
19	0	526	526	81.42	24.4	830
19	30	285	285	86.58	23.6	830

20	0	18	18	91.78	22.9	830
20	30	0	0	96.54	22.7	830
21	0	0	0	100.99	22.6	830
21	30	0	0	105.05	22.6	830
22	0	0	0	108.67	22.6	830
22	30	0	0	111.76	22.3	830
23	0	0	0	114.25	22	830
23	30	0	0	116.07	21.3	830

APPENDIX F. CORRELATIONS

Boiler Inlet Pressure

$$P_6 = 2.9985P_{s1}^{0.548} + 7.6221 \tag{F.1}$$

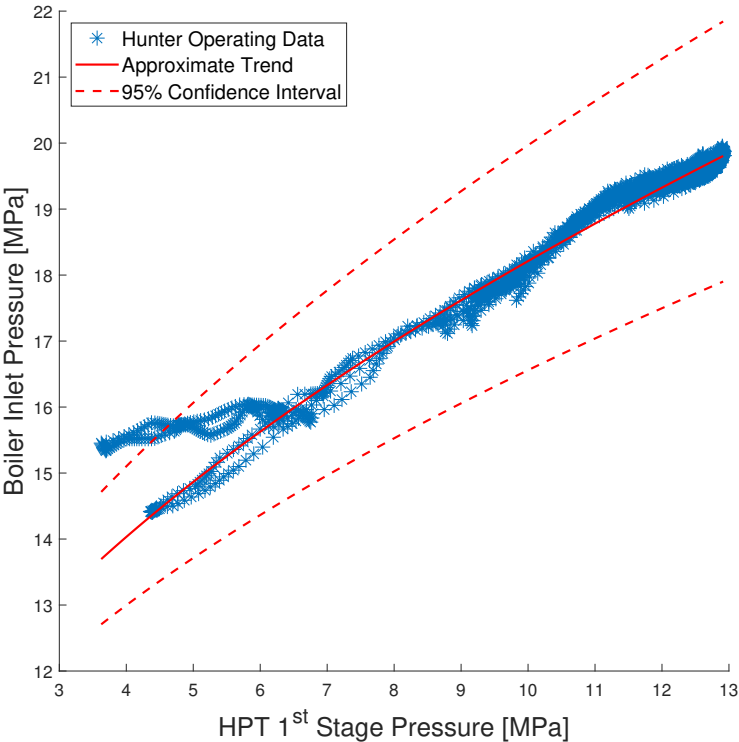


Figure F.1: Boiler inlet pressure data and correlation to HPT 1st stage pressure.

Main Steam Pressure

$$P_7 = 10.7684P_{s1}^{0.1739} \quad (\text{F.2})$$

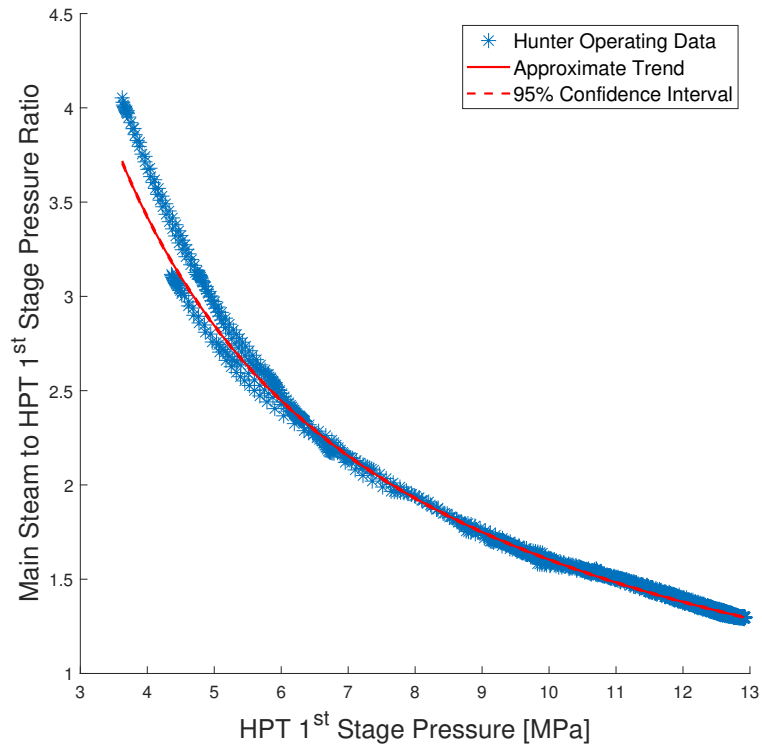


Figure F.2: Main steam pressure data and correlation to HPT 1st stage pressure.

FWH 6 Pressure ratio

$$r_{FWH6} = \frac{P_{HPT,ex}}{P_{FWH6}} = 1.8155 \quad (F.3)$$

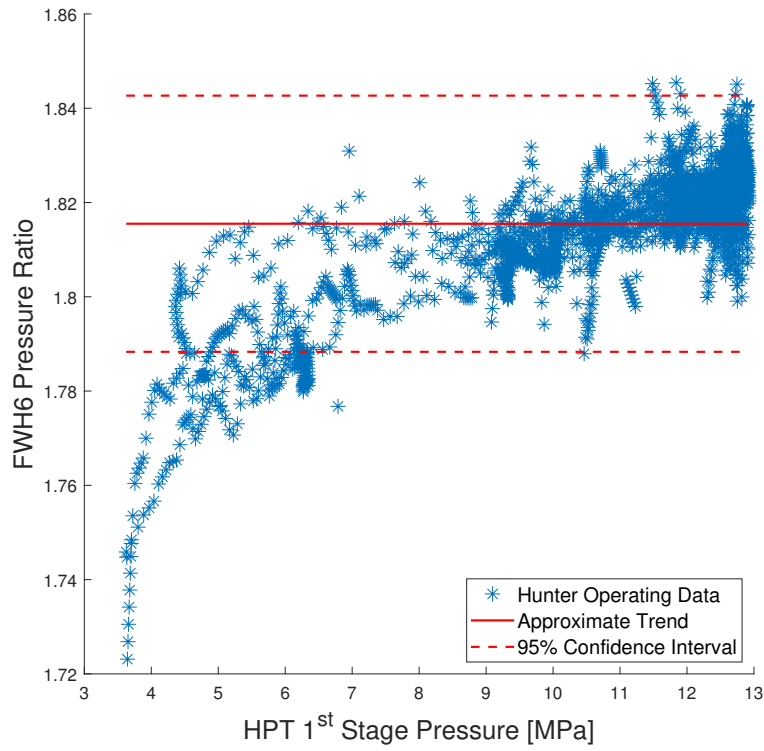


Figure F.3: FWH 6 data and constant average value

FWH 5 Pressure ratio

$$r_{FWH5} = \frac{P_{HPT,ex}}{P_{FWH5}} = -0.7076P_{s1}^{-0.8261} + 2.638 \quad (F.4)$$

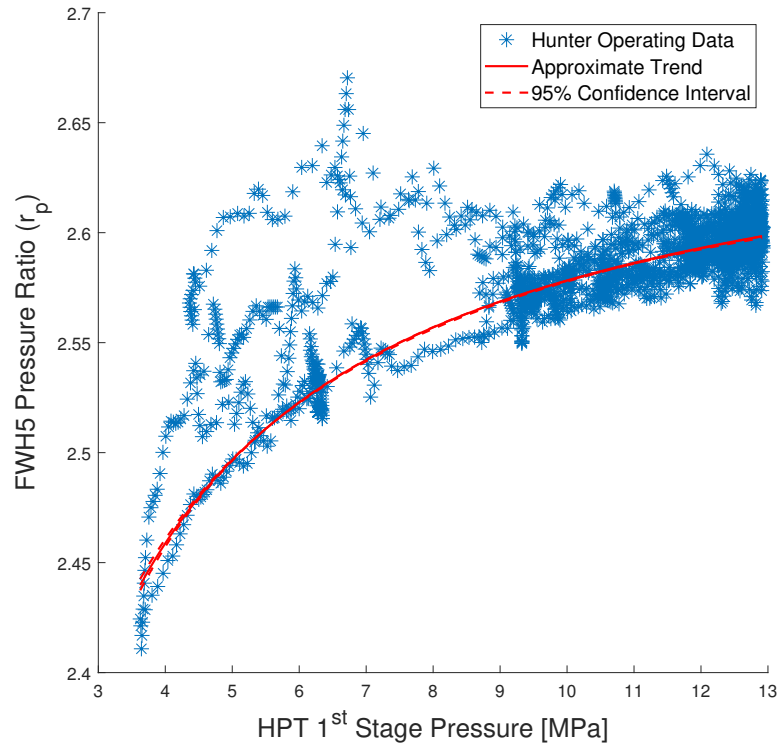


Figure F.4: FWH 5 pressure ratio data and correlation to HPT 1st stage pressure.

IPT Pressure Ratio

$$r_{\text{IPT}} = \frac{P_{\text{HPT},ex}}{P_{\text{IPT},ex}} = 2.586 \quad (\text{F.5})$$

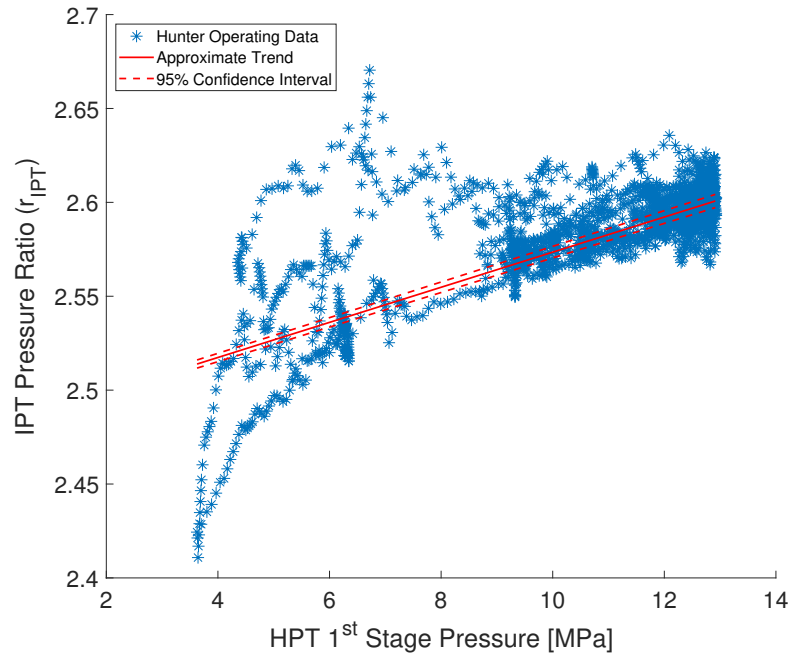


Figure F.5: IPT pressure ratio data and correlation to HPT 1st stage pressure.

DA Pressure Ratio

$$r_{\text{DA}} = \frac{P_{\text{IPT},ex}}{P_{\text{DA}}} = 49.7939P_{s1}^{-3.4562} + 2.2131 \quad (\text{F.6})$$

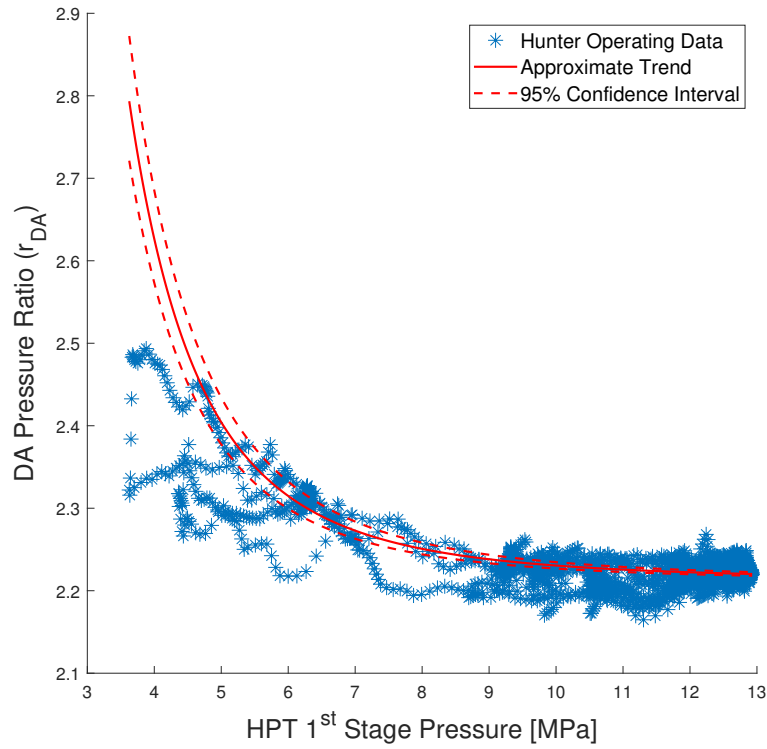


Figure F.6: DA pressure ratio data and correlation to HPT 1st stage pressure.

FWH 3 Pressure Ratio

$$r_{\text{FWH3}} = \frac{P_{\text{IPT},ex}}{P_{\text{FWH3}}} = 5.7824 \quad (\text{F.7})$$

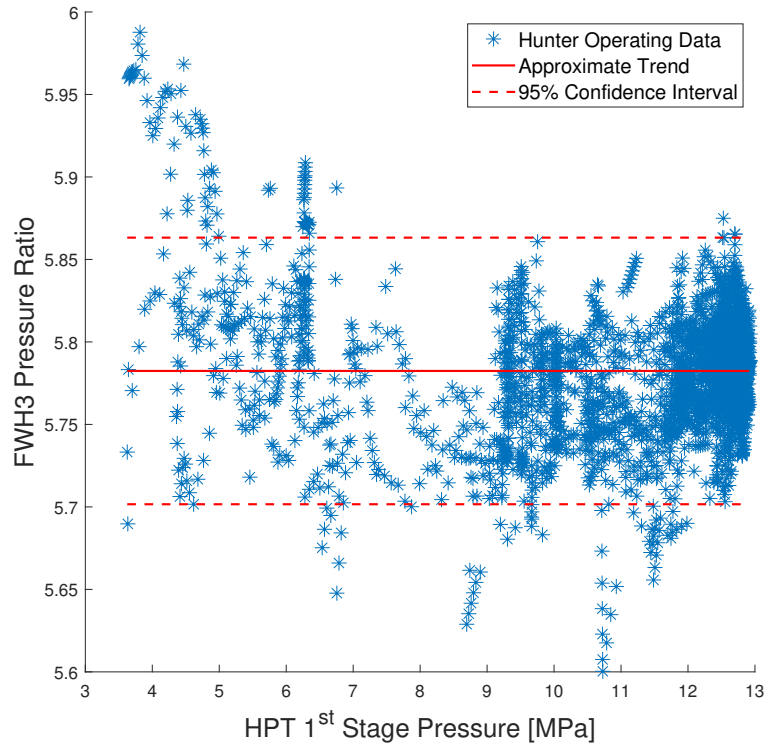
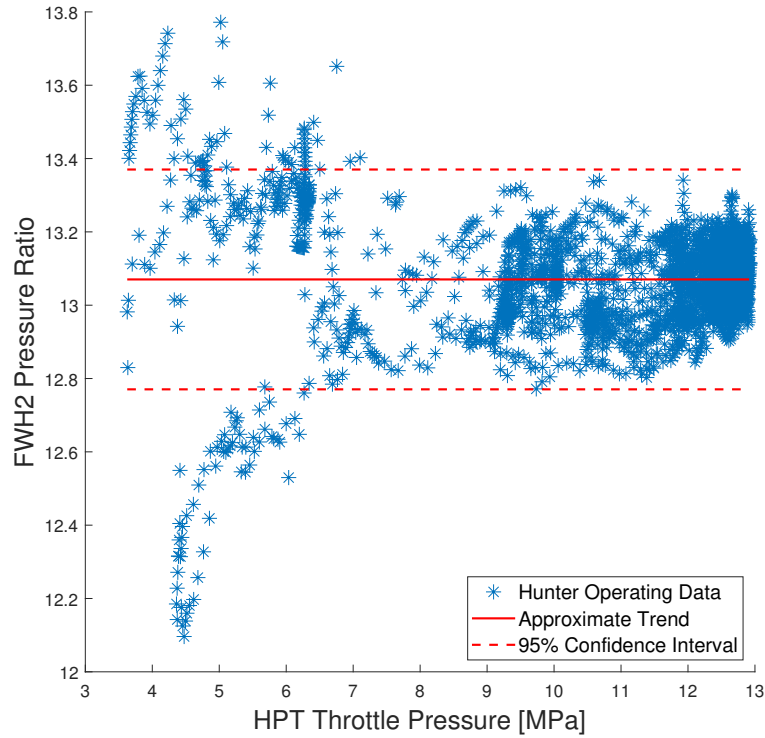


Figure F.7: FWH 3 pressure ratio data and correlation to HPT 1st stage pressure.

FWH 2 Pressure Ratio

$$r_{\text{FWH2}} = \frac{P_{\text{IPT},ex}}{P_{\text{FWH2}}} = 13.0703 \quad (\text{F.8})$$



LPT Pressure Ratio

$$r_{\text{LPT}} = \frac{P_{\text{IPT},ex}}{P_{\text{LPT},ex}} = \begin{cases} 7.9169P_{s1} + 14.8199 & P_{s1} \leq 6\text{MPa} \\ 62.65 & P_{s1} > 6\text{MPa} \end{cases} \quad (\text{F.9})$$

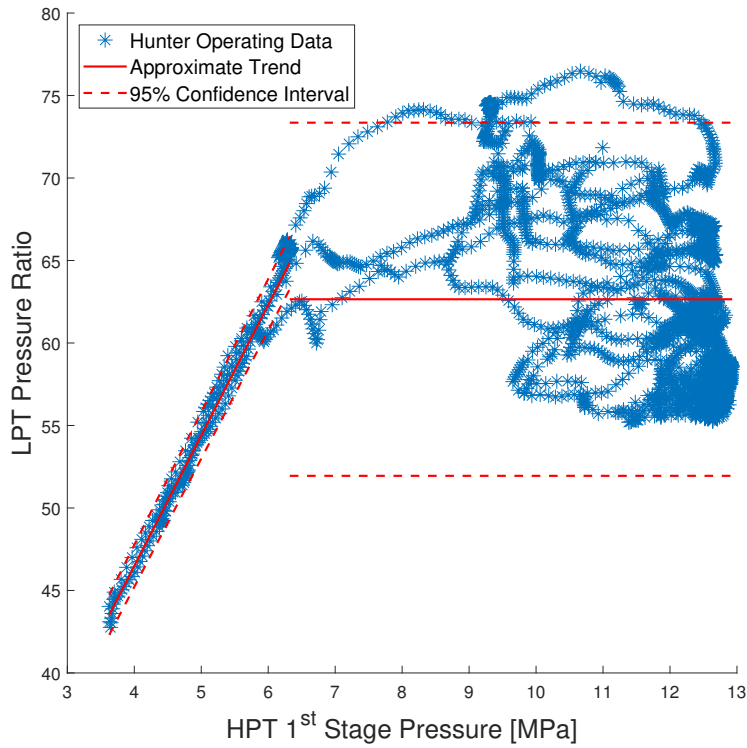


Figure F.9: LPT pressure ratio data and correlation to HPT 1st stage pressure.

Boiler Inlet Mass Flow Rate

$$\dot{m}_6 = 31.3897P_{s1} + 0.75 \quad (\text{F.10})$$

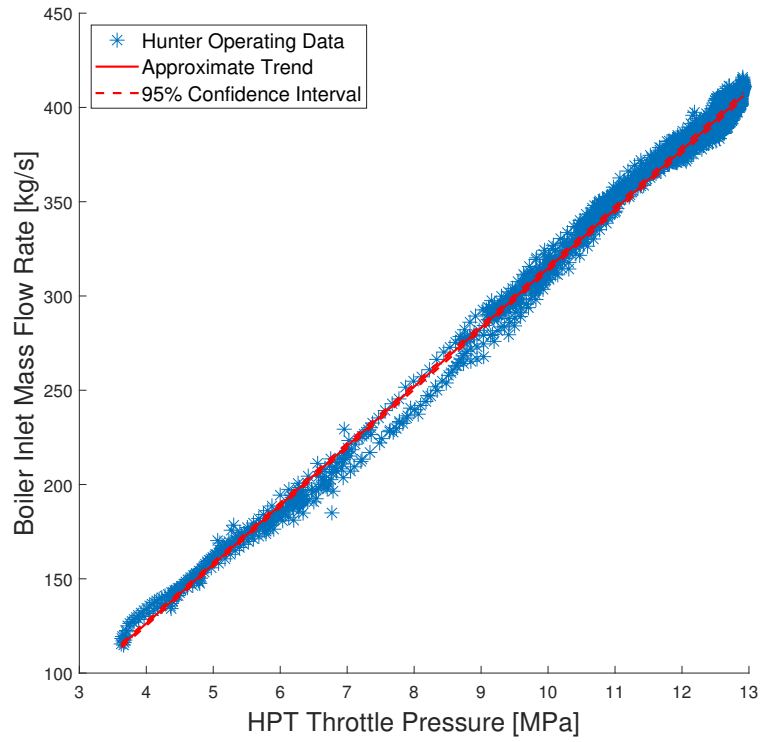


Figure F.10: Boiler inlet mass flow rate data and correlation with respect to HPT 1st stage pressure.

DA Inlet Flow Rate

$$\dot{m}_{\text{DA}} = 25.5728P_{s1} - 2.7841 \quad (\text{F.11})$$

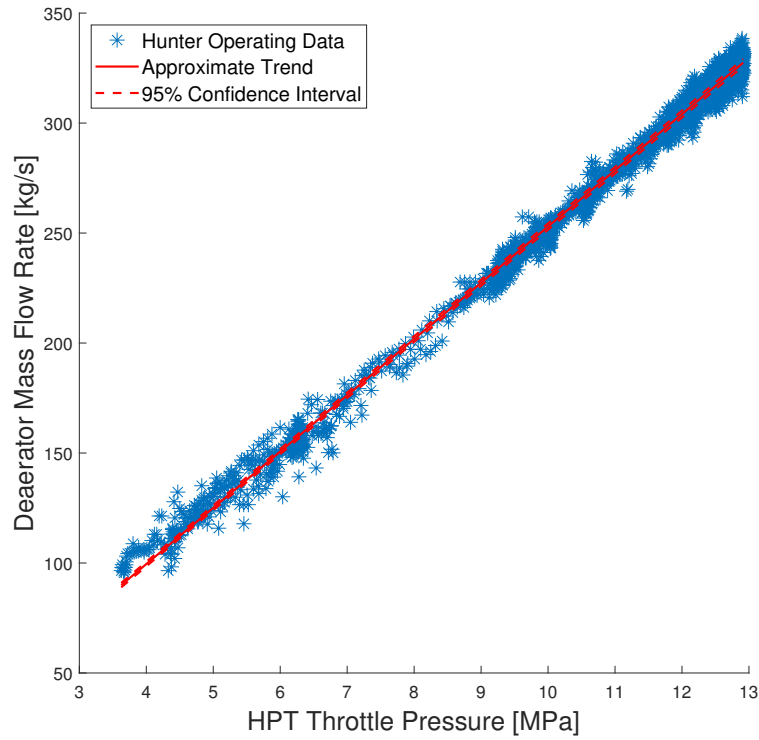


Figure F.11: DA inlet mass flow rate data and correlation with respect to HPT 1st stage pressure.

Table F.1: Correlation property equations for use in the representative model. Properties generally follow a power law relationship ($\mathcal{P} = aP_{s1}^b + c$) where P_{s1} is in MPa. Constant properties are shown where $a = b = 0$.

Property (\mathcal{P})	P_6 [MPa]	r_{HPT}	r_{FWH6}	r_{FWH5}	r_{IPT}	r_{DA}	r_{FWH3}	r_{FWH2}	r_{LPT}	\dot{m}_6 [kg s ⁻¹]	\dot{m}_{DA} [kg s ⁻¹]	T_B [K]	P_{cond} [MPa]	η_{HPT} [%]	η_{IPT} [%]	η_{LPT} [%]	
a	2.9985	10.7684	0	-0.7076	0	49.7939	0	0	0	31.3897	25.5728	0	0	0	0	0	0
b	0.548	0.1739	0	-0.8261	0	-3.4562	0	0	0	1	1	0	0	0	0	0	0
c	7.6221	0	1.8155	2.6838	2.5860	2.2131	5.7824	13.0703	62.65	0.75	-2.7841	811.8	8.1e-3	89.4	91.7	91.8	91.8

APPENDIX G. SOLAR INTEGRATION CONFIGURATIONS AND SUBSYSTEMS

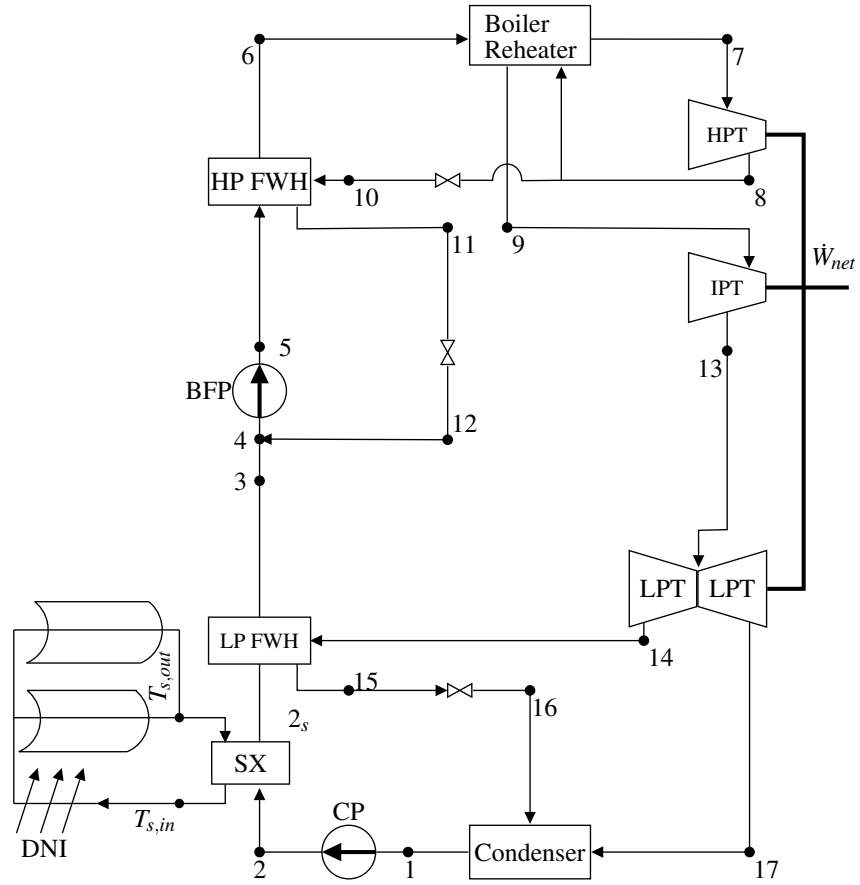


Figure G.1: FWH 1 or FWH 2 bypass solar integration configuration.

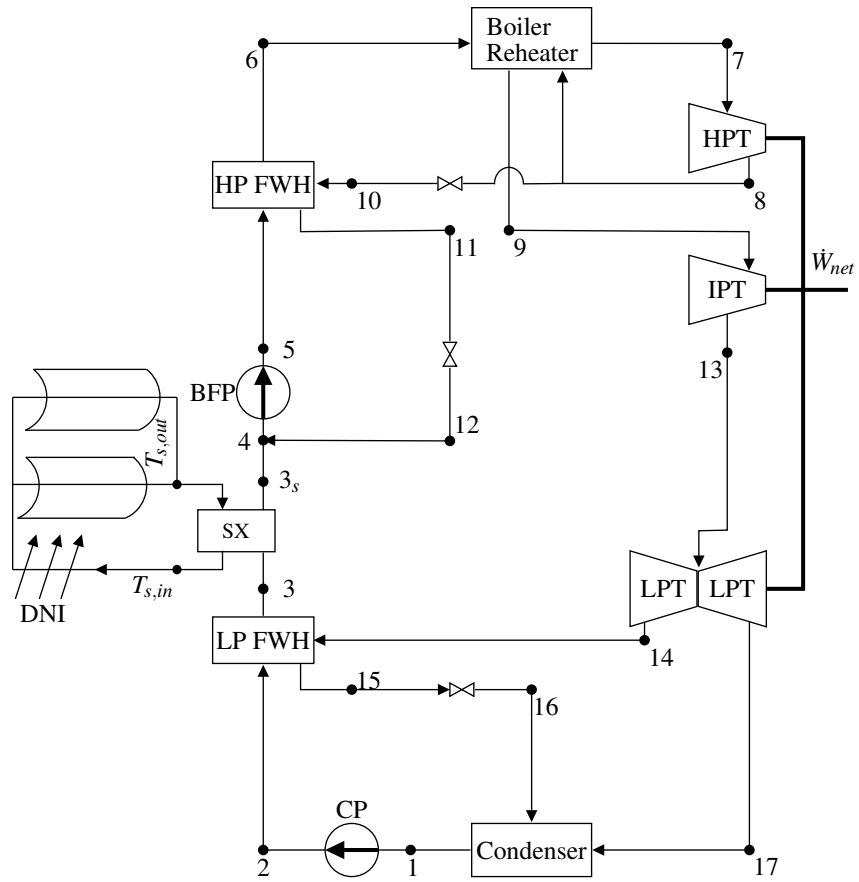


Figure G.2: FWH 3 bypass solar integration configuration.

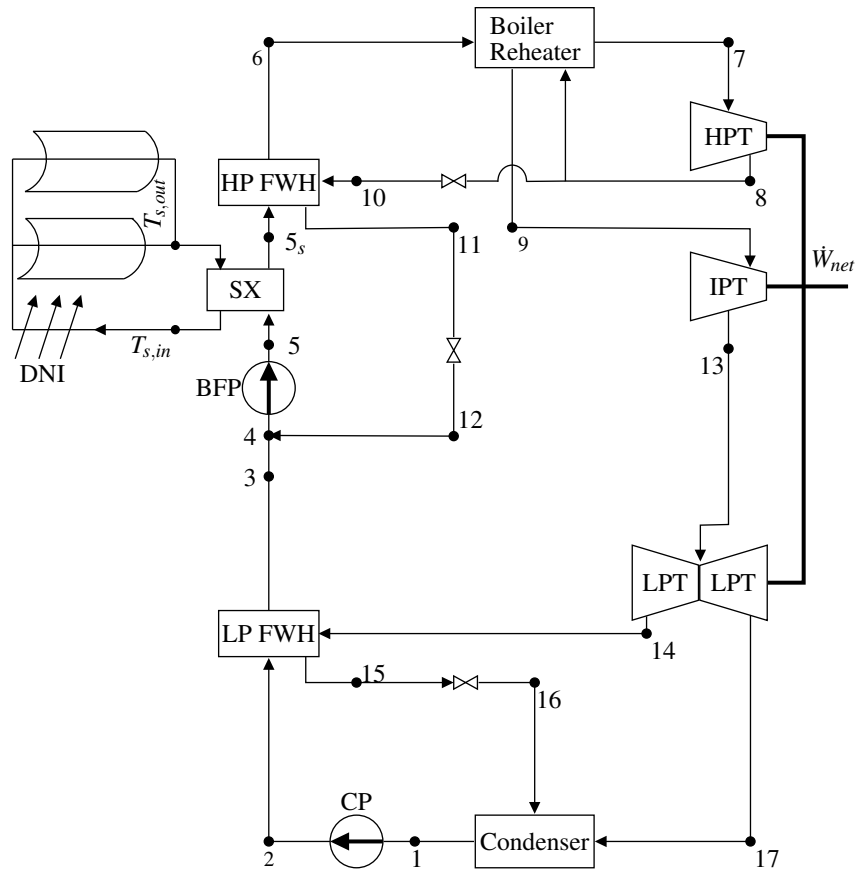


Figure G.3: FWH 5 or FWH 6 bypass solar integration configuration.

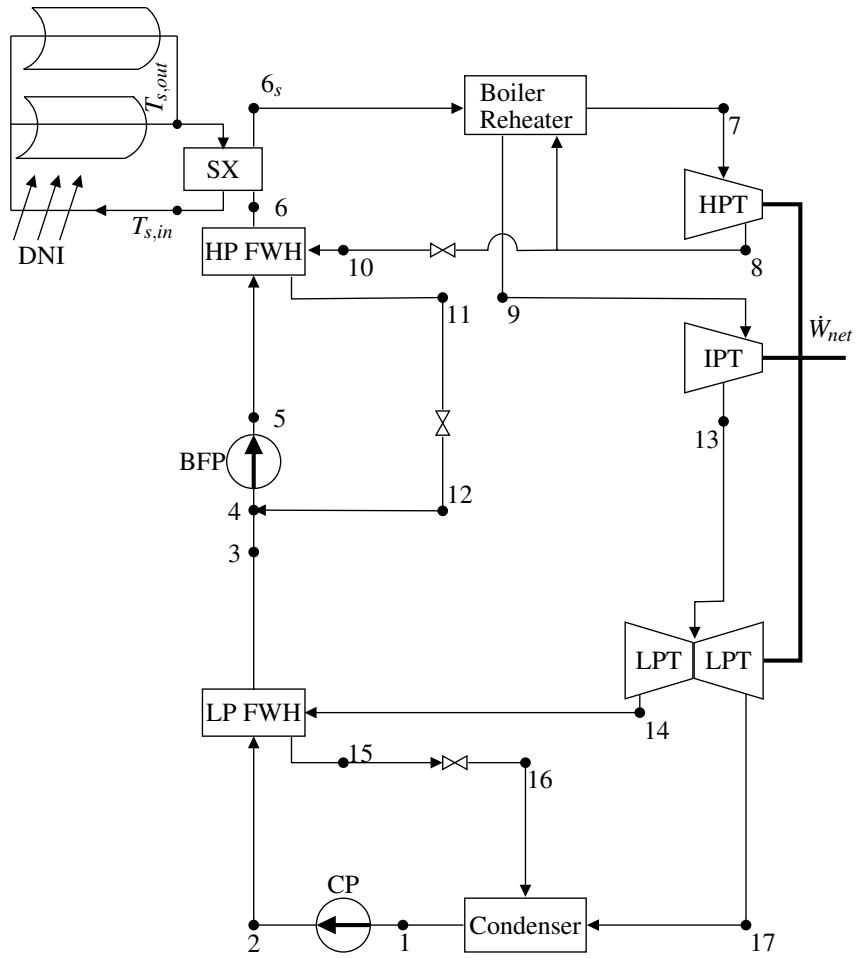


Figure G.4: FWH 7 bypass solar integration configuration.

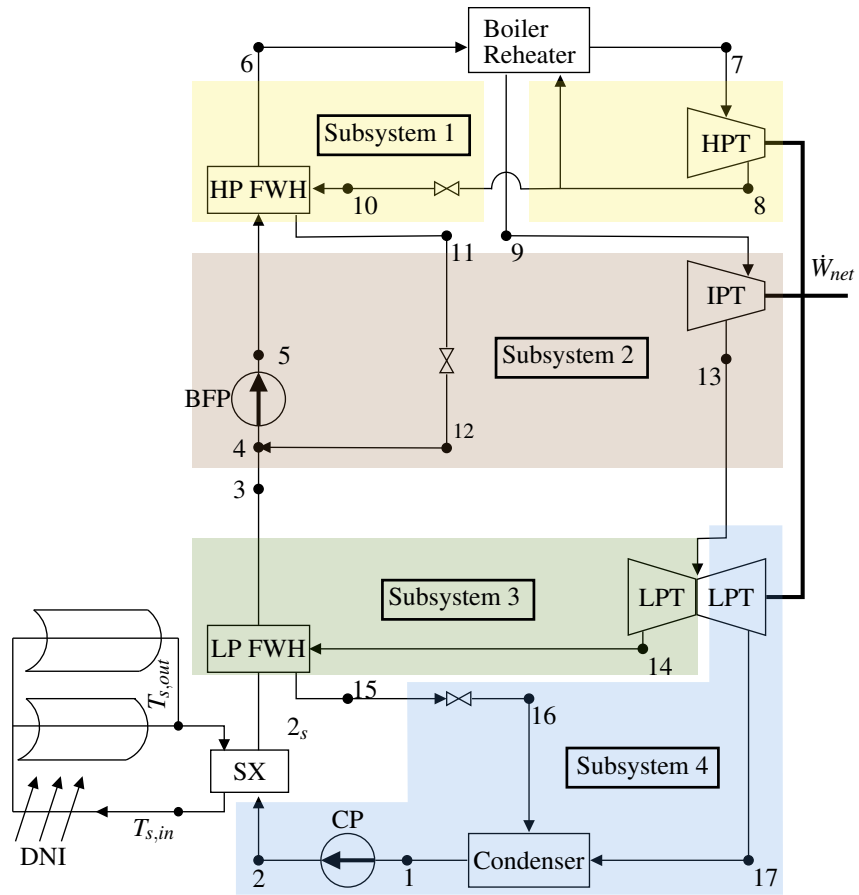


Figure G.5: Subsystem division for SX Model integration at FWH 1 or FWH 2 bypass.

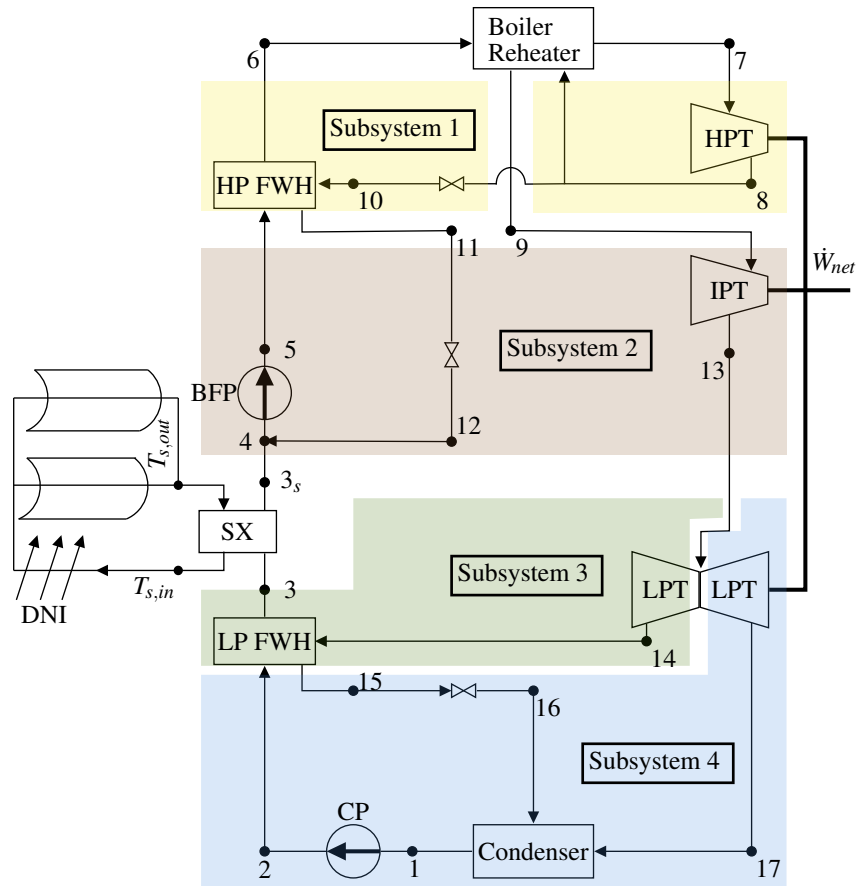


Figure G.6: Subsystem division for SX Model integration at FWH 3 bypass.

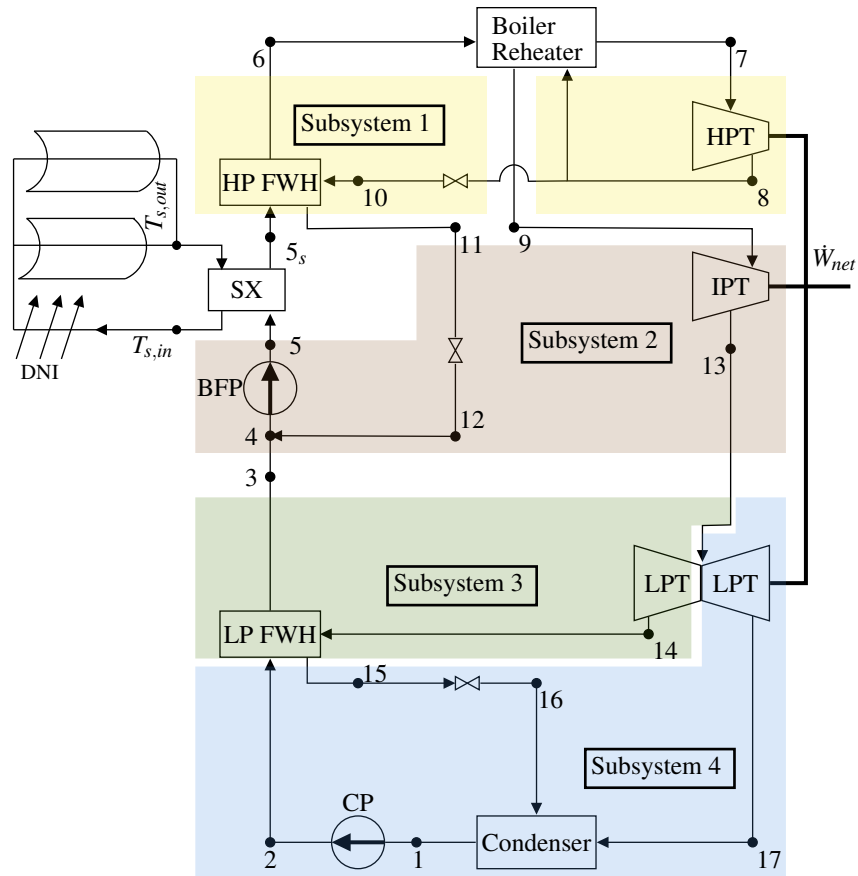


Figure G.7: Subsystem division for SX Model integration at FWH 5 or FWH 6 bypass..

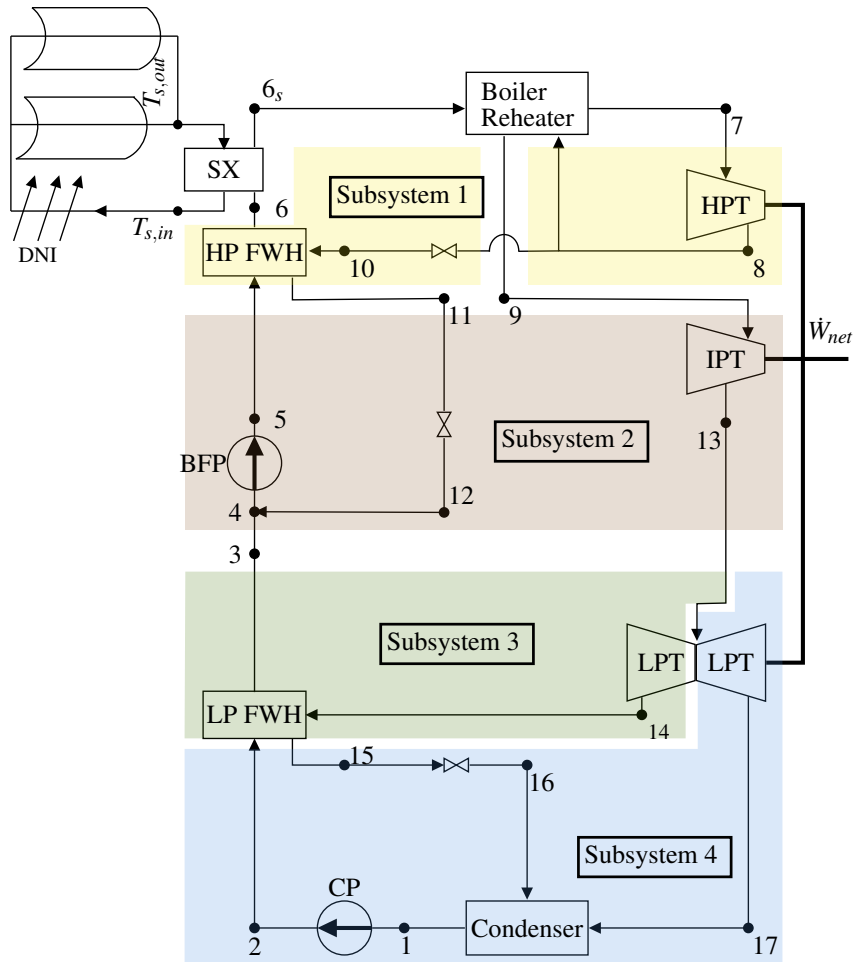


Figure G.8: Subsystem division for SX Model integration at FWH 7 bypass.

APPENDIX H. MATLAB FUNCTIONS

H.1 Optimization

```
1 % SX_opt
2 % Created by Aaron Bame (aaron.bame@gmail.com)
3
4 FWHres=zeros(6,2);
5 kres=zeros(6,2);
6 zeros(6,2);
7 weights=5;
8 w(1,:)=0:(1/weights):1;
9 w(2,:)=1-w(1,:);
10
11 %% PTC
12 TECH=1;
13 for i=1:2
14     for j=1:3
15         [TECH,i,j]
16         for l=1:length(w(1,:))
17             w(1,l)
18             index=3*(i-1)+j;
19             [kres(index,l),FWHres(index,l),~,~]=kopt(1,i,j,w(:,l));
20         end
21     end
22 end
23
24 %% LFR
25 TECH=2;
26 iPF=2;
```

```

27 for i=1:2
28     for j=1:3
29         [TECH,i,j]
30         for l=1:length(w(1,:))
31             w(1,l)
32             index=3*(i-1)+j;
33             [kres((6+index),l),FWHres((6+index),l),~,~]=kopt(2,i,j,w(:,l));
34         end
35     end
36 end
37
38
39 %% Optimization
40 function [xopt, fopt, exitflag, output] = kopt(TECH,PFLAG,FWHno,w)
41
42     % -----Starting point and bounds-----
43     x0 = [0.09];    % Starting guess
44     ub = [0.15];    % Upper bound
45     lb = [0.06];    % Lower bound
46
47     % -----Linear constraints-----
48     A = [];
49     b = [];
50     Aeq = [];
51     beq = [];
52
53     % -----Objective and Non-linear Constraints-----
54     function [f, c, ceq] = objcon(k)
55
56         N=correlations.N();          % [yrs] Project life
57         Amax=correlations.Amax();     % [ac] Max solar field area
58         Amax=Amax*4046.86;           % [m^2] Convert max area to m^2
59         hsun=correlations.hsun();     % [hrs] Average useful sunlight time
60         rc=correlations.rc();
61         DNI=correlations.DNI();
62

```

```

63     % Calculate parameters for objective values
64     [Wnet, Qsav, Wsol, qsol]=SX_model(k, PFLAG, FWHno);
65     [~,~, Ar, Af]=solfield(TECH, qsol);
66     [LCOE, CC, PBT1, ~, ~]=LCOE_Calc(Ar, TECH, Wsol, Qsav);
67
68     % Objectives
69     OBJ1=(Qsav.*Ar*rc(TECH)*DNI)./(CC.*Wnet);
70     OBJ2=1./(LCOE*PBT1*hsun*365)*1e2;
71     f=-w(1)*OBJ1-w(2)*OBJ2;
72
73     c=zeros(2,1);
74     c(1)=(Af-Amax)*1e-7;
75     c(2)=(PBT1-N)*1e-1;
76
77     ceq=[];
78
79 end
80
81 % -----Call fmincon-----
82 options = optimoptions(@fmincon, 'display', 'iter-detailed');
83 [xopt, fopt, exitflag, output] = fmincon(@obj, x0, A, b, Aeq, beq, ...
84     lb, ub, @con, options);
85
86
87 % -----Separate obj/con (do not change)-----
88 function [f] = obj(x)
89     [f, ~, ~] = objcon(x);
90 end
91 function [c, ceq] = con(x)
92     [~, c, ceq] = objcon(x);
93 end
94 end

```

H.2 Solar Integration

```
1 % Solar Integration model
2 % Created by Aaron Bame (aaron.bame@gmail.com)
3
4 %%%%%%%%%%%%%%%%%%%%%%%%%%%%%%%%%%%%%%%%%%%%%%%%%%%%%%%%%%%%%%%%%%%%%%%%%Objective/Algorithm%%%%%%%%%%%%%%%%%%%%%%%%%%%%%%%%%%%%%%%%%%%%%%%%%%%%%%%%%%%%%%%%%%%%%%%%
5 %   Simulate the integration of CSP by FWH bypass. Each state point is   %
6 %       calculated following the process provided in the 'State Points'   %
7 %       appendix in the final report. See report for derivations and     %
8 %       explanations for the methods used in this model                 %
9 %%%%%%%%%%%%%%%%%%%%%%%%%%%%%%%%%%%%%%%%%%%%%%%%%%%%%%%%%%%%%%%%%%%%%%%%%
10
11 %%%%%%%%%%%%%%%%%%%%%%%%%%%%%%%%%%%%%%%%%%%%%%%%%%%%%%%%%%%%%%%%%%%%%%%%%Inputs%%%%%%%%%%%%%%%%%%%%%%%%%%%%%%%%%%%%%%%%%%%%%%%%%%%%%%%%%%%%%%%%%%%%%%%%
12 %       k:   CSP augment fraction                                       %
13 %   PFLAG:  Flag for FWH pressure level                                 %
14 %           1 - LP FWH                                                %
15 %           2 - HP FWH                                                %
16 %   FWHno:  FWH number in the pressure stage specified by PFLAG      %
17 %%%%%%%%%%%%%%%%%%%%%%%%%%%%%%%%%%%%%%%%%%%%%%%%%%%%%%%%%%%%%%%%%%%%%%%%%
18
19 %%%%%%%%%%%%%%%%%%%%%%%%%%%%%%%%%%%%%%%%%%%%%%%%%%%%%%%%%%%%%%%%%%%%%%%%%Outputs%%%%%%%%%%%%%%%%%%%%%%%%%%%%%%%%%%%%%%%%%%%%%%%%%%%%%%%%%%%%%%%%%%%%%%%%
20 %   Wnet:   Net power output of the hybrid power plant [MW]           %
21 %   Qsav:   Amount of coal saved from hybridization [MW]             %
22 %           (based on SX_model k = 0 condition simulation)           %
23 %   Wsol:   Solar contribution to the total power output [MW]        %
24 %   qs:     CSP heating transferred to the power plant by FWH bypass [kW] %
25 %%%%%%%%%%%%%%%%%%%%%%%%%%%%%%%%%%%%%%%%%%%%%%%%%%%%%%%%%%%%%%%%%%%%%%%%%
26
27 function [Wnet,Qsav,Wsol,qs]=SX_model(k,PFLAG,FWHno)
28
29
30 %% Power Plant Input Parameters
31
32 switch PFLAG
33     case 1
```

```

34         SX='LP';
35     case 2
36         SX='HP';
37     otherwise
38         SX='SH';
39 end
40
41 N=21;
42 T=zeros(1,N);
43 P=zeros(1,N);
44 h=zeros(1,N);
45 s=zeros(1,N);
46 mdot=zeros(1,N);
47
48 TmaxK=810;           % K           Boiler operating temperature
49 etalp=0.918187;     %           LPT isentropic efficiency
50 etaip=0.917276;     %           IPT isentropic efficiency
51 eta hp=0.894375;    %           HPT isentropic efficiency
52 etaboil=0.8978694531; %           Boiler efficiency
53 DCLP=50/9;          % deg C      LP FWH DC
54 DCHP=50/9;          % deg C      HP FWH DC
55 etacp=0.44;         %           CP isentropic efficiency
56 etabfp=0.809;       %           BFPT isentropic efficiency
57 Td=300;             % K           Dead state temperature
58 % Tk=2445;          % K           Boiler flame temperature
59 Tsun=5800;          % K           Boundary temperature of the sun
60
61 Wmax=525;           % MW         Maximum power output
62 HPlim=140;          % MW         HPT power output limit
63 IPlim=110;          % MW         IPT power output limit
64 LPlim=270;          % MW         LPT power output limit
65 Qrate=1273;         % MW         Nominal Hunter heating load
66 Q0=1276;            % MW         Heating load calculated from k=0%
67 qs=k/(1-k)*Q0;     % MW         CSP heating transferred to the cycle
68 qs=qs*1000;        % kW         Convert MW to kW
69 if (strcmp(SX,'LP'))

```

```

70     qsol1p=qs;
71     qsolhp=0;
72 else
73     qsol1p=0;
74     qsolhp=qs;
75 end
76
77 %% Cycle Analysis
78
79 %List of states in order evaluated
80 % 7-Boiler exit
81 % 8-HPT exhaust
82 % 10-HP FWH extraction throttling
83 % 9-Reheat exit
84 % 13-IPT exhaust
85 % 14-LPT bleed exit
86 % 17-LPT exhaust
87 % 1-Condenser exit
88 % 2-CP exit
89 % 3-LP FWH cold exit
90 % 15-LP FWH hot exit
91 % 16-LP FWH drain cooler
92 % 6-HP FWH cold exit
93 % Guess 5-HP FWH cold inlet
94 % 11-HP FWH hot exit
95 % 12-HP FWH drain cooler
96 % 4-Mixing/deaerator
97 % Check 5 and iterate
98
99 % Set the simulation power flag. FLAGpow=1 when all power limits are
100 % satisfied
101 FLAGpow=0;
102
103 % Starting guess for 1st stage pressure [MPa]
104 Ps1=14; % 1875 psi
105

```

```

106 % Plant input: Constant pressure ratio from HPT 1st stage to exhaust
107 rHPs1=2.9909;
108
109 % Mass Extraction fractions calculated from Hunter Heat Balance Diagram
110 mf7=0.37415;
111 mf6=0.150794;
112 mf5=0.188209;
113 mf3=0.037;
114 mf2=0.0355;
115 mf1=0.057;
116
117 % Begin iteration until all turbine power limits are satisfied (FLAGpow=1)
118 while(~FLAGpow)
119
120     % Pull correlation/constant values from correlation expressions input
121     % to correlations.m file
122
123     corr=correlations(Ps1);
124     mflow=corr.mdot;
125     mda=corr.mda;
126     PBFP=corr.pbfp;
127     PHP=Ps1*corr.php;
128     rFWH6=corr.rf6;
129     rFWH5=corr.rf5;
130     rDA=corr.rda;
131     rFWH3=corr.rf3;
132     rFWH2=corr.rf2;
133     rFWH1=corr.rf1;
134     rIPT=corr.rip;
135     rRH=corr.rrh;
136     Tk=corr.Tk;
137
138
139     dm=mflow-mdm;
140
141     %Find new bleed values

```

```

142 % HP Stage
143 rHP=[rFWH5,rFWH6,rHPs1]; % High to low pressure extraction ratios
144 PHPex=Ps1/rHP(3);
145 PIPi=PHPex/rRH;
146 HPex=[PIPi./rHP(1:2),PHPex];
147 mHP=[mf5,mf6,mf7];
148 mHP=mHP.*dm;
149 if (strcmp(SX,'HP'))
150     HPex(FWHno)=[];
151     mHP(FWHno)=[];
152 end
153 hp_ave=bleedpress(mHP,HPex);
154 hpbleed=hp_ave(1);
155 pHPFWH=hp_ave(2);
156 mLpi=mflow-sum(mHP);
157 mDAex=dm-sum(mHP);
158
159 % LP Stage
160 rLP=[rFWH1,rFWH2,rFWH3,rDA];
161 PLPi=PIPi/rIPT;
162 LPTex=PLPi./rLP;
163 mLP=[mf1,mf2,mf3,mDAex];
164 mLP(1:3)=mLP(1:3).*mLpi;
165 Pmin=LPTex(1);
166 PCP=LPTex(end);
167 if (strcmp(SX,'LP'))
168     LPTex(FWHno)=[];
169     mLP(FWHno)=[];
170 end
171 lp_ave=bleedpress(mLP,LPTex);
172 PLP_bleed=lp_ave(2);
173 lpbleed=lp_ave(1);
174
175 % Begin simulation of solar integration model
176 % State 7 (HP Turbine inlet)
177 T(7)=TmaxK;

```

```

178     P(7)=PHP;
179     temp=waterprops('TP',[T(7),P(7)],['D','H','S']);
180     rho(7)=temp(1);
181     h(7)=temp(2);
182     s(7)=temp(3);
183     mdot(7)=mflow;
184
185     % State 8 (HPT exhaust)
186     P(8)=PHPeX;
187     s(8)=s(7);
188     mdot(8)=mflow;
189     temp=waterprops('PS',[P(8),s(8)],['T','H']);
190     Ts8=temp(1);
191     hs8=temp(2);
192     h(8)=h(7)-(h(7)-hs8)*etahp;
193     temp=waterprops('PH',[P(8),h(8)],['T','D','S']);
194     T(8)=temp(1);
195     rho(8)=temp(2);
196     s(8)=temp(3);
197
198     % HP FWH extraction model option 2 (toggle comment to execute option 3)
199     % State 9 (Reheat exit)
200     P(9)=PIPi;
201     T(9)=TmaxK;
202     temp=waterprops('PT',[P(9),T(9)],['D','H','S']);
203     rho(9)=temp(1);
204     h(9)=temp(2);
205     s(9)=temp(3);
206     mdot(9)=mdot(8)-hpbleed;
207
208     % State 10 (HP FWH extraction throttling)
209     h(10)=h(8);
210     P(10)=pHPFWH;
211     temp=waterprops('PH',[P(10),h(10)],['T','D','S']);
212     T(10)=temp(1);
213     rho(10)=temp(2);

```

```

214     s(10)=temp(3);
215     mdot(10)=hpbleed;
216     % End option 2 simulation section
217
218     % HP FWH extraction model option 3 (toggle comment to execute option 2)
219     %
220     % State 9
221     %
222     P(9)=PIPi;
223     T(9)=TmaxK;
224     temp=waterprops('PT',[P(9),T(9)],['D','H','S']);
225     rho(9)=temp(1);
226     h(9)=temp(2);
227     s(9)=temp(3);
228     mdot(9)=mdot(8);
229     %
230     % State 10 (IPT extraction)
231     %
232     mdot(10)=hpbleed;
233     P(10)=pHPFWH;
234     h10s=waterprops('PS',[P(10),s(9)],'H');
235     h(10)=h(9)-etaip*(h(9)-h10s);
236     temp=waterprops('PH',[P(10),h(10)],['T','D','S']);
237     T(10)=temp(1);
238     rho(10)=temp(2);
239     s(10)=temp(3);
240     % End option 2 simulation section
241
242     % State 13 (IPT Exit w/efficiency)
243     P(13)=PLPi;
244     s(13)=s(9);
245     temp=waterprops('PS',[P(13),s(13)],['T','H']);
246     T13s=temp(1);
247     h13s=temp(2);
248     mdot(13)=mdot(8)-hpbleed;
249     h(13)=h(9)-etaip*(h(9)-h13s);
250     temp=waterprops('PH',[P(13),h(13)],['T','D','S']);
251     T(13)=temp(1);
252     rho(13)=temp(2);

```

```

250     s(13)=temp(3);
251
252     % State 14 (LPT Extraction Exit)
253     s(14)=s(13);
254     P(14)=PLP_bleed;
255     temp=waterprops('PS',[P(14),s(14)],['T','H']);
256     T14s=temp(1);
257     h14s=temp(2);
258     mdot(14)=lpbleed;
259     h(14)=h(13)-etalp*(h(13)-h14s);
260     temp=waterprops('PH',[P(14),h(14)],['T','D','S']);
261     T(14)=temp(1);
262     rho(14)=temp(2);
263     s(14)=temp(3);
264
265     % State 17 (LPT Exit)
266     s(17)=s(13);
267     P(17)=Pmin;
268     temp=waterprops('PS',[P(17),s(17)],['T','H']);
269     T17s=temp(1);
270     h17s=temp(2);
271     mdot(17)=mdot(13)-lpbleed;
272     h(17)=h(13)-etalp*(h(13)-h17s);
273     temp=waterprops('PH',[P(17),h(17)],['T','D','S']);
274     T(17)=temp(1);
275     rho(17)=temp(2);
276     s(17)=temp(3);
277
278     % Check Turbine limits
279     Whp=mdot(8)*(h(7)-h(8))/1000;
280
281     % HP FWH extraction model option 2 (toggle comment to execute option 3)
282     Wip=(mdot(9)*(h(9)-h(13)))/1000;
283     % HP FWH extraction model option 3 (toggle comment to execute option 2)
284     % Wip=(mdot(9)*(h(9)-h(13))+mdot(10)*(h(9)-h(10)))/1000;
285

```

```

286     Wlp=(mdot(14)*(h(13)-h(14))+mdot(17)*(h(13)-h(17)))/1000;
287     Wtot=Whp+Wip+Wlp;
288     if(Wtot>Wmax)
289         if(Whp>HPlim||Wip>IPlim||Wlp>LPlim)
290             % Change PS1
291             Ps1=0.95*Ps1;
292         end
293     else
294         FLAGpow=1;
295     end
296 end
297
298 % State 1 (Condenser Exit)
299 P(1)=Pmin;
300 x_1=0;
301 temp=waterprops('PQ',[P(1),x_1],['T','D','H','S']);
302 T(1)=temp(1);
303 rho(1)=temp(2);
304 h(1)=temp(3);
305 s(1)=temp(4);
306 mdot(1)=lpbleed+mdot(17);
307
308 % State 2 (CP Exit)
309 s(2)=s(1);
310 P(2)=PCP;
311 mdot(2)=mdot(1);
312 temp=waterprops('PS',[P(2),s(2)],['T','H']);
313 Ts2=temp(1);
314 hs2=temp(2);
315 h(2)=h(1)+(hs2-h(1))*1/etacp;
316 temp=waterprops('PH',[P(2),h(2)],['T','D','S']);
317 T(2)=temp(1);
318 rho(2)=temp(2);
319 s(2)=temp(3);
320
321 % State 2sol

```

```

322 P(18)=P(2);
323 mdot(18)=mdot(2);
324 if(strcmp(SX,'LP')&&(FWHno<3))
325     h(18)=qsol1p/mdot(2)+h(2);
326     temp=waterprops('PH',[P(18),h(18)],['T','D','S']);
327     T(18)=temp(1);
328     rho(18)=temp(2);
329     s(18)=temp(3);
330 else
331     h(18)=h(2);
332     T(18)=T(2);
333     rho(18)=rho(2);
334     s(18)=s(2);
335 end
336
337 % State 15
338 mdot(15)=mdot(14);
339 P(15)=P(14);
340 T(15)=T(18)+DCLP;
341 temp=waterprops('PT',[P(15),T(15)],['D','H','S']);
342 rho(15)=temp(1);
343 h(15)=temp(2);
344 s(15)=temp(3);
345
346 mdot(3)=mdot(2);
347 P(3)=P(2);
348 h(3)=mdot(15)/mdot(3)*(h(14)-h(15))+h(18);
349 temp=waterprops('PH',[P(3),h(3)],['T','D','S']);
350 T(3)=temp(1);
351 rho(3)=temp(2);
352 s(3)=temp(3);
353 s3sat=waterprops('PQ',[P(3),0],['S']);
354 if(s(3)>s3sat)
355     s(3)=s3sat;
356     temp=waterprops('PS',[P(3),s(3)],['T','D','H']);
357     T(3)=temp(1);

```

```

358     rho(3)=temp(2);
359     h(3)=temp(3);
360     %Also change 15
361     h(15)=h(14)-mdot(3)/mdot(15)*(h(3)-h(18));
362     temp=waterprops('PH',[P(15),h(15)],['T','D','S']);
363     T(15)=temp(1);
364     rho(15)=temp(2);
365     s(15)=temp(3);
366 end
367
368 % State 3sol
369 P(19)=P(3);
370 mdot(19)=mdot(3);
371 if(strcmp(SX,'LP')&&FWHno==3)
372     h(19)=qsol1p/mdot(3)+h(3); %qsol=etasx*mdot(3)*(h3sol-h(3))
373     temp=waterprops('PH',[P(19),h(19)],['T','D','S']);
374     T(19)=temp(1);
375     rho(19)=temp(2);
376     s(19)=temp(3);
377 else
378     h(19)=h(3);
379     T(19)=T(3);
380     rho(19)=rho(3);
381     s(19)=s(3);
382 end
383
384
385
386 % State 16
387 mdot(16)=mdot(15);
388 P(16)=P(1);
389 h(16)=h(15);
390 temp=waterprops('PH',[P(16),h(16)],['T','D','S']);
391 T(16)=temp(1);
392 rho(16)=temp(2);
393 s(16)=temp(3);

```

```

394
395 % Guess 5, find 11->12->4, check 5 and iterate
396 mdot(5)=mflow;
397 P(5)=PBFP;
398 T(5)=450;
399 T51=T(5);
400 err=1;
401 tol=1e-3;
402 i=0;
403 while(err>tol)
404     i=i+1;
405     T(5)=(T(5)+T51)/2;
406     temp=waterprops('PT',[P(5),T(5)],['D','H','S']);
407     rho(5)=temp(1);
408     h(5)=temp(2);
409     s(5)=temp(3);
410
411     % State 5sol
412     mdot(20)=mdot(4);
413     P(20)=P(5);
414     if(strcmp(SX,'HP')&&FWHno<3)
415         h(20)=qsolhp/mdot(5)+h(5);
416         temp=waterprops('PH',[P(20),h(20)],['T','D','S']);
417         T(20)=temp(1);
418         rho(20)=temp(2);
419         s(20)=temp(3);
420     else
421         h(20)=h(5);
422         T(20)=T(5);
423         rho(20)=rho(5);
424         s(20)=s(5);
425     end
426
427     % State 11
428     mdot(11)=mdot(10);
429     P(11)=P(10);

```

```

430 T(11)=T(20)+DCHP;
431 temp=waterprops('PT',[P(11),T(11)],['D','H','S']);
432 rho(11)=temp(1);
433 h(11)=temp(2);
434 s(11)=temp(3);
435
436 % State 12
437 mdot(12)=mdot(11);
438 h(12)=h(11);
439 P(12)=P(3);
440 temp=waterprops('PH',[P(12),h(12)],['T','D','S']);
441 T(12)=temp(1);
442 rho(12)=temp(2);
443 s(12)=temp(3);
444
445 % State 4
446 mdot(4)=mdot(12)+mdot(3);
447 P(4)=P(3);
448 h(4)=1/mdot(4)*(mdot(3)*h(19)+mdot(12)*h(12));
449 temp=waterprops('PH',[P(4),h(4)],['T','D','S']);
450 T(4)=temp(1);
451 rho(4)=temp(2);
452 s(4)=temp(3);
453
454 % Check state 5
455 h5s=waterprops('PS',[P(5),s(4)],['H']);
456 h(5)=(h5s-h(4))/etabfp+h(4);
457 temp=waterprops('PH',[P(5),h(5)],['T','D','S']);
458 Tnew=temp(1);
459 rho(5)=temp(2);
460 s(5)=temp(3);
461 err=abs((T51-Tnew)/T51);
462 if(err>tol)
463     T51=Tnew;
464 else
465     T(5)=Tnew;

```

```

466     end
467 end
468
469 % State 5sol
470 mdot(20)=mdot(4);
471 P(20)=P(5);
472 if(strcmp(SX,'HP')&&FWHno<3)
473     h(20)=qsolhp/mdot(5)+h(5);
474     temp=waterprops('PH',[P(20),h(20)],['T','D','S']);
475     T(20)=temp(1);
476     rho(20)=temp(2);
477     s(20)=temp(3);
478 else
479     h(20)=h(5);
480     T(20)=T(5);
481     rho(20)=rho(5);
482     s(20)=s(5);
483 end
484
485 % State 6
486 mdot(6)=mflow;
487 P(6)=PBFP;
488 h(6)=mdot(10)/mdot(6)*(h(10)-h(11))+h(20);
489 temp=waterprops('PH',[P(6),h(6)],['T','D','S']);
490 T(6)=temp(1);
491 rho(6)=temp(2);
492 s(6)=temp(3);
493 s6sat=waterprops('PQ',[P(6),0], 'S');
494 if(s(6)>s6sat)
495     s(6)=s6sat;
496     temp=waterprops('PS',[P(6),s(6)],['T','D','H']);
497     T(6)=temp(1);
498     rho(6)=temp(2);
499     h(6)=temp(3);
500 %Also change 11
501 h(11)=h(10)-mdot(6)/mdot(11)*(h(6)-h(5));

```

```

502     temp=waterprops('PH',[P(11),h(11)],['T','D','S']);
503     T(11)=temp(1);
504     rho(11)=temp(2);
505     s(11)=temp(3);
506 end
507
508 % State 6sol
509 mdot(21)=mdot(6);
510 P(21)=P(6);
511 if(strcmp(SX,'HP')&&FWHno==3)
512     h(21)=qsolhp/mdot(6)+h(6); %qsolhp=mdot6sol*(h6sol-h6)
513     temp=waterprops('PH',[P(21),h(21)],['T','D','S']);
514     T(21)=temp(1);
515     rho(21)=temp(2);
516     s(21)=temp(3);
517 else
518     h(21)=h(6);
519     T(21)=T(6);
520     rho(21)=rho(6);
521     s(21)=s(6);
522 end
523
524 % % T-s Data storage - Uncomment to save data for specific condition
525 % Tmain=[T(1:9),T(13),T(17),T(1)];
526 % smain=[s(1:9),s(13),s(17),s(1)];
527 %
528 % TSmodel_main=[Tmain;smain];
529 %
530 % %HP FWH
531 % Thpfwh=[T(8),T(10:12),T(4)];
532 % shpfwh=[s(8),s(10:12),s(4)];
533 % Tsmodel_hpfwh=[Thpfwh;shpfwh];
534 %
535 % %LP FWH
536 % Tlpfwh=[T(13:16),T(1)];
537 % slpfwh=[s(13:16),s(1)];

```

```

538 % Tsmodel_lpfwh=[Tlpfwh;slpfwh];
539 %
540 % txtname='SImodel.txt';
541 % fid=fopen(txtname,'w');
542 % options='%16.15f %16.15f\r\n';
543 % fprintf(fid,options,[Tsmodel_main,[0;0]]);
544 % fprintf(fid,options,[Tsmodel_hpfwh,[0;0]]);
545 % fprintf(fid,options,[Tsmodel_lpfwh,[0;0]]);
546 %
547 % fclose(fid);
548
549 %% Output/Performance Parameters
550 %HP
551 Whp=mdot(8)*(h(7)-h(8)); % [kW]
552
553 %IP
554 Wip=mdot(9)*(h(9)-h(13)); % [kW]
555
556 % HP FWH extraction model option 2 (toggle comment to execute option 3)
557 Wipex=0; % [kW]
558 % HP FWH extraction model option 3 (toggle comment to execute option 2)
559 % Wipex=mdot(10)*(h(9)-h(10)); % [kW]
560
561 %LP
562 Wlpbleed=mdot(14)*(h(13)-h(14)); % [kW]
563 Wlp=mdot(17)*(h(13)-h(17)); % [kW]
564
565 %Pumping
566 Wcp=mdot(1)*(h(2)-h(1)); % [kW]
567 Wbfp=mdot(5)*(h(5)-h(4)); % [kW]
568 Win=(Wcp+Wbfp)*10^-3; % [MW]
569
570 %Heating
571 Qin=mdot(6)*(h(7)-h(21))+mdot(9)*(h(9)-h(8)); % [kW]
572 Qin=Qin/etaboil*10^-3; % [MW]
573 Qsav=Q0-Qin; % [MW]

```

```

574
575 Wout=(Whp+Wip+Wipex+Wlp+Wlpbleed)*10^-3;           % [MW]
576 Wnet=Wout-Win;                                       % [MW]
577 Werr=(Wnet-511.237)/511.237;                         % [-]
578 eff=Wnet/(Qin+qs/1000);                             % [-]
579 etaII=Wnet/((1-Td/Tk)*Qin+(1-Td/Tsun)*qs/1000);    % [-]
580
581 Wsol=Solar_Contribution(['T','P','h','s',mdot']);    % [MW]
582 end

```

H.3 Solar Contribution

```
1 % Function to calculate the solar contribution of the hybrid CSP and coal
2 % power plant
3 % Created by Joseph Furner (joseph.furner@gmail.com)
4
5 % Inputs:
6 % Nodes      -type:      21x5 matrix
7 %            meaning:    state point properties. Columns are in order from
8 %            left to right: T [K], P [MPa], H [kJ kg-1],
9 %            S [kJ kg-1 K-1], mdot [kg s-1].
10 % Outputs:
11 % Wsol      -type:      double
12 %           meaning:    Solar contribution [MW]
13 %
14 % eD        -type:      double
15 %           meaning:    Solar exergy destruction factor
16 %
17 % sprpo     -type:      double
18 %           meaning:    Solar proportion
19 %
20 % esol      -type:      double
21 %           meaning:    Exergy addition from CSP field
22 %
23 function [Wsol,eD,sprpo,esol] = SolarContribution(Nodes)
24
25 state = Nodes(1:17,:);
26 sol = Nodes(18:end,:);
27
28 T0 = 298;
29 T = state(:,1);
30 P = state(:,2);
31 H = state(:,3);
32 S = state(:,4);
33 mdot = state(:,5);
```

```

34
35
36 % Subsystem 1
37 in{1} = [H(7) S(7) mdot(7);H(5) S(5) mdot(5)];
38 out{1} = [H(8) S(8) mdot(9);H(6) S(6) mdot(6);H(11) S(11) mdot(11)];
39 % Subsystem 2
40 in{2} = [H(9) S(9) mdot(9);H(3) S(3) mdot(3);H(11) S(11) mdot(11)];
41 out{2} = [H(13) S(13) mdot(13);H(5) S(5) mdot(5)];
42 % Subsystem 3
43 in{3} = [H(13) S(13) mdot(13);H(2) S(2) mdot(2)];
44 out{3} = [H(14) S(14) mdot(17);H(3) S(3) mdot(3);H(15) S(15) mdot(15)];
45 % Subsystem 4
46 in{4} = [H(14) S(14) mdot(17);H(15) S(15) mdot(15)];
47 out{4} = [H(2) S(2) mdot(2)];
48
49 if sol(1,4) ~= S(2)
50     used = 1;
51     Hsol = [H(2) sol(1,3)];
52     Ssol = [S(2) sol(1,4)];
53     in{3}(2,1:2) = [Hsol(2) Ssol(2)];
54     msprpo = [mdot(7) mdot(9) mdot(2)];
55 elseif sol(2,4) ~= S(3)
56     used = 2;
57     Hsol = [H(3) sol(2,3)];
58     Ssol = [S(3) sol(2,4)];
59     in{2}(2,1:2) = [Hsol(2) Ssol(2)];
60     msprpo = [mdot(7) mdot(9) mdot(3)];
61 elseif sol(3,4) ~= S(5)
62     used = 3;
63     Hsol = [H(5) sol(3,3)];
64     Ssol = [S(5) sol(3,4)];
65     in{1}(2,1:2) = [Hsol(2) Ssol(2)];
66     msprpo = [mdot(7) mdot(9) mdot(5)];
67 elseif sol(4,4) ~= S(6)
68     used = 4;
69     Hsol = [H(6) sol(4,3)];

```

```

70     Ssol = [S(6) sol(4,4)];
71     msprpo = [mdot(7) mdot(9) mdot(6)];
72 end
73
74 liquid = [T(2),S(2);
75           sol(1,1),sol(1,4);
76           T(3),S(3);
77           sol(2,1),sol(2,4);
78           T(4),S(4);
79           T(5),S(5);
80           sol(3,1),sol(3,4);
81           T(6),S(6);
82           sol(4,1),sol(4,4)];
83 Ssprpo = [Ssol(1) Ssol(2) sol(4,4) S(7) S(8) S(9)];
84 m0 = mdot(7);
85 Ps = P(7);
86 Prh = P(9);
87 Pw = [Ps Prh];
88 Sthtl = [S(8) S(10)];
89 Tthtl = [T(8) T(10)];
90 Pcs = [P(6) P(10) P(13) P(14) P(17)];
91 TS = zeros(1,length(SSprpo));
92 for i = 1:length(Pcs)
93     for j = 1:length(SSprpo)
94         TS(i,j) = waterprops('PS',[Pcs(i),SSprpo(j)],'T');
95     end
96 end
97 WHPT = (H(7) - H(8))*mdot(7);
98 WIPT = (H(9) - H(13))*mdot(9);
99 WLPT1 = (H(13) - H(14))*mdot(13);
100 WLPT2 = (H(14) - H(17))*mdot(17);
101 WBFP = mdot(4)*(H(5)-H(4));
102 WCP = mdot(1)*(H(2) - H(1));
103 Qcon = (mdot(17)*H(17)) + (mdot(16)*H(16)) - (mdot(1)*H(1));
104 Xwq = [WHPT,WIPT - WBFP,WLPT1,WLPT2 + ((1 - (T0/T0))*Qcon) - WCP];
105

```

```

106
107
108 eD = zeros(1,4);
109 sprpo = zeros(1,4);
110 for i = 1:4
111     if i > 2
112         Sthtl = [0 0];
113         Tthtl = [0 0];
114     end
115     if used == 1
116         if i < 4
117             sprpo(i) = 0;
118         else
119             [sprpo(i)] = Solar_Prop([Pcs(i),Pcs(i+1)],msprpo,Ssprpo,Pw,...
120                 TS(i:i+1,:),Sthtl,Tthtl,liquid,[H(6),H(7)]);
121         end
122     elseif used == 2
123         if i < 3
124             sprpo(i) = 0;
125         else
126             [sprpo(i)] = Solar_Prop([Pcs(i),Pcs(i+1)],msprpo,Ssprpo,Pw,...
127                 TS(i:i+1,:),Sthtl,Tthtl,liquid,[H(6),H(7)]);
128         end
129     elseif used == 3
130         if i < 2
131             sprpo(i) = 0;
132         else
133             [sprpo(i)] = Solar_Prop([Pcs(i),Pcs(i+1)],msprpo,Ssprpo,Pw,...
134                 TS(i:i+1,:),Sthtl,Tthtl,liquid,[H(6),H(7)]);
135         end
136     elseif used == 4
137         if i < 1
138             sprpo(i) = 0;
139         else
140             [sprpo(i)] = Solar_Prop([Pcs(i),Pcs(i+1)],msprpo,Ssprpo,Pw,...
141                 TS(i:i+1,:),Sthtl,Tthtl,liquid,[H(6),H(7)]);

```

```

142     end
143 end
144 ein = sum((in{i}(:,1) - T0.*(in{i}(:,2))).*in{i}(:,3));
145 eout = sum((out{i}(:,1) - T0.*(out{i}(:,2))).*out{i}(:,3));
146 eD(i) = (ein - eout - Xwq(i))/m0;
147
148 end
149
150 esol = (msprpo(3)/m0)*((Hsol(2) - Hsol(1)) - T0*(Ssol(2) - Ssol(1)));
151 Wsol = 0.001*m0*(esol - sum(eD.*sprpo));
152 end

```

H.4 Solar Data

```
1 clear all
2 %% Header
3 % Created by Aaron Bame (aaron.bame@gmail.com)
4 % v1: 12/3/2019
5 %   Script to scrub multiple years of solar resource data downloaded from
6 %   NREL's NSRDB (https://maps.nrel.gov/nsrdb-viewer)
7
8 %   Assumes downloading data for:
9 %   yr | month | day | hr | min | DHI | DNI | Clearsky DNI | humid | Temp
10
11 %   Currently assumes every 30 minutes
12
13 % v2: 12/6/2019–Aaron Bame
14 %   Update downloaded data order:
15 %   yr | month | day | hr | min | DNI | CSDNI | zenith | Temp | Pressure
16 %   Calculate average daily zenith, correspondingly correct indices
17
18 % v3: 12/10/2019–Aaron Bame
19 %   Include calculation for minimum average spacing to eliminate shading
20 %   Use zenith angle, declination, azimuth, latitude,
21 %   and equations from Padilla USF thesis
22
23 %% Set up calendar array %calendar=[month; date; DNI; CSDNI; Dayhr; Energy]
24 calendar=zeros([365,6]);
25 begin=1;
26 %January (31 day)
27 jan=31;
28 calendar(begin:(begin+jan-1),1)=1;
29 calendar(begin:(begin+jan-1),2)=1:1:jan;
30 begin=begin+jan;
31 %February (28 day)
32 feb=28;
33 calendar(begin:(begin+feb-1),1)=2;
```

```
34 calendar(begin:(begin+feb-1),2)=1:1:feb;
35 begin=begin+feb;
36 %March (31 day)
37 mar=31;
38 calendar(begin:(begin+mar-1),1)=3;
39 calendar(begin:(begin+mar-1),2)=1:1:mar;
40 begin=begin+mar;
41 %April (30 day)
42 apr=30;
43 calendar(begin:(begin+apr-1),1)=4;
44 calendar(begin:(begin+apr-1),2)=1:1:apr;
45 begin=begin+apr;
46 %May (31 day)
47 may=31;
48 calendar(begin:(begin+may-1),1)=5;
49 calendar(begin:(begin+may-1),2)=1:1:may;
50 begin=begin+may;
51 %June (30 day)
52 jun=30;
53 calendar(begin:(begin+jun-1),1)=6;
54 calendar(begin:(begin+jun-1),2)=1:1:jun;
55 begin=begin+jun;
56 %July (31 day)
57 jul=31;
58 calendar(begin:(begin+jul-1),1)=7;
59 calendar(begin:(begin+jul-1),2)=1:1:jul;
60 begin=begin+jul;
61 %August (31 day)
62 aug=31;
63 calendar(begin:(begin+aug-1),1)=8;
64 calendar(begin:(begin+aug-1),2)=1:1:aug;
65 begin=begin+aug;
66 %September (30 day)
67 sep=30;
68 calendar(begin:(begin+sep-1),1)=9;
69 calendar(begin:(begin+sep-1),2)=1:1:sep;
```

```

70 begin=begin+sep;
71 %October (31 day)
72 oct=31;
73 calendar(begin:(begin+oct-1),1)=10;
74 calendar(begin:(begin+oct-1),2)=1:1:oct;
75 begin=begin+oct;
76 %November (30 day)
77 nov=30;
78 calendar(begin:(begin+nov-1),1)=11;
79 calendar(begin:(begin+nov-1),2)=1:1:nov;
80 begin=begin+nov;
81 %December (31 day)
82 dec=31;
83 calendar(begin:(begin+dec-1),1)=12;
84 calendar(begin:(begin+dec-1),2)=1:1:dec;
85 begin=begin+dec;
86
87 months=[jan,feb,mar,apr,may,jun,jul,aug,sep,oct,nov,dec];
88
89
90 %% Import the data
91
92 % Asks the user to select file(s)
93 % May select multiple files, must be from the same folder
94 [names,path]=uigetfile('*.csv','MultiSelect','on');
95 files=length(names);
96
97 if(files==29)
98     files=1;
99 end
100
101 phi=39.17; % Latitude [deg]
102 w=2.5; % PTC mirror width [m]
103
104 clearvars f filename header
105

```

```

106 % Set up array for length calculations; 1 Length for each year
107 Lspace=zeros(1,files);
108 % Variable used for numerator of Energy-weighted Length average
109 LEsum=0;
110
111 % Repeat for each year of data
112 for i=1:files
113
114     % Combine the file path and name into a single file name
115     if(files>1)
116         f=fullfile(path,names(i));
117     else
118         f=fullfile(path,names);
119     end
120     % Convert filename to a character variable
121     filename=char(f);
122     %Begin reading data from A4 of the .csv file
123     data=csvread(filename,3,0);
124
125     % Assign imported array to column variable names
126     year = data(:,1);
127     month = data(:,2);
128     day = data(:,3);
129     hour = data(:,4);
130     minute = data(:,5);
131     DNI = data(:,6); %W/m^2
132     CSDNI = data(:,7); %W/m^2
133     thetaz = data(:,8);
134     Temp = data(:,9);
135     Press = data(:,10);
136
137     % Clear temporary variables
138     clearvars data f;
139
140     N=48; %Number of readings in one day
141

```

```

142 %% Data Analysis
143 % Find the average for each day and then average across the whole month
144 for j=1:365 %Iterate through each day, j=day number from Jan 1
145
146     begin=j*N-47;
147     midnight=j*N;
148
149     rise=find(CSDNI(begin:midnight)>0,1,'first');
150     sunset=find(CSDNI(begin:midnight)>0,1,'last');
151
152     xtime=0:(30/(60*24):(1-30/(60*24)));
153     start=fix(now);
154     xtime=datestr(start+xtime,'HH:MM');
155     for v=1:48
156         times(v)=string(xtime(v,:));
157     end
158
159     % Daily flux average
160     a=begin+rise;
161     b=begin+sunset;
162     calendar(j,3)=calendar(j,3)+avg(DNI(a:b));
163     calendar(j,4)=calendar(j,4)+avg(CSDNI(a:b));
164     calendar(j,5)=calendar(j,5)+(sunset-rise+1)/2;
165     Eflux=avg(DNI(a:b))*(sunset-rise+1)/2;
166     % Eflux=1;
167     calendar(j,6)=Eflux;
168
169
170     % Calculate required length to avoid shading
171     delta=declination(i); % Declination angle for the day [deg]
172
173     % Length for sunrise
174     theta=thetaz(rise+2); % Zenith angle at sunrise [deg]
175     zeta=theta; % Solar tilt; zeta=theta for tracking [deg]
176     alpha=90-theta; % Altitude angle at sunrise [deg]
177

```

```

178     % Azimuth angle at sunrise (-) [deg]
179     gamma=-acosd((cosd(theta)*sind(phi)-sind(delta))...
180         /(sind(theta)*cosd(phi)));
181
182     % Angle of shadow extension [deg]
183     sigma=asind(sind(zeta)*cosd(gamma)/(tand(alpha)*...
184         (cosd(zeta)^2+sind(zeta)^2/tand(alpha)^2 ...
185         +sind(2*zeta)/tand(alpha)*sind(gamma)));
186     temp=w*(sind(zeta)*cosd(sigma)/tand(alpha)+cosd(zeta));
187     LEsum=LEsum+abs(temp)*Eflux;
188
189     % Length for sunset
190     theta=thetaz(sunset-4);
191     zeta=theta;
192     alpha=90-theta;
193
194     % Positive for sunset
195     gamma=acosd((cosd(theta)*sind(phi)-sind(delta))/...
196         (sind(theta)*cosd(phi)));
197     sigma=asind(sind(zeta)*cosd(gamma)/(tand(alpha)*...
198         (cosd(zeta)^2+sind(zeta)^2/tand(alpha)^2 ...
199         +sind(2*zeta)/tand(alpha)*sind(gamma)));
200
201     temp=w*(sind(zeta)*cosd(sigma)/tand(alpha)+cosd(zeta));
202     LEsum=LEsum+abs(temp)*Eflux;
203
204     end
205     Lspace(i)=LEsum/(2*sum(calendar(:,6)));
206     LEsum=0;
207 end
208
209 % Calculate the average for each day
210 calendar(:,3)=calendar(:,3)/files;
211 calendar(:,4)=calendar(:,4)/files;
212 calendar(:,5)=calendar(:,5)/files;
213

```

```

214 Lavg=avg(Lspace);
215
216 %% Data presentation
217 % Yearly average flux [W/m^2]
218 yearavg=sum(calendar(:,3))/length(calendar(:,3));
219 % Clear sky yearly average (Maximum solar condition) [W/m^2]
220 CSyearavg=sum(calendar(:,4))/length(calendar(:,4));
221 % Average hours of daylight [hrs]
222 hrs=sum(calendar(:,5))/length(calendar(:,5));
223 % Yearly average energy [kWh/m^2]
224 yrly_energy=yearavg*hrs/1000;
225 % Monthly flux
226 monDNI=zeros(1,12);
227 CSmonDNI=zeros(1,12);
228 N=1;
229 for i=1:12
230 monDNI(i)=sum(calendar(N:(N+months(i)-1),3))/months(i);
231 CSmonDNI(i)=sum(calendar(N:(N+months(i)-1),4))/months(i);
232 N=N+months(i);
233 end
234
235 monconf=std(calendar(:,3));
236 yavgup=(yearavg+monconf)*ones(12,1);
237 yavglow=(yearavg-monconf)*ones(12,1);
238 yavg=(yearavg)*ones(12,1);
239
240 monnum=1:12;
241 mondiff=monDNI./CSmonDNI;
242
243 %% Daily average
244 function [result]=avg(flux)
245     N=length(flux);
246     result=sum(flux)/N;
247 end
248
249 %% Delta function

```

```
250 function [delta]=declination(n)
251
252 B=(n-1)*360/365;
253 a=0.006918;
254 b=0.399912;
255 c=0.070257;
256 d=0.006758;
257 e=0.000907;
258 f=0.002679;
259 g=0.00148;
260 delta=a - b * cosd(B) + c * sind(B) - d * cosd(2*B) + e * sind(2*B) ...
261      - f * cosd(3*B) + g * sind(3*B);
262 end
```

H.5 Solar Field Simulation

```
1 % Created by Aaron Bame (aaron.bame@gmail.com)
2 % v1 (4/1/20): Create script-simulate solar field design
3
4 %%%%%%%%%%%%%%%%%%%%%%%%%%%%%%%%%%%%%%%%%%%%%%%%%%%%%%%%%%%%%%%%%%%%%%%%%Objective/Algorithm%%%%%%%%%%%%%%%%%%%%%%%%%%%%%%%%%%%%%%%%%%%%%%%%%%%%%%%%%%%%%%%%%%%%%%%%
5 % Simulate a possible solar field configuration given a required thermal%
6 % output and maximum row length. %
7 % 1) Calculate maximum possible solar collection assemblies (SCA) %
8 % per row(Nc) %
9 % 2) Calculate minimum SCA required (SCAmin) %
10 % 3) Find modulus of SCAmin/Nc (SCAmod) %
11 % 4) If SCAmod>(Nc/2) %
12 % 4a) Increase SCAmin (SCAmin=SCAmin+(Nc-SCAmod)) %
13 % 5) If SCAmod<(Nc/2) %
14 % 5a) Decrement maximum SCA per row (Nc=Nc-1) %
15 % 5b) Repeat 3-5 %
16 % 6) Assuming rows are of consistent length for a rectangular field %
17 % (Nr=SCAmin/Nc) %
18 %%%%%%%%%%%%%%%%%%%%%%%%%%%%%%%%%%%%%%%%%%%%%%%%%%%%%%%%%%%%%%%%%%%%%%%%%
19 %%%%%%%%%%%%%%%%%%%%%%%%%%%%%%%%%%%%%%%%%%%%%%%%%%%%%%%%%%%%%%%%%%%%%%%%%Inputs%%%%%%%%%%%%%%%%%%%%%%%%%%%%%%%%%%%%%%%%%%%%%%%%%%%%%%%%%%%%%%%%%%%%%%%%
20 % tech: Integer denoting which technology will be used %
21 % 1-PTC %
22 % 2-LFR %
23 % qsol: Solar thermal load passed into power plant [kW] %
24 %%%%%%%%%%%%%%%%%%%%%%%%%%%%%%%%%%%%%%%%%%%%%%%%%%%%%%%%%%%%%%%%%%%%%%%%%
25
26 %%%%%%%%%%%%%%%%%%%%%%%%%%%%%%%%%%%%%%%%%%%%%%%%%%%%%%%%%%%%%%%%%%%%%%%%%Outputs%%%%%%%%%%%%%%%%%%%%%%%%%%%%%%%%%%%%%%%%%%%%%%%%%%%%%%%%%%%%%%%%%%%%%%%%
27 % Nr: Number of rows (integer) %
28 % Nc: Number of assemblies per row (integer) %
29 % PTC-Assume 3 collectors per assembly %
30 % LFR-Assume 1 collector per assembly %
31 % Ar: Final receiver area resulting from plant%
32 % layout simulation [m2] %
33 % A: Total land used for solar field [m2] %
```

```

34 %%%%%%%%%%%%%%%%%%%%%%%%%%%%%%%%%%%%%%%%%%%%%%%%%%%%%%%%%%%%%%%%%%%%%%%%%
35
36 function [Nr,Na,Ar,A]=solfield(tech,qsol)
37
38 Lrec=10;           % m           Receiver tube length
39 d=0.08;           % m           Receiver tube diameter
40 Lmax=1000;        % m           Maximum field size
41 epsilon=0.9;     % -           Solar exchange efficiency
42 DNI=correlations.DNI(); % W m^-2 Direct Normal Insolation
43
44 if tech==1        % PTC
45     Nmodule=3;    %           Modules per assembly
46     Lsca=Nmodule*Lrec; % m       Length of 1 SCA
47     W=5.6;        % m           Aperture width
48     Ls=15;        % m           Row pitch
49     eta=0.63;     % -           Collection efficiency
50     rc=20;        % -           Concentration ratio
51
52 elseif tech==2    % LFR
53     Nmodule=1;
54     Lsca=Nmodule*Lrec;
55     W=15;
56     Ls=20;
57     eta=0.405;
58     rc=60;
59
60 end
61
62 % Detailed simulation methods are provided in the final report
63 Areq=qsol*1000/(epsilon*rc*DNI*eta);
64
65 SCAMin=ceil((Areq/(pi*d))/Lsca);
66 Na=ceil(Lmax/Lsca);
67 FLAG=1;
68
69 while(FLAG)

```

```

70     extra=mod(SCAmin,Na);
71     if extra==0
72         FLAG=0;
73         Nr=SCAmin/Na;
74     elseif extra>(Na/2)
75         FLAG=1;
76         SCAmin=SCAmin+(Na-extra);
77     else
78         FLAG=1;
79         Na=Na-1;
80     end
81 end
82
83 A=(Na*Nmodule*Lrec)*(W*Nr+(Ls-W)*(Nr-1));
84 Ar=pi*d*Lsca*Nr*Na;
85
86 end

```

H.6 Financial Model

```
1 % FILE:      LCOE_Calc.m
2 % AUTHOR:    Joseph Furner
3 %
4 % PURPOSE:   Calculate the LCOE of a hybrid CSP and coal plant.
5 %
6 %
7 % INPUTS:
8 % Ar        -type:      double
9 %           meaning:    Total heat absorbtion area of the reciever tubes [m2]
10 %
11 % tech      -type:      index
12 %           meaning:    Indicates the technology type
13 %                               1 = parabolic trough
14 %                               2 = linear fresnel
15 %
16 % Wsol      -type:      double
17 %           meaning:    Solar contribution [MW]
18 %
19 % Esav      -type:      double
20 %           meaning:    Boiler load reduction [MW]
21 %
22 % rpr       -type:      double
23 %           meaning:    Increase to electricity customer rate [USD/kWh]
24 %
25 % OUTPUT:
26 % LCOE      -type:      double
27 %           meaning:    Real Levelized Cost of Electricity [USD/kWh]
28 %
29 % CC        -type:      double
30 %           meaning:    Total capital cost for solar portion of project [USD]
31 %
32 % PBT1      -type:      double
33 %           meaning:    Time required for cumulative cash flow = 0 [yrs].
```

```

34 %           If PBT1 > 200 years, the function returns 200.
35 %
36 % PBT2      -type:      double
37 %           meaning:    Time required for cumulative fuel savings to equal
38 %                       investment cost [yrs]
39 %
40 % FE        -type:      double
41 %           meaning:    Total amount saved from fuel savings at the end of
42 %                       the project life [USD]
43
44 function [LCOE,CC,PBT1,PBT2,FE]= LCOE_Calc(Ar,tech,Wsol,Esav,rpr)
45
46
47
48
49 % Default values for project parameters
50 N = correlations.N;           % Analysis period [years]
51 Wnetp = 515000;              % Nominal plant capacity [kW]
52 Wsol = Wsol*1000;
53 %
54
55 % Default values for system costs autamtically defaults to parabolic
56 % trough, if tech = 2, the cost values will be changed to be consistent
57 % with linear fresnel.
58 FSI=correlations.FSI;       % Site improvements [USD/m2]
59 FSF=correlations.FSF;       % Solar field [USD/m2]
60 FHTF=correlations.FHTF;     % HTF system [USD/m2]
61 FFOM=correlations.FFOM;     % Fixed O&M Costs [USD/kW-yr]
62 FVOM=correlations.FVOM;     % Variable O&M costs [USD/MW]
63 rc=correlations.rc;         % Concentration ratio
64
65
66 CHX = correlations.CHX;     % Capital and installation cost of
67                               % heat exchanger [USD]
68 rcont = correlations.rcont; % Contingency [% of direct cost]
69 rEPC = correlations.rEPC;   % Engineer-procure-construct and

```

```

70             % owner costs [% of direct cost]
71 Ftsal = correlations.FTsal;           % Sales tax basis [% of Capital Cost]
72 rtsal = correlations.rtsal;           % Sales tax rate [%]
73
74
75 rITC = correlations.rITC;             % US Investment Tax Credit [% of CC]
76 rins = correlations.rins;             % Insurance rate [% of CC]
77 rtprp = correlations.rtprp;           % Property tax rate [% of basis]
78 Ftprp = correlations.Ftprp;           % Property tax basis [% of CC]
79 rSALV = correlations.rSALV;           % Salvage Percentage [% of CC]
80 %
81
82
83 % Default Values for LCOE calculator
84 ri = correlations.ri;                  % Inflation rate [%/year]
85 rtst = correlations.rtst;              % State tax rate [%/year]
86 rtFed = correlations.rtFed;            % Federal tax rate [%/year]
87 SCdep = correlations.SCdep;            % Depreciation schedule 5-yr MACRS
88             % [% of capital cost]
89 FL = correlations.FL;                  % Project term debt fraction
90             % [% of capital cost]
91 rint = correlations.rint;              % Nominal debt interest rate [%/year]
92 P = correlations.P;                    % Loan term [years]
93 rrd = correlations.rrd;                % discount rate (real) [%/year]
94 %
95
96
97 % Default Values for fuel savings used in payback time calculation
98 FF = correlations.FF;                  % Cost of coal [USD/sh.tn.]
99 HVF = correlations.HVF;                % Hard coal heating value [MJ/kg]
100 rtCO2 = correlations.rtCO2;            % Carbon tax [USD/sh.tn.of CO2]
101 Fcc = correlations.Fcc;                % CO2 emitted to coal burned ratio
102 Suse = correlations.hsun;              % Time solar field is in use [h]
103 etaE = 1;                              % Ratio of consumer power to
104             % generated power
105 %

```

```

106
107
108 % Conversion of Percentages into decimals
109 rcont = rcont/100;
110 rEPC = rEPC/100;
111 Ftsal = Ftsal/100;
112 rtsal = rtsal/100;
113 rITC = rITC/100;
114 ri = ri/100;
115 rtst = rtst/100;
116 rtFed = rtFed/100;
117 SCdep = SCdep./100;
118 FL = FL/100;
119 rint = rint/100;
120 rins = rins/100;
121 rtprp = rtprp/100;
122 Ftprp = Ftprp/100;
123 rSALV = rSALV/100;
124 rrd = rrd/100;
125 %
126
127 % Calculation of nominal discount rate
128 rnomd = ((ri + 1)*(rrd + 1) - 1);
129 %
130
131 % Calculation of Aperture Area
132 Ap = Ar*rc(tech);
133 %
134
135 % Capital cost calculation
136 % Calculate Direct Capital Cost
137 Subtotal = (FSI(tech)*Ap) + (FSF(tech)*Ap) + (FHTF(tech)*Ap) + CHX;
138 CDC = Subtotal*(1 + rcont);
139 %
140
141 % Calculate Indirect Capital Cost

```

```

142 CIC = (rEPC*CDC) + (Ftsal*rtsal*CDC);
143 %
144
145 % Calculate Total Capital Cost
146 CC = CDC + CIC;
147 %
148
149 % Year by year cost analysis
150 Project_life = 1:N;
151 E = Wnetp*8760;
152 E = zeros(1,N) + E;
153 %
154
155 % Annual Expenses calculation
156 CFOM = zeros(1,N) + FFOM(tech)*(1+ri).^(Project_life-1)*Wsol;
157 CVOM = zeros(1,N) + FVOM(tech)/1000.*(Wsol*Suse*365).*(1+ri).^(Project_life-1);
158 Cins = zeros(1,N) + CC*rins.*(1+ri).^(Project_life-1);
159 Property_value = zeros(1,N) + CC*Ftprp;
160 Ctprp = zeros(1,N) + rtprp.*Property_value;
161 CSALV = zeros(1,N);
162 CSALV(N) = CC*rSALV;
163 EXP = CFOM + CVOM + Cins + Ctprp - CSALV;
164 %
165
166
167 % Loan Payments
168 DEBTamt = CC*FL;
169 Equity = CC - DEBTamt;
170 CPI = zeros(1,N) + ((DEBTamt*(rint*(1+rint)^P))/((1+rint)^P-1));
171 CPI(P+1:N) = 0;
172 DEBT = zeros(1,P+1);
173 INT = zeros(1,N);
174 PRN = zeros(1,N);
175 DEBT(1) = DEBTamt;
176 for i = 1:P
177

```

```

178     INT(i) = rint*DEBT(i);
179     PRN(i) = CPI(1) - INT(i);
180     DEBT(i+1) = DEBT(i) - PRN(i);
181 end
182 Pretax_cashflow = -(CPI + EXP);
183 %
184
185
186 % State income tax
187 taxable_income = zeros(1,N);
188 ITCbas = CC;
189 DEPbas = ITCbas - 0.5*(rITC*CC);
190 STATE_DEP = zeros(1,N);
191 STATE_DEP(1:length(SCdep)) = (SCdep*DEPbas);
192 STATE_totalDeductions = EXP + INT + STATE_DEP;
193 STATE_without_deductions = taxable_income-STATE_totalDeductions;
194 STATE = rtst*STATE_without_deductions;
195 STATESav = 0 - STATE;
196 %
197
198
199 % Fedreral income tax
200 DEPbas = ITCbas - 0.5*(rITC*CC);
201 FED_DEP = zeros(1,N);
202 FED_DEP(1:length(SCdep)) = (SCdep*DEPbas);
203 FED_totalDeductions = EXP + INT + FED_DEP + STATE;
204 FED_without_deductions = taxable_income-FED_totalDeductions;
205 FED = rtFed*FED_without_deductions;
206 FED_ITC = rITC*ITCbas;
207 FEDsav = 0 - FED;
208 FEDsav(1) = 0 + (FED_ITC) - FED(1);
209 %
210
211 % First year benefits including: Fuel savings,additional profits, CO2 tax
212 FF = FF/977.4216; % USD/sh.tn. - USD/kg
213 HVF = HVF/3.6; % MJ/kg - kWh/kg

```

```

214 Esav = Esav*1000*Suse*365; % MW - kWh. 365 days/yr
215 rtCO2 = rtCO2*Fcc; % USD/sh.tn.CO2 - USD/sh.tn coal
216 rtCO2 = rtCO2/977.4216; % USD/sh.tn - USD/kg
217 FS = FF*Esav/HVF; % Calculates fuel savings [USD]
218 TAX = rtst+rtFed*(1-rtst); % Calculates effective tax rate
219 CO2TAXsav = (rtCO2*Esav/HVF)*(1-TAX); % Carbon tax for the first year
220 Prof = rpr*Wnetp*etaE*Suse*365; % Additional profits using the
221 % green energy premium
222 %
223
224 % Calculation of after tax costs
225 Ctot = FEDsav + STATEsav + CO2TAXsav + Pretax_cashflow;
226 %
227
228
229 % Calculation of LCOE
230 Discounted_E = E./(1+rrd).^Project_life;
231 Discounted_C = Ctot./(1+rnomd).^Project_life;
232 LCOE = (Equity - sum(Discounted_C))/sum(Discounted_E);
233 %
234
235
236 % Calculation of payback time
237
238
239
240 % Cash flow analysis for 200 years
241 N_PBT1 = 1:200;
242 CFOM_PBT1 = zeros(1,200) + CFOM(1)*(1+ri).^ (N_PBT1-1);
243 CVOM_PBT1 = zeros(1,200) + CVOM(1).*(1+ri).^ (N_PBT1-1);
244 Cins_PBT1 = zeros(1,200) + CC*rins.*(1+ri).^ (N_PBT1-1);
245 Property_value_PBT1 = zeros(1,200) + CC*Ftprp;
246 Ctprp_PBT1 = zeros(1,200) + rtprp.*Property_value_PBT1;
247 CSALV_PBT1 = zeros(1,200);
248 CSALV_PBT1(N) = CC*rSALV;
249 EXP_PBT1 = CFOM_PBT1 + CVOM_PBT1 + Cins_PBT1 + Ctprp_PBT1 - CSALV_PBT1;

```

```

250 CPI_PBT1 = zeros(1,200) + ((DEBTamt*(rint*(1+rint)^P))/((1+rint)^P-1));
251 CPI_PBT1(P+1:200) = 0;
252 INT_PBT1(1:N) = INT;
253 INT_PBT1(N+1:200) = 0;
254 PRN_PBT1(1:N) = PRN;
255 PRN_PBT1(N+1:200) = 0;
256 Pretax_cashflow_PBT1 = -(CPI_PBT1 + EXP_PBT1);
257 taxable_income_PBT1 = zeros(1,200);
258 STATE_DEP_PBT1 = zeros(1,200);
259 STATE_DEP_PBT1(1:length(SCdep)) = (SCdep*DEPbas);
260 STATE_total_Ded_PBT1 = EXP_PBT1 + INT_PBT1 + STATE_DEP_PBT1;
261 STATE_without_deductions_PBT1 = taxable_income_PBT1-STATE_total_Ded_PBT1;
262 STATE_PBT1 = rtst*STATE_without_deductions_PBT1;
263 STATESav_PBT1 = 0 - STATE_PBT1;
264 FED_DEP_PBT1 = zeros(1,200);
265 FED_DEP_PBT1(1:length(SCdep)) = (SCdep*DEPbas);
266 FED_total_Ded_PBT1 = EXP_PBT1 + INT_PBT1 + FED_DEP_PBT1 + STATE_PBT1;
267 FED_without_deductions_PBT1 = taxable_income_PBT1-FED_total_Ded_PBT1;
268 FED_PBT1 = rtFed*FED_without_deductions_PBT1;
269 FEDsav_PBT1 = 0 - FED_PBT1;
270 FEDsav_PBT1(1) = 0 + (FED_ITC) - FED(1);
271 Ctot_PBT1 = FEDsav_PBT1 + STATESav_PBT1 + CO2TAXsav + Pretax_cashflow_PBT1;
272 %
273
274
275 % Calculation of PBT1
276 ProfV = zeros(1,200) + Prof.*(1+ri).^ (N_PBT1-1);
277 FSV = zeros(1,200) + FS.*(1+ri).^ (N_PBT1-1);
278 After_tax_benefit = (FSV+ProfV)*(1-TAX);
279 After_tax_cashflow = Ctot_PBT1 + After_tax_benefit;
280 PBT1cost = After_tax_cashflow + PRN_PBT1 + INT_PBT1.*(1-TAX);
281 CUMcash = -CC;
282 PBT = 1;
283 PBT1 = 1;
284 j = 0;
285 FE = 0;

```

```

286 for i = 1:200
287     Extra = -CUMcash/PBT1cost(i);
288     CUMcash = CUMcash + PBT1cost(i);
289     PBT = PBT + 1;
290     if i == N
291         FE = FE + CUMcash;
292     end
293     if CUMcash > 0 && j == 0
294         PBT1 = PBT + Extra;
295         j = i;
296     end
297     if PBT1 > 1 && FE > 0
298         break;
299     end
300 end
301 PBT1 = PBT1-1;
302 % Returns NaN when PBT1 exceeds 200 years
303 if PBT1 <= 200 && CUMcash < 0
304     PBT1 = 200;
305 end
306 %
307
308
309 % Calculation of PBT2
310 PBT2 = log(((CC*ri)/(FS + CO2TAXsav +Prof))+1)/log(1+ri);
311 %
312
313 end

```